## ABSTRACT

**Title of Dissertation:** THE GENESIS OF TYPHOON CHANCHU (2006)

Wallace A. Hogsett, Ph.D., 2010

**Directed By:** Professor Da-Lin Zhang
Department of Atmospheric and Oceanic Science

The phenomenon of tropical cyclogenesis (TCG), defined as the processes by which common tropical convection organizes into a coherent, self-sustaining, rapidly-rotating, and potentially destructive tropical cyclone (TC), consistently headlines research efforts but still remains largely mysterious. TCG has been described by a leading TC scientist as "one of the great remaining mysteries of the tropical atmosphere." This dissertation was motivated by a specific case of TCG: the near-equatorial formation of a well-organized synoptic cyclonic disturbance during the active West Pacific Madden-Julian Oscillation (MJO). At very high resolution, the Weather Research and Forecasting (WRF) mesoscale atmospheric model proves capable of reproducing the multiscale interactions that comprise the TCG of Typhoon Chanchu.

In the first part of the dissertation, the synoptic observations of the incipient disturbance (i.e., weak cyclonic vortex) are compared with the results from the WRF simulation. It is found that the disturbance tilts westward with height, and as a consequence of the vertical tilt, large-scale ascent (and thus precipitation) is favored on the downtilt-right side of the vortex. A major result is that the precipitation to the north of the tilted vortex serves as an attractor to the vortex through its generation of

vorticity, thereby serving to dually diminish the vertical tilt of the vortex and deflect the incipient storm northward. Observations and the model simulation both indicate that TCG commences when the storm becomes vertically upright.

In the second part of the dissertation, it is shown that the simulated downtilt-right precipitation takes the form of several mesoscale convective systems (MCSs), which spawn midlevel vortices that merge with and intensify the midlevel vortex. The precipitation during the several days prior to TCG generally serves to precondition the near-vortex environment by raising the low- and midlevel humidity. Apparently, the onset of TCG can be characterized as the transition of a tilted cold-core vortex into a vertically-erect warm-core vortex.

The final part of the dissertation addresses the storm-scale processes during the day of TCG. The primary point of emphasis is the vertical wind shear, which is often dismissed as detrimental to the prospect of TCG. On the contrary, it is found that the inherent vertical shear of the tilted vortex is actually the critical variable in understanding the TCG of Chanchu through its role in the vorticity tilting term. More specifically, the clockwise turning (i.e., veering) of the shear vector with height suggests a new mechanism for the rapid generation of system-scale vorticity, which current hypotheses posit as simply a stochastic amalgamation of vorticity sufficient to trigger self-intensification. The near-surface spin-up mechanism is analogous to that which occurs in supercell thunderstorms. The missing link in TCG understanding may be the dynamic implications of the veering wind profile in which the convection develops.

# THE GENESIS OF TYPHOON CHANCHU (2006)

By

Wallace A. Hogsett

Dissertation submitted to the Faculty of the Graduate School of the
University of Maryland, College Park, in partial fulfillment
of the requirements for the degree of
Doctor of Philosophy
2010

Advisory Committee:
Prof. Da-Lin Zhang, Chair
Prof. James Carton
Prof. Daniel Kirk-Davidoff
Prof. Hugo Berbery
Prof. Karen Prestegaard (Dean's Representative)

# Preface

This dissertation is presented in a simple five-chapter format, in which the first chapter provides a basic, broad, and bullish perspective of the present understanding, the outstanding issues of interest, and the need for continued tropical cyclogenesis (TCG) research. Each of Chapters 2 – 4 represents a self-contained study of the genesis of Typhoon Chanchu. The chapters build on one another and logically progress from synoptic scales and weekly timescales (Chapter 2), to mesoscale and daily timescales (Chapter 3), and finally to the storm scale and hourly timescales (Chapter 4). The final chapter summarizes the major findings and sketches the research path forward.

The three middle chapters are organized as three dependent submissions to the literature. Chapter 2 has been accepted as an article to the *Journal of the Atmospheric Sciences* (January 2010), Chapters 3 has been submitted to the same journal as Part II, and Chapter 4 will similarly be submitted in the coming months as Part III of this ongoing study. The final Chapter 5 contains the plan for continued study of what appears to be a rich dataset, as well as future theoretical and practical extensions of the scientific findings presented herein.

# Dedication

To the late Jean Grace.

# Acknowledgements

Thanks to: Dad for encouraging me to spend time enjoying the outdoors; Mom for encouraging me to do anything I wanted to do; Will and Hal for camaraderie throughout the years; Prof. Zhang for providing the requisite tools and unfettered freedom to innovate while wielding ruthless constructive criticism; Alex and Charcoal; John for encouraging occasional irresponsibility; Joel for endless encouragement; Ashley for pretending to listen to my half-constructed theories on tropical cyclogenesis; the U.S. State Department for auxiliary education; Chanh for confidence; Rich for encouraging me to come to graduate school in DC; and of course the weather, for giving me something to do with my life.

# Table of Contents

# Chapter 1: Introduction

## *1.1. Statement of the problem*

The formation of tropical cyclones (TCs) is poorly understood. Consistent observations are sparse in the vast tropical oceans, and field projects require extraordinary funding to adequately sample nascent storms. Thus the acquisition of a dataset that is capable of resolving the multiscale interactions that comprise TCG is one of the greatest challenges to TCG investigators. In fact, data scarcity is probably *the* limiting factor preventing a more complete understanding of TCG, since the densely-sampled land-based vortical storms are significantly better understood.

Each year many tropical waves and convective clusters develop in the tropics, but only a select few undergo TCG. Of course, the limited observational resources (e.g. aircraft hours, dropsondes, etc.) can spread thin very quickly in the face of innumerable TC "prospects." This is especially true when existing observational resources are directed at mature TCs that threaten coastal wealth rather than those developing in the open ocean. An exception is a handful of targeted observational field campaigns that have contributed significantly to an increasing, albeit slowly, understanding of TCG in the past half-century.

## *1.2. Importance of the problem*

While it could be argued that TCG should be a secondary forecasting concern, with the track and intensity forecasts of mature TCs that do extensive damage as the primary concern, it is concerning how little is understood about the TCG process. Often TCG is only noticed after it has begun. Indeed, most TCG cases do occur far

from land in the open ocean, including the case of Chanchu presented herein, but TCG can occur near shore, quickly, and without forecast skill. Such cases present a great risk to coastal populations. Several cases of poorly-forecast, near-land TCG in the recent past (e.g. Hurricane Humberto, 2007) remain the subject of intense investigation, but until a fundamental understanding of the TCG processes is attained, TCG forecasts of such dangerous cases will fail.

If case studies, such as the present study, can provide any improved understanding of the structure and evolution of pre-TC disturbances and their associated TCG, forecasts could benefit. Given finite observational capabilities, improved understanding could help to more efficiently target observations toward high-value locations that may impact TCG more than others. To the extent that improved understanding is obtained from analyses herein, and subsequently generalized, more precisely targeted observations and unique forecasting techniques will certainly follow.

### *1.3. Scope of the problem*

Stressing depth over breadth, this dissertation is based almost exclusively on a single numerical simulation in which a single episode of TCG is completely captured at cloud-resolving scale. To the extent that the current generation of mesoscale atmospheric models can provide a dynamically consistent perspective of the atmosphere, the point at issue in this dissertation is not one of *forecasting* TCG, but instead one of *understanding* the TCG process through the acquisition and analysis of a high-resolution TCG dataset. Until now, no such dataset has been obtained (or if so, it has not been analyzed in depth). An attempt is made to shed light on processes

that contribute to intensification at various scales and have eluded understanding until now.

# Chapter 2: Formation of Chanchu during the MJO

*2.1. Introduction*

In the Western North Pacific (WNP) basin, the frequency of tropical cyclogenesis (TCG) peaks in the late northern summer, when the monsoon trough extends eastward from Asia into the Pacific Ocean. It is in this region that easterly trade winds meet westerly monsoon winds and sustain an environment that is favorable for enhanced convergence and rotation of the low-level winds. Previous studies have identified this low-latitude confluence zone at the easternmost extent of the monsoon trough as a focus for TCG (see Holland 1995).

However, few tropical cyclones (TCs) develop prior to June in the WNP, even though the necessary conditions for TCG persist year round (Gray 1998). This is because this region lacks climatological foci for TCG prior to the onset of the Asian monsoon. Instead, trade easterlies dominate the WNP during the spring months, and the rare TCs that do develop during this pre-monsoon environment are often associated with anomalous westerly equatorial winds that modulate the formation of TC precursor disturbances (Ritchie and Holland 1999). This is the case for the present study of Typhoon Chanchu, which developed in early May 2006. In fact, Mao and Wu (2008) found that Chanchu served as the trigger for the onset of the 2006 Asian monsoon through its modulation of the meridional temperature gradient.

The Madden-Julian Oscillation (MJO; Madden and Julian 1994) is the dominant mode of intraseasonal variability globally, and it was first discussed by Liebmann et al. (1994) as a favorable environment for TCG. Barrett and Leslie (2009) showed that the MJO significantly modulates TC activity in all ocean basins worldwide

through its enhancement of low-level vorticity and deep convection. In general, the MJO can be characterized as a wavelike disturbance that propagates eastward from the equatorial Indian Ocean into the WNP; its active phase is associated with active deep convection and westerly winds in the lower troposphere, the so-called westerly wind bursts (WWBs). Near-equatorial WWBs converge with easterly trades during the active phase of the MJO, not only enhancing deep convection, but also facilitating the growth of cyclonic disturbances through wave accumulation - a process by which cyclonic vorticity associated with traveling disturbances is gathered in a region of converging zonal wind (Chang and Webster 1990). When WWBs impinge on the easterly trades, the cyclonic vorticity associated with the zonal wind shear allows northwestward-moving cyclonic eddies to develop via barotropic energy conversions, as found by Maloney and Hartmann (2001). These sub-synoptic eddies can serve as precursors to TCG (Aiyyer and Molinari 2003), and if the eddies are continuously produced they can repeatedly spawn TCs (Molinari et al. 2007). In some situations, WWBs can modulate the development of twin TCs that are roughly symmetric about the equator (Lander 1990; Zhu et al. 2003).

Dickinson and Molinari (2002) showed that within the area of active convection associated with the MJO, mixed Rossby-gravity (MRG) waves can develop and serve as precursors to TCG. The MRG waves exhibit a westward vertical tilt because of the easterly vertical shear during the MJO (Frank and Roundy 2006). Dickinson and Molinari (2002) further found that deep convection prior to TCG develops not near the circulation center, but to its north. As the westward-tilted MRG waves "transition" to tropical depression (TD) type waves, deep convection develops closer

to their centers and they move northwestward away from the equator. The northward translation and "transition" of the incipient equatorial disturbances to off-equatorial TCs still remain mysteries central to the issue of TCG during the active MJO.

While the previous studies have established the relationship between the MJO, WWBs, and TCG, little is certain about the mechanisms by which they interact. Specifically, what is the importance of the associated WWB vortex, occurring at the synoptic scale, in initiating TCG? How is the low-level cyclonic circulation, which is necessary for triggering the wind-induced surface heat exchange (WISHE) processes (Emanuel 1986), initially generated from the large-scale flows? In this dissertation, we attempt to address these issues by examining the multi-scale processes involving the MJO, WWBs, mesoscale convective systems (MCSs), mesoscale convective vortices (MCVs), and convective scale processes during the genesis of Typhoon Chanchu (2006).

The purposes of Chapter 2 of this dissertation are to (i) document the evolution of large-scale conditions associated with Typhoon Chanchu, from its incipient to typhoon stage, using the National Centers for Environmental Prediction (NCEP) final analysis (FNL) at $1.0^{o}$ resolution and satellite observations; (ii) demonstrate that the general flow structures and organization of precipitation that comprise the genesis of Chanchu could be reasonably duplicated by an 11-day cloud-resolving simulation using the Weather Research and Forecast (WRF) model at the finest resolution of 2 km; and (iii) examine the evolution of the simulated westward-tilted vortex associated with a WWB, hereafter the tilted WWB-vortex, that occurs prior to the genesis of Chanchu.

The next section provides an overview of the evolution of Chanchu in relation to the large-scale environment as well as the 2006 typhoon season and intraseasonal variability. Section 2.3 describes the configuration of the WRF model used for the present study. Section 2.4 compares the simulation results to available observations prior to the genesis of Chanchu. Section 2.5 shows the mechanisms by which the pre-Chanchu disturbance develops and evolves during the pre-genesis stage. A summary and concluding remarks are given in the final section.

## *2.2. Synoptic overview of Chanchu*

### *2.2.1. TC activity in the Indian and West Pacific basins: Spring 2006*

Chanchu was the second named TC of the 2006 Northern Hemisphere tropical season and the second to make landfall in Southeast Asia. The first TC, Cyclone Mala, developed in the Indian Ocean basin on 20 April and became what would retrospectively be the strongest TC of the 2006 TC season and the first category-4 cyclone of the 21$^{st}$ century in the Indian Ocean basin. The pre-Mala disturbance developed slowly as it tracked northwestward from near the northern tip of Sumatra into the open Bay of Bengal during 20 – 24 April (Fig. 2.1). Mala subsequently intensified in warm water (> 30ºC), reached peak intensity on 28 April, weakened slightly prior to landfall in Burma on 29 April, and accelerated northeastward over mainland China and into the open Pacific along the northern periphery of a subtropical ridge.

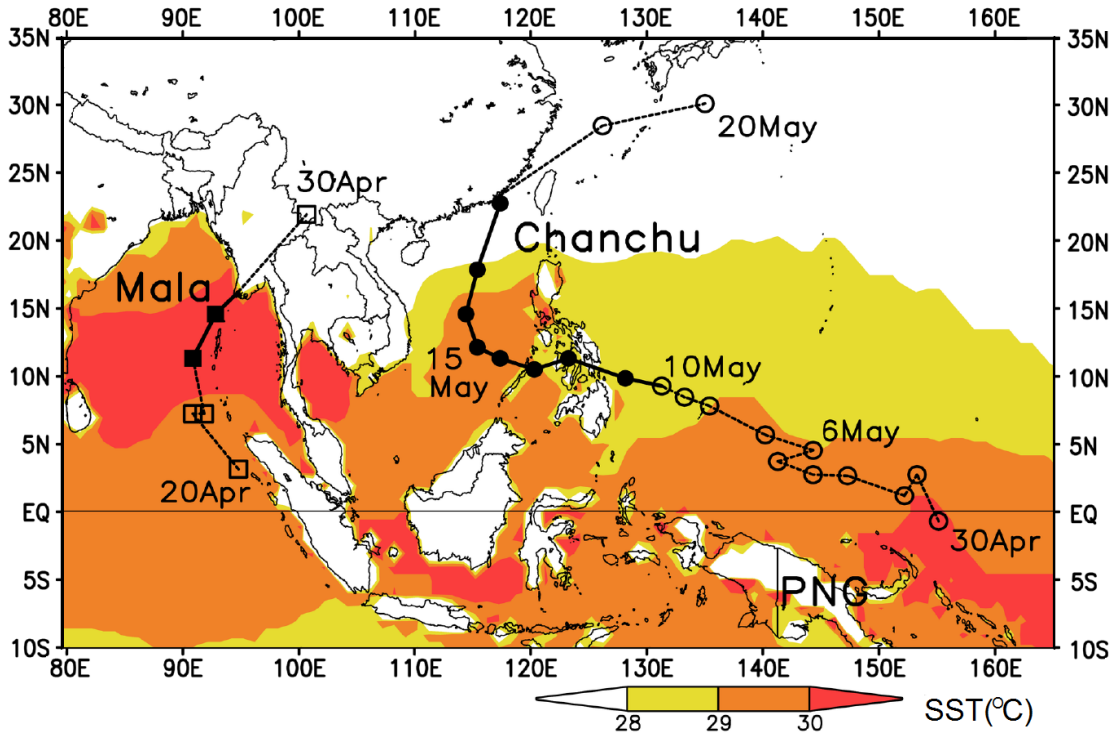


Figure 2.1. Observed track of Typhoon Chanchu (Cyclone Mala), marked at daily (two-day) intervals and based on the 900-hPa circulation center from NCEP's FNL during the period of 0000 UTC 30 April – 20 May (20 – 30 April) 2006. Filled symbols and heavy track lines represent the periods when the intensity exceeded category one hurricane equivalent. NCEP SSTs at the model initial time are shaded according to the gray scale. Symbol "PNG" denotes the location of Papua New Guinea.

As Mala completed its extratropical transition, an area of active equatorial deep convection northeast of Papua New Guinea, denoted by "PNG" in Fig. 2.1, spawned the pre-requisite disturbance on 30 April that led to the second named storm of the 2006 season, Typhoon Chanchu. The pre-Chanchu disturbance appears to have originated in the Southern Hemisphere and crossed the equator as it moved erratically northwestward (Fig. 2.1). After an 8-day incubation period, the pre-Chanchu disturbance began to organize on 7 May, received the designation of tropical depression on 8 May, and by 10 May it became a typhoon. Chanchu deepened slowly as it moved across the Philippine archipelago, and after entering the South China Sea

on 13 May it deepened rapidly and became a super-typhoon on 15 May. Subsequently, Chanchu turned sharply northward and accelerated toward mainland China. It weakened over the cooler water (Fig. 2.1) of the northern South China Sea prior to landfall late on 17 May and finally underwent extratropical transition as it merged with a midlatitude frontal system and the associated jet stream aloft. While the current chapter focuses on the formation of Chanchu, the next two subsections indicate that the near-equatorial formation of Mala two weeks prior to Chanchu was not necessarily coincidental. Their associated pre-genesis disturbances were closely associated with the active phase of the MJO.

*2.2.2. Relationship between Chanchu and the MJO*

For the purposes of this study, we use the term *pre-genesis* to refer to the period between the initial identification of a low-level (900-hPa) cyclonic circulation in the NCEP FNL and the official recognition of the system by the Joint Typhoon Warning Center (JTWC). The pre-genesis periods for Mala and Chanchu are shown schematically in Fig. 2.2 against the background of the MJO during April – May 2006. During this period, the MJO exhibited its well-known west to east propagation, from the Indian Ocean into the Pacific Ocean.

Fig. 2.2 shows that Mala and Chanchu, while developing in separate basins, both began pre-genesis during the convectively active phase of apparently the same MJO event. The pre-Mala disturbance developed first as a closed low-level circulation on 20 April near 100°E, at the peak of the active phase of the MJO in the Indian Ocean, and reached its depression stage as the equatorial Indian Ocean transitioned to the inactive phase of the MJO. During its pre-genesis stage, the pre-

Mala disturbance translated west-northwestward under the influence of the easterly trades. By 30 April, Mala intensified into a destructive cyclone in the Bay of Bengal, as the MJO propagated eastward into the West Pacific along with its enhanced equatorial deep convection.

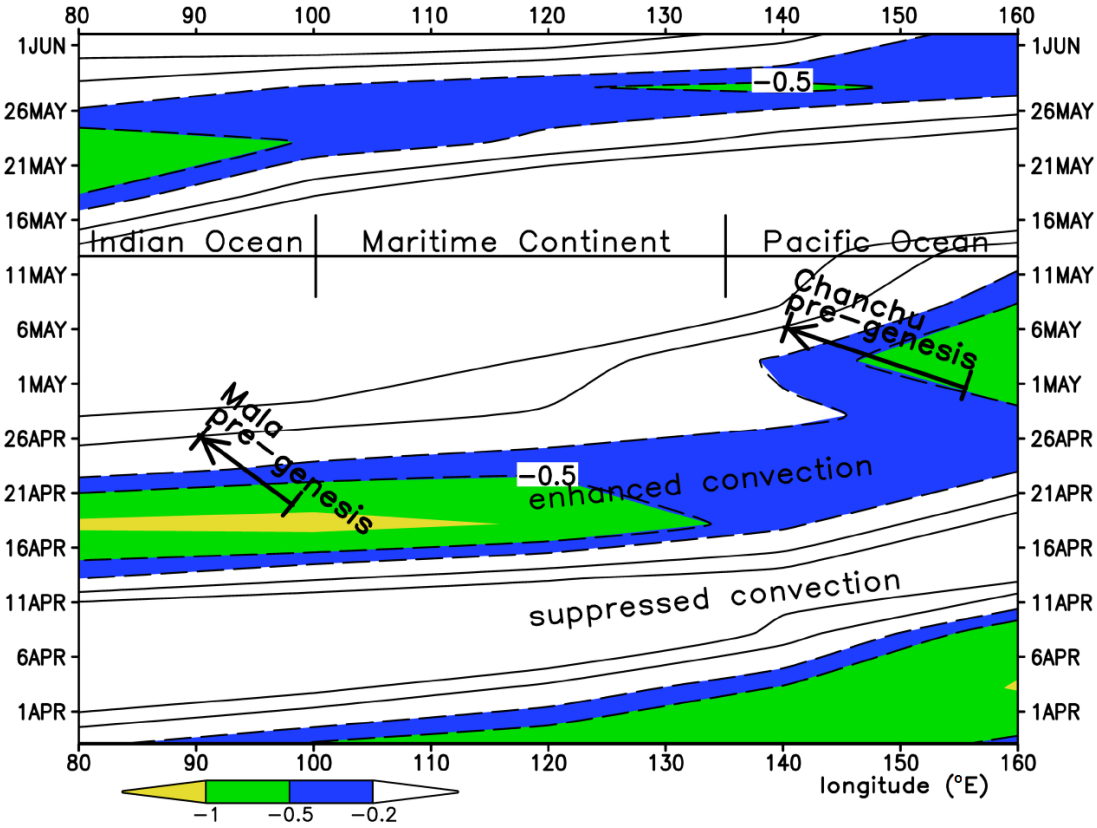


Figure 2.2. Hovmöller diagram of the observed (5-day) mean MJO index from 27 March to 2 June 2006 for the equatorial region spanning from 80°E to 160°E. Positive (negative) magnitudes are plotted using solid (dashed) contours at intervals of ±0.2 and 0.5 and represent convectively inactive (active) periods. Convectively active periods are shaded according to the gray scale. The pre-genesis periods of Chanchu and Mala are marked by the heavy arrows. Data source: www.cpc.ncep.noaa.gov/products/precip/CWlink/daily_mjo_index/mjo_index.html.

On 30 April, the pre-Chanchu disturbance emerged near 155°E during the MJO's local peak conditions (Fig. 2.2), moved west-northwestward during pre-genesis, and became a depression during the transition period between the active and inactive MJO. The precursors associated with Mala and Chanchu appeared to persist

as weak but coherent low-level disturbances for 5 and 8 days, respectively, prior to being classified as tropical depressions. It is likely that the slowly evolving MJO helped maintain the two weak disturbances (Liebmann et al. 1994). While the pre-Mala and pre-Chanchu disturbances both developed during the active phase of the MJO, their geneses occurred as the MJO weakened (Fig. 2.2). Thus, the active phase of the MJO could not be considered as sufficient for TCG, but only favorable for the development and maintenance of the pre-Mala and pre-Chanchu disturbances.

*2.2.3. Pre-genesis of Chanchu*

Enhanced deep convection and WWBs are well-known accompaniments to the MJO in the near-equatorial region. Fig. 2.3 shows the synoptic setup at the 600- and 900- hPa levels during the pre-genesis and genesis stages of Chanchu, i.e., from 0000 UTC 28 April – 0000 UTC 8 May 2006. A subtropical high-pressure system dominated the WNP, with the easterly winds spanning the basin except in the vicinity of the equator. As early as 28 April, Fig. 2.3g shows a WWB situated on the maritime continent, extending eastward to PNG. Convergence of the WWB and the easterly trades led to enhanced cloud cover along their northwest-southeast oriented interface (see Figs. 2.4a,b) with an inverted trough (see the dashed lines in Fig. 2.3g) just east of PNG in advance of the WWB. The 900-hPa trough amplified as the WWB intensified to exceed 10 m $s^{-1}$ and progressed eastward to nearly 160°E, and by 30 April a closed cyclonic vortex developed to both the north ("C") and south ("L") of the WWB (Fig. 2.3h). By 2 May, two cyclonic vortices ("L") had developed south of the equator (Fig. 2.3i). Note that the two southern vortices resulted from the split of the WWB as it crossed the rugged terrain of PNG. Though the focus of the current

chapter is the development of the northern vortex into Chanchu, it is noteworthy that the PNG landmass sits entirely in the southern hemisphere, and it likely disrupted the formation of a coherent mirror image vortex to that which formed in the northern hemisphere by 2 May.

A northwest-southeast oriented trough also appeared at 600 hPa on 28 April (Fig. 2.3a) in advance of the WWB, but it was located about 1000 km to the west of the 900-hPa trough. By 2 May, two 600-hPa cyclonic circulations also appeared approximately symmetric on the north and south sides of the WWB (Fig. 2.3c). Because the highest mountain on the island (i.e., Puncak Jaya) has an elevation of 4884 m, the WWB at 600 hPa showed little evidence of splitting. Note that the center of the north-hemispheric circulation at 600 hPa appeared as if it were spatially disjointed westward from its 900-hPa counterpart (cf. Figs. 2.3c, i), and that the WWB at 900 hPa extended much farther eastward than that at 600 hPa on 2 May. As will be shown in the next subsection, the two vortices are physically related in the vertical.

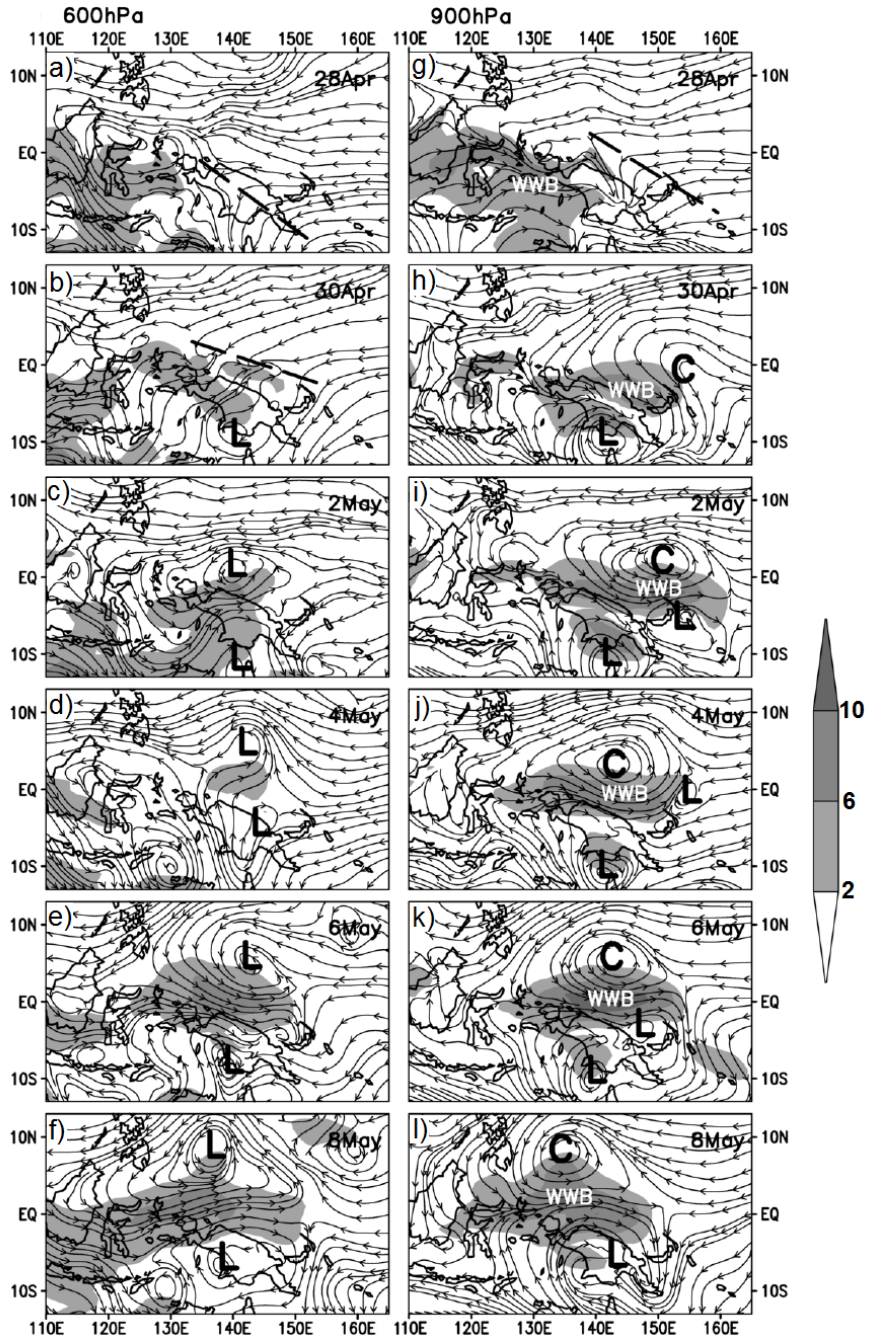


Figure 2.3. Distribution of horizontal streamlines, obtained from NCEP's FNL, with the westerly winds (m $s^{-1}$) shaded in (a) – (f) at 600 hPa (left panel), and in (g) – (l) at 900 hPa (right panel) during the period of 0000 UTC 28 April (top) – 0000 UTC 8 May (bottom) at 2-day intervals. Letter "C" highlights a closed 900-hPa circulation associated with Chanchu, and "L" denotes other closed cyclonic circulations. Symbol "WWB" in the right panel denotes the westerly wind burst, and heavy lines represent trough axes of interest. Fields are averaged within a ± 6-h period and a ± 50-hPa layer.

During the period of May 2 – 6, the 600-hPa circulation moved slowly northeastward (Fig. 2.3c-e), while the 900-hPa vortex moved northwestward (Figs. 2.3i-k). The northwestward movement of such low-level pre-TC disturbances during active MJO periods has been shown by Maloney and Hartmann (2001) and other studies. Because of their differing translations during 2 – 6 May, the horizontal distance between the two vortex centers diminished to nearly zero by 6 May, after which they moved northwestward as a vertically stacked vortex (Figs. 2.3f,l). The subsequent rapid convective organization and TCG after the two vortices were vertically locked in phase is evident on May 10 (see Fig. 2.4g). In fact, Chanchu reached near typhoon strength on this date.

Though the MJO appeared to propagate smoothly eastward (Fig. 2.2), the WWB exhibited a different evolution. That is, the intensifying WWB surged first rapidly eastward during 28 April – 2 May, resulting in the formation of the pre-Chanchu disturbance at 900 hPa, but it retreated northwestward during 2 – 8 May (Figs. 2.3i-l). This behavior is similar to the MJO composites shown by Kim et al. (2008) and other studies. Thus, the evolution of the WWB shown in Fig. 2.3 could be considered typical, although the mechanisms responsible for the northward movement of the MJO are still not well understood. While we do not address this issue herein, it is of interest that because only the northern vortex intensified (and the southern one weakened due likely to the landmass blocking), its subsequent northwestward translation could give the appearance of the northwestward translation of the WWB.

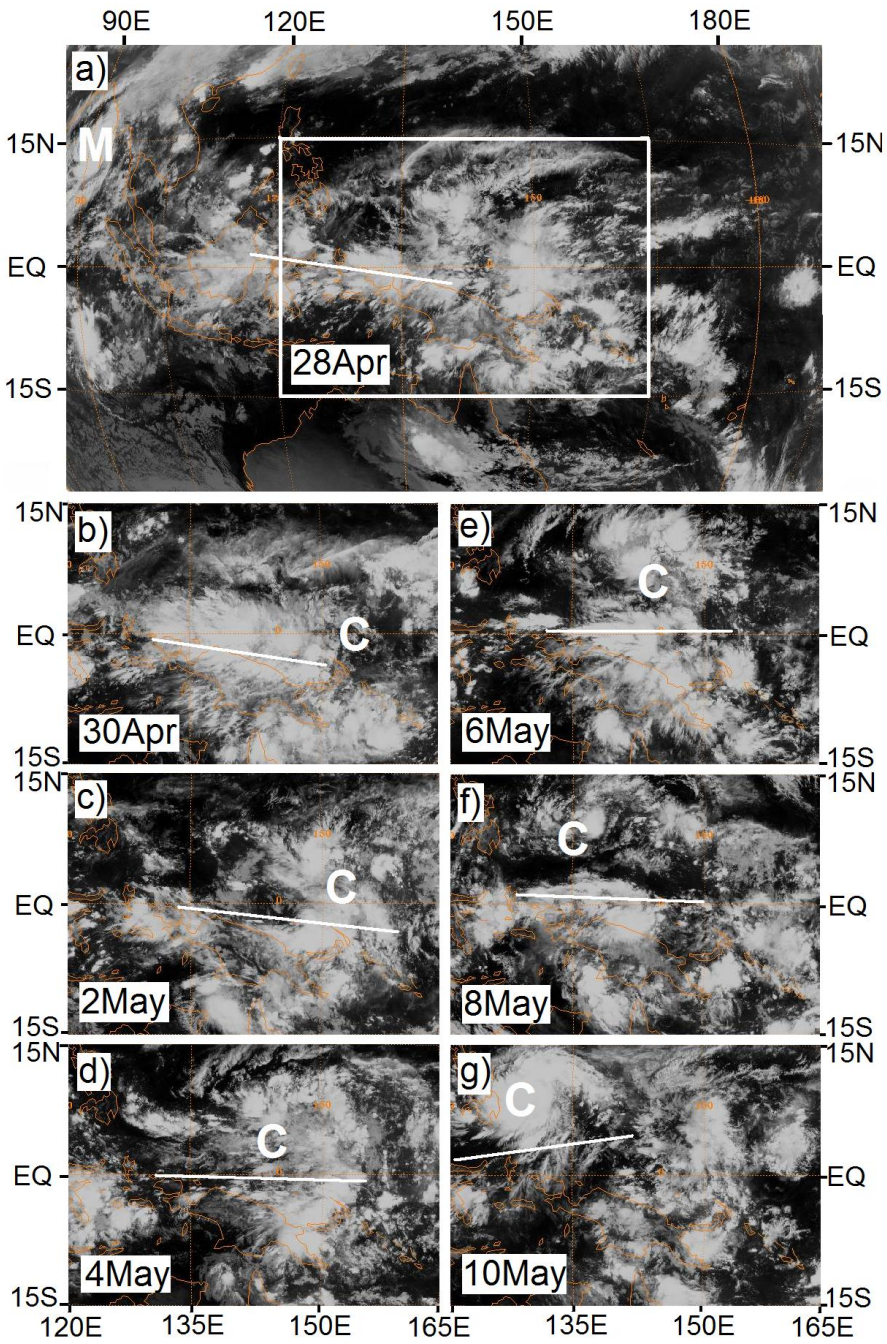


Figure 2.4. Cloud fields as viewed from the MTSAT satellite infrared channel (10.3 – 11.3 μm) at 2-day intervals from 0000 UTC 28 April (a) – 10 May (g) 2006. The box in (a) denotes the region containing the pre-Chanchu disturbance (marked by a "C" during 30 April – 10 May), and the solid line in (a) – (g) denotes the axis of the WWB at 900 hPa. In (a), Cyclone Mala (marked by "M") is shown just prior to its landfall on 28 April. Data source: http://www.ncdc.noaa.gov/gibbs/

As the eastward-moving WWB increased its intensity during 28 April – 2 May, the pre-Chanchu disturbance amplified due likely to the well-known mechanisms of barotropic eddy kinetic energy conversions (Maloney and Hartmann 2001) and wave accumulation (Sobel and Maloney 2000). Once a closed vortex developed (i.e., after April 30), it could persist due to the same mechanisms, plus the continuous deep convection in its vicinity (Fig. 2.4). The pre-Chanchu disturbance did not undergo TCG, however, until it finally ejected poleward of 5°N by 7 May, while the southern disturbance remained in close proximity to PNG and weakened with time (see Figs. 2.3f and 2.3l).

*2.2.4. Mean structure of the MJO*

Fig. 2.5 shows the composite structures of the WWB and its associated dual (actually triple) vortices that occurred during the pre-genesis phase of Chanchu. Note that the peak mean WWB occurred near 2°S. One could expect the development of twin vortices symmetrically located in each hemisphere if the WWB were symmetric about the equator. But with the mean WWB shown in Fig. 2.5, the southern vortex development should be dynamically favored due to the presence of a larger Coriolis force. However, as discussed earlier, the southern vortex developed in the vicinity of a large landmass, which tended to disrupt intensification. Evidence of the second southern vortex can be seen near 10ºS (Fig. 2.5) in association with the southern (and weaker) split of the WWB. Further, the northward movement of the WWB at later stages favored the northern vortex. So in extraordinarily fortuitous situations twin TCs could develop and exhibit a mirror image about the WWB (e.g., see Zhu et al. 2003), but the present case is not such a scenario due to the large landmass and the

northward movement of the WWB that inhibited the southern vortices. Clearly, the MJO, through enhanced low-level confluence (see "X" symbols marked in Fig. 2.5) associated with the WWB, barotropic eddy growth, and northward movement into the open ocean, created an environment that was favorable for TCG in the northern hemisphere.

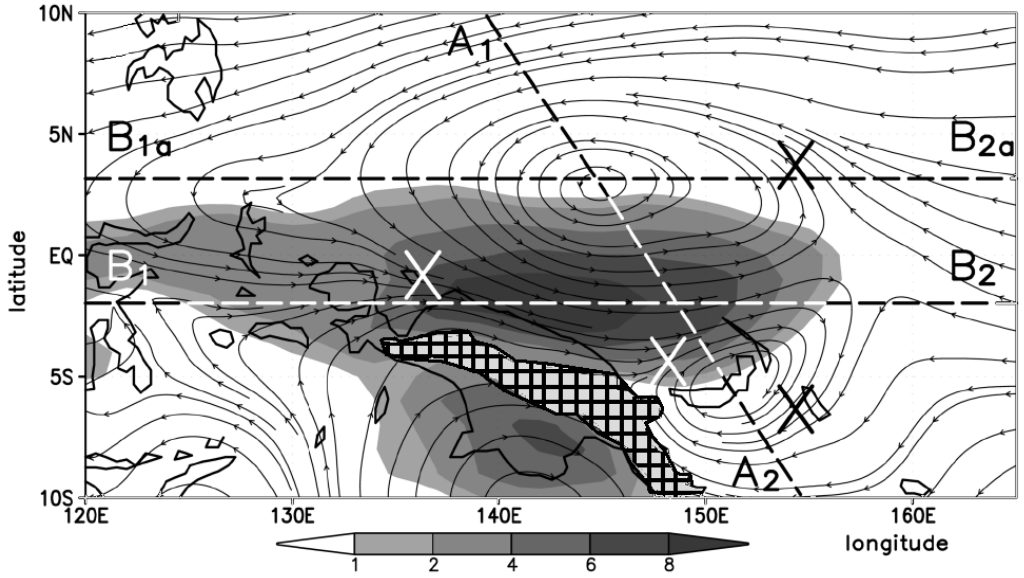


Figure 2.5. The 900 – 800 hPa layer-mean horizontal streamlines, with the westerly flows shaded (m $s^{-1}$), that are averaged during the period of 30 April – 5 May 2006 from NCEP's FNL. Lines $A_1 - A_2$, $B_1 - B_2$, and $B_{1a} - B_{2b}$ represent the paths of the vertical cross sections, shown in Fig. 2.6, through the centers of the quasi-symmetric cyclonic vortices, along the axis of the WWB, and through the pre-Chanchu vortex, respectively. Symbol "X" marks the areas of obvious low-level confluence, and areas of underneath terrain are hatched.

Fig. 2.6 shows the across- and along-flow vertical structures of the WWB. Across the WWB (Fig. 2.6a), easterly winds dominated the WNP basin, except for the WWB that was confined below 500 hPa with the peak magnitude near 900 hPa. Associated with the WWB were the two lower-tropospheric cyclonic vortices exhibiting peak magnitudes at the interface of the westerly and easterly flow. An along-WWB vertical cross section clearly shows a westward tilt of the WWB with

height (Fig. 2.6b). At 900 hPa, the leading edge of the WWB extended to near 158°E, but only to 138°E at its uppermost location. The westward vertical tilt explains the development of a closed 600-hPa circulation (Fig. 2.3e) over 1000 km to the west of the 900-hPa counterpart. The coherent vorticity structure north of the WWB (Fig. 2.6b) suggests that *the two circulations (i.e., at 900 and 600 hPa) could be considered as part of the same vertically-tilted vortex*, which developed in the presence of large scale easterly vertical shear (Fig. 2.6b). Note that the converging zonal winds at the leading edge of the WWB (Fig. 2.6b) favored wave accumulation, as will be discussed in section 2.5 in the context of the formation of the pre-Chanchu vortex.

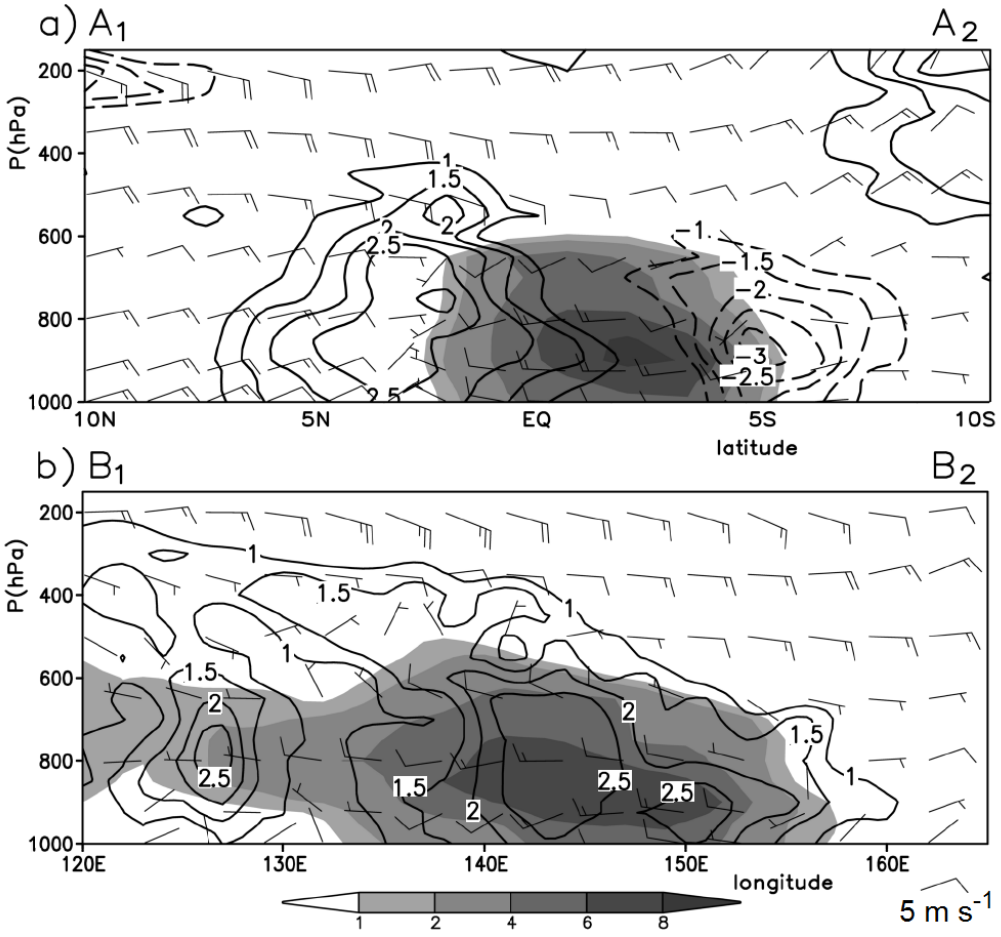

Figure 2.6. Vertical cross sections of horizontal wind barbs (a full barb is 5 m $s^{-1}$) and the vertical relative vorticity (contoured at intervals of ±1, 1.5, 2, 2.5, and 3 x $10^{-5}$ $s^{-1}$), as shown in Fig. 2.5, with westerly flows shaded (m $s^{-1}$), that are taken (a) across the composite WWB (i.e., lines $A_1 - A_2$), and (b) along the axes of the WWB (lines $B_1 - B_2$) and through the pre-Chanchu vortex (line $B_{1a} - B_{2b}$). Solid (dashed) contours denote positive (negative) relative vorticity, and only the positive values in (b) are shown. Note that in (b) only the relative vorticity field is taken along ($B_{1a} - B_{2b}$) in order to show the WWB-associated vorticity field. Fields are calculated as a five grid point slice-average.

In summary, the development of Chanchu could be traced back more than a week prior to its classification as a depression. It formed at the leading portion of the WWB associated with the eastward propagation of the MJO, and its associated vortex exhibited a westward tilt in the vertical. The ongoing processes during this pre-genesis period, particularly those non-observable from the large-scale analyses, are the subject of many unanswered questions about TCG. The subsequent sections describe a cloud-resolving simulation of this pre-genesis portion of Chanchu that is performed to replicate the above-observed evolution and attempt to gain insight into the processes by which the vertically tilted WWB-vortex could transition into an intense typhoon.

### *2.3. Model description*

The current study utilizes Version 2.2 of the Advanced Research WRF (WRF-ARW, Skamarock et al. 2005) to simulate for a period of 11 days the pre-genesis and genesis of what would eventually become Super Typhoon Chanchu (2006), at the finest cloud-resolving resolution of 2 km. The model physics schemes used include (i) the Lin et al. (1983) cloud microphysics scheme (Tao et al. 1993), which contains six classes of water substance (i.e., water vapor, cloud water, rain, snow, graupel, and cloud ice); (ii) the Yonsei University planetary boundary layer (PBL)

parameterization with the Monin-Obukhov surface layer scheme (Hong et al. 2006); (iii) the rapid radiative transfer model (RRTM) for long waves with six molecular species (Mlawer et al. 1997) and the Dudhia scheme for shortwave radiation; and (iv) a modified version of the Kain-Fritsch (1993) cumulus parameterization scheme for the outer 3 domains in which deep convection and a broad range of shallow convection are both parameterized. Note that no cumulus parameterization is used in the 2-km resolution domain.

Fig. 2.7 shows schematically the WRF model setup, which consists of a quadruply-nested telescoping configuration. Three stationary outer domains A, B, and C have the (x, y) dimensions of 100 × 134, 175 × 136, and 313 × 235 grid points with the grid lengths of 54, 18, and 6 km, respectively; and a moving inner domain D with dimensions of 301 × 301 grid points is used to follow the center of Chanchu at the grid length of 2 km. All domains have 40 vertical sigma levels, and they are 1, 0.993, 0.983, 0.97, 0.954, 0.934, 0.909, 0.88, 0.814, 0.753, 0.695, 0.641, 0.590, 0.542, 0.497, 0.455, 0.416, 0.379, 0.345, 0.313, 0.283, 0.256, 0.230, 0.206, 0.184, 0.163, 0.144, 0.126, 0.110, 0.095, 0.081, 0.069, 0.057, 0.047, 0.037, 0.028, 0.020, 0.013, 0.006, and 0. The model top is defined at 30 hPa.

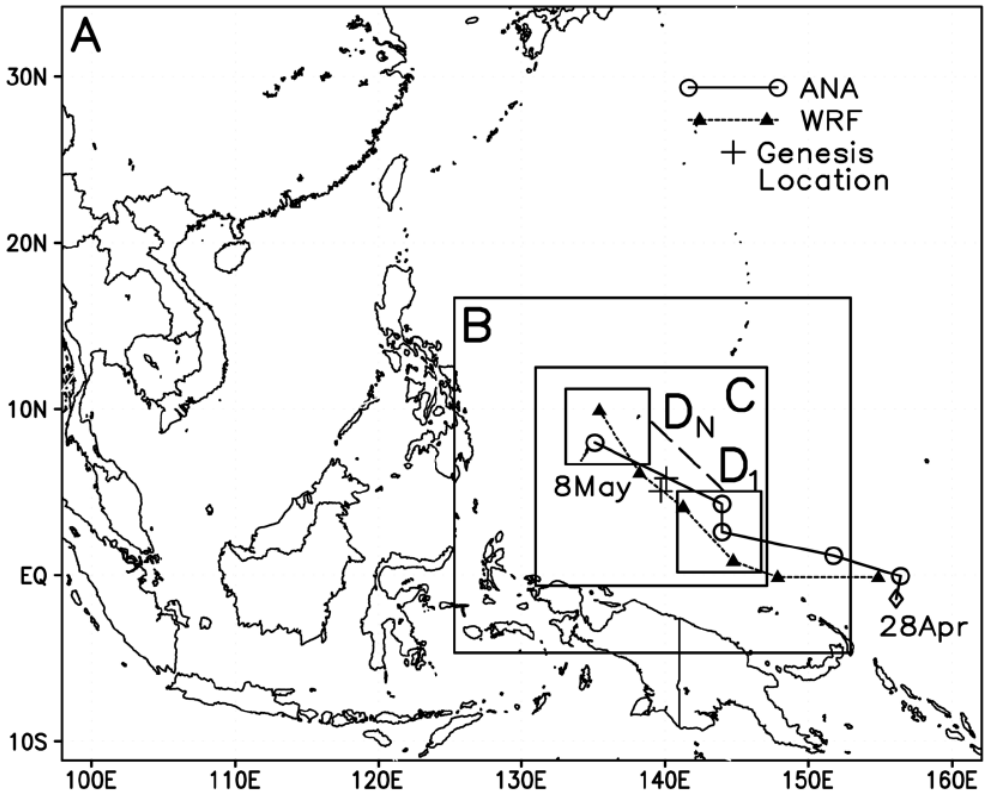


Figure 2.7. Configuration of the nested WRF model domains. Domains A, B, and C remain fixed, while domain D moves with the storm along the dashed line between $D_1$ and $D_N$. The observed (solid with open circles) and simulated (dotted with filled triangles) tracks are shown at 2-day intervals from 28 April to 08 May 2006. The observed April 28 marker is diamond-shaped to denote the absence of a closed circulation, and it is placed at the location of peak vorticity near the 900 hPa trough. Symbols "+" along each track denote the approximate location of Chanchu's genesis.

The integration proceeds via a staggered initiation of the nested domains, in which Chanchu is allowed to spin up within each domain before a new domain is initiated. The simulated Chanchu is not permitted to cross the boundary of any nest at any time, and care is taken to prevent the initialization of any nest when precipitation is occurring near the boundaries. The outermost domain (A) is initialized at 0000 UTC 27 April 2006. Domain B begins 4 days later, i.e., at 0000 UTC 1 May. Domain C is activated at 1200 UTC 2 May, and domain D 12 h later at 0000 UTC 3 May. The 11-day simulation is chosen to capture different stages of the genesis of Chanchu,

including the earliest large-scale formation of a WWB associated with the MJO (domain A), the mesoscale pre-genesis (domains B and C), and the storm-scale genesis (domain D). Due to the two-way interactive nature of the nests, we may use only the results from domain A to examine the large and mesoscale flows in Chapter 2 without losing the upscale influences of deep convection and the small-scale processes, which we reserve for subsequent studies.

The model initial conditions and the outermost lateral boundary conditions are obtained from the NCEP FNL with the latter updated every 6 hours. No artificial data (e.g., bogus vortices) are used during the 11-day model integration. Sea-surface temperatures (SSTs) are updated daily using NCEP's data (see Fig. 2.1 for the initial SST distribution), though there is no significant TC-induced variation in SSTs during the simulation, as the disturbance remains weak. Note that the outermost domain A is allowed to spin up from the raw initial conditions, in which the WWB has not yet moved across PNG and the pre-Chanchu disturbance has not yet developed into a closed circulation at any vertical level.

### *2.4. Model verification*

In general, it is not surprising that the WRF model could reproduce well the large-scale features. Thus, in this section we compare the 11-day WRF simulation to available observations of the track, intensity, and some major structures of the pre-Chanchu disturbance. Fig. 2.7 shows that the model reproduces reasonably well the observed track, which was obtained by taking the location of the 900-hPa circulation center from the NCEP FNL prior to Chanchu's depression stage and the JTWC's best track analysis afterward. The simulation captures the formation of a low-level

disturbance evident on 28 April near the equator at 155°E, and its subsequent west-northwestward translation up to May 8.

While the observed disturbance remains quasi-stationary for about 2 days (i.e., April 28-30), the simulated disturbance moves immediately westward. On 2 May, the simulated near-equatorial disturbance is displaced about 800 km to the west of the observed. After 2 May, both the simulated and observed disturbances begin to move northwestward away from the equator, in concert with the WWB (cf. Figs. 2.7 and 2.3), until the end of the 11-day simulation on 8 May. At the final time, the simulated storm exhibits a track error of roughly 200 km northward compared to the observed. Despite these differences, especially for the premature westward translation, we may claim that the WRF model reproduces reasonably well both the formation near the equator and subsequent movement of the pre-Chanchu disturbance for a period of 11 days. This indirectly confirms that the larger-scale flows, in which the weak disturbance evolves, are reasonably simulated.

The JTWC began to estimate the intensity of the pre-Chanchu disturbance on May 7, and their report suggests that the minimum pressure remains above 1000 hPa until 8 May (not shown) when the observed storm could be classified as a tropical depression. Fig. 2.8 shows that the simulated storm intensity remains nearly constant, with minimum pressure above 1000 hPa during the first 8-day (or 192-h) period, when few observations were available. However, it begins to intensify after the 192-h integration, valid at 0000 UTC 5 May (hereafter 5/00-192), which is more than 2 days earlier than the observed. This simulated early intensification is likely associated with its early west- and northwestward translation during the period of

May 2 – 6 (Fig. 2.7), when the simulated storm reaches its genesis position two days prior to that observed. Nevertheless, the geneses of the observed and simulated storms occur at nearly the same position (i.e., near 140°E, 5°N; see Fig. 2.7). Thus, we may assume that the WRF model also reproduces reasonably well the evolution of the storm intensity during the pre-genesis stage.

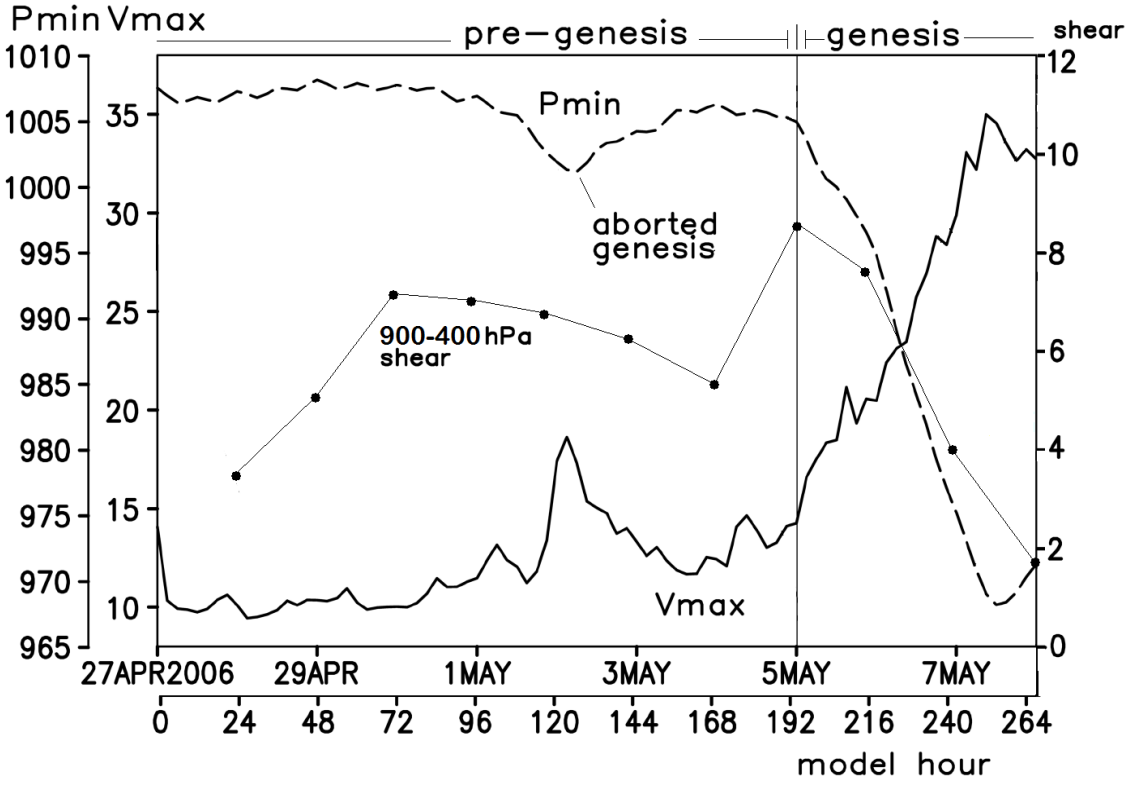


Figure 2.8. Time series of the minimum central pressure ($P_{min}$, hPa, dashed) and the maximum surface winds ($V_{max}$, m $s^{-1}$, solid) at 3-h intervals, from the 11-day (i.e., 0000 UTC 27 April – 0000 UTC 8 May 2006) simulation in Domain A. The vertical wind shear (m $s^{-1}$) between 400 and 900 hPa is also superimposed at daily intervals, which is estimated using an area of 1000 km × 1000 km centered on the 900-hPa circulation center. The thin solid vertical line at 0000 UTC 5 May demarcates the pre-genesis and genesis periods.

Note that the simulated intensity changes, shown in Fig. 2.8, can be clearly divided into two distinct stages, i.e., pre-genesis and genesis stages. During the pre-genesis stage (i.e., April 27 – May 5), the minimum central pressure ($P_{min}$) fluctuates between 1000 – 1007 hPa, and the maximum surface wind ($V_{max}$) fluctuates between

10 – 13 m $s^{-1}$. A noteworthy exception during the pre-genesis stage is a near-equatorial *aborted genesis episode*, i.e., a temporary intensification and subsequent weakening before and after 2/00-120, respectively (Fig. 2.8). It is well known that TCG cannot occur near the equator due to the lack of the planetary vorticity for vortex stretching, but as will be shown in section 2.5, TCG can *temporarily* occur at this time because of increasing deep convection near the center of the pre-Chanchu vortex. The *sustained* intensification stage begins at 5/00-192, which marks the end (beginning) of the pre-genesis (genesis) stage. Subsequently, the storm deepens until 7/12-252 with a 36-hPa drop in $P_{min}$ and an increase in $V_{max}$ to about 35 m $s^{-1}$, just reaching typhoon intensity.

An examination of the large-scale vertical wind shear (VWS) in the 900 – 400 hPa layer indicates that the synoptic environment in which the pre-Chanchu disturbance develops remains relatively favorable for TCG (see Fig. 2.8), with VWS fluctuating between 2 - 9 m $s^{-1}$ during pre-genesis and genesis. The VWS during the early stages of pre-genesis is easterly because the 400-hPa flow over the equatorial region remains easterly (see Fig. 2.6) while the low-level WWB surges eastward. During the later stages of pre-genesis, the VWS shifts to westerly (not shown) due to preferential enhancement of low-level easterly winds in the northern semicircle of the circulation, associated with convection there. Generally, large-scale VWS remains weak and favorable for TCG, especially during the aborted genesis.

Because direct observations of the storm intensity during pre-genesis are not available, we compare in Fig. 2.9 the simulated sea-level pressure and the vertically-integrated cloud hydrometeors to the NCEP FNL and the satellite-observed outgoing

longwave radiation (OLR) during the 11-day integration period. On 30 April, the model produces a loosely closed isobar of 1009 hPa at the equator - a surface manifestation of the pre-Chanchu disturbance, with dense cloud coverage near the circulation center (Fig. 2.9d). Though the simulated circulation translates to the west faster than the observed (cf. Figs. 2.9a and 2.9d), as also indicated in Fig. 2.7, the model does capture the large area of cloud coverage observed to the north and west of the circulation as well as the cloud-free region to the southeast. Since the easterly trades increase with height (Fig. 2.6b), the upper-level hydrometeors tend to be advected downstream of the low-level convergence zone, forming a large area of stratiform clouds and precipitation to the northwest of the vortex (cf. Figs. 2.9d and 2.5).

Note that while the observed 900-hPa wind fields show closed circulations (denoted by "C" and "L" in Figs. 2.9a-c), there are no associated closed surface isobars for either the pre-Chanchu or the southern hemispheric disturbance on 4 May (cf. Figs. 2.3i and 2.9b). Such a poor correspondence between the wind and mass fields is common over the equatorial area. Both the observed (Fig. 2.9b) and simulated (Fig. 2.9e) maximum cloud coverage shifts from the western to the northern portion of the vortex during 30 April – 4 May. Meanwhile, a cloud-free area develops to the south, suggesting large-scale dry intrusion and subsidence to the south of the vortex. Although the southern vortex evolves in close proximity to land with little intensity changes, the simulation captures well its associated cloud field on 4 May (Fig. 2.9e).

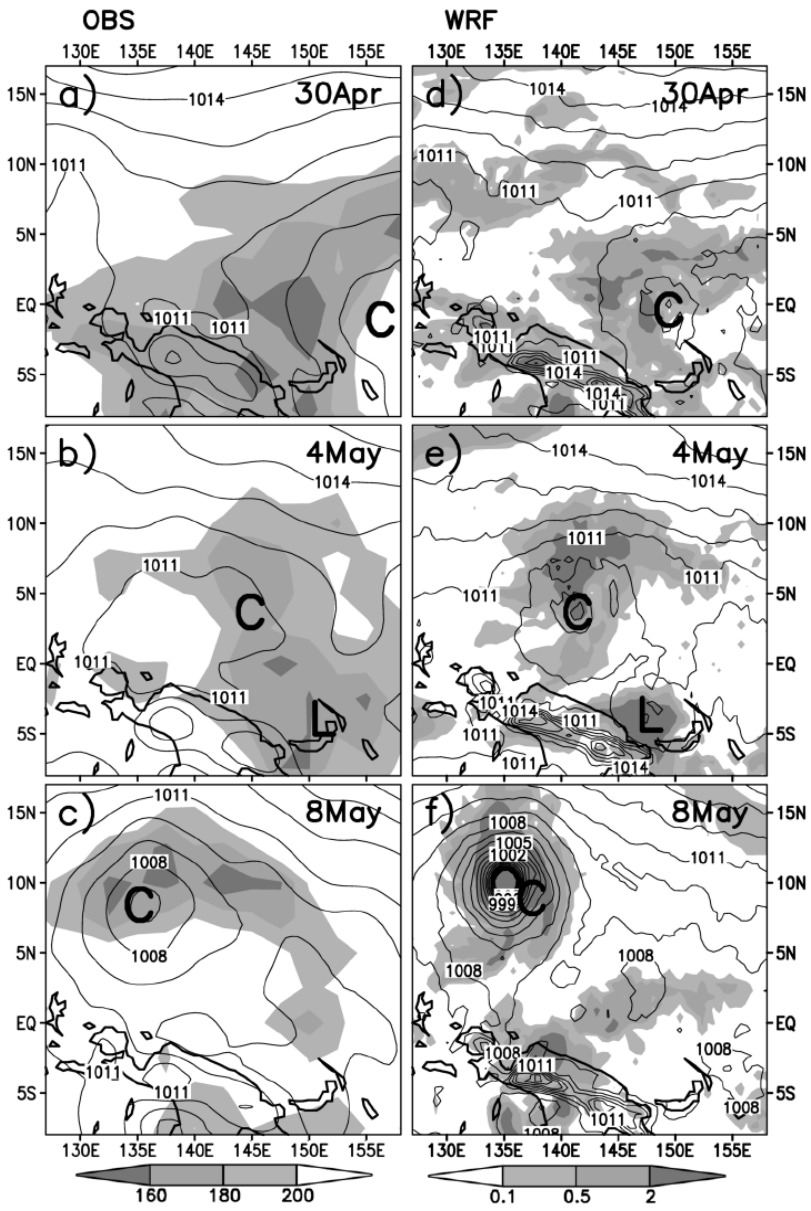


Figure 2.9. Comparison of (a) – (c) the observed outgoing long-wave radiation (OLR, W $m^{-2}$, shaded left panel) at the top of cloud columns to (d) – (f) the simulated vertically mass-weighted cloud hydrometeors (g $kg^{-1}$, shaded, right panel), and superimposed with contours of the sea-level pressure (every 1 hPa) at four-day intervals during the period of 0000 UTC 30 April (top) – 8 May (bottom) 2006. Fields in (d) – (f) are averaged during a 12-h period. OLR data source: ftp://ftp.cdc.noaa.gov/Datasets/interp_OLR/olr.day.mean.nc

By 8 May both the observed and simulated storms exhibit easily identifiable centers in the sea-level pressure fields as they eject poleward and continue to intensify. The simulated Chanchu is much more intense than the observed on 8 May

due to its premature intensification. However, despite the differences in intensity and some differences in the cloud coverage between the simulation and observations, their general agreements lends credibility to the 11-day simulation of the larger-scale environment.

### *2.5. Formation and evolution of the pre-Chanchu vortex*

In this section we discuss in chronological order the formation of the closed pre-Chanchu circulation, the implications of the vertical tilt, the processes associated with the aborted genesis, and finally the transition of the tilted WWB-vortex to an upright TC.

#### *2.5.1. The formation of a closed TC circulation*

Understanding the origin of low-level disturbances is a challenging problem, and thus most TCG studies focus only on the amplification of pre-existing disturbances. In the present case, the eastward progression of the WWB appears to account directly for the formation of the pre-Chanchu disturbance. Although the MJO owes its existence to large-scale deep convection, the WWB and its associated vortices can be maintained in the absence of deep convection, at least within this regional simulation. This is confirmed by a sensitivity simulation in which the effect of latent heating is turned off, hereafter referred to as the DRY run, while holding all the other conditions identical to the control run shown in section 2.4. It is found that the incipient disturbance in DRY forms at nearly the same location as that in the control run, but it fails to intensify (not shown), as expected.

To help visualize the formation of the pre-Chanchu disturbance, Fig. 2.10 shows a 3-day (i.e., 27/06-06 - 30/06-78) window of the simulated low- and mid-level flows

in the vicinity of the WWB. In general, the model captures the eastward progression of the WWB (Figs. 2.10e-h), an inverted trough at both 600 (Fig. 2.10a) and 900 hPa (Fig. 2.10e), and the eventual development of closed circulations during this 3-day period (Figs. 2.10d,h). Note that the inverted trough is already present in the model initial conditions due to the preexistence of the WWB (not shown), but it is quite weak. Note also that a short easterly wave (SW) approaches the WWB-related trough axis from the east at 28/06-30 (Fig. 2.10f). According to Chang and Webster (1990), any wave approaching a major trough tends to congregate its associated cyclonic vorticity at the trough axis, serving to amplify the trough. This phenomenon is apparent between 28/06-30 and 29/06-54 (Figs. 2.10f,g) as the SW approaches the primary trough axis from the east.

Figs. 2.10i-l show at higher time resolution the formation of the closed circulation at 900 hPa, which develops by 29/03-51 to the northeast of PNG where the SW merges into the preexisting trough axis. This suggests that *the initial closed circulation in the lower troposphere forms through the wave accumulation process*. While deep convection may contribute to the SW intensity at earlier times, it is not essential for the formation of the low-level closed circulation since it also occurs in the DRY simulation (not shown). As the WWB continues to penetrate eastward, the incipient 900-hPa disturbance progresses west-northwestward under the influence of the easterlies, with precipitation concentrated to the northwest of the 900-hPa center (Fig. 2.10h).

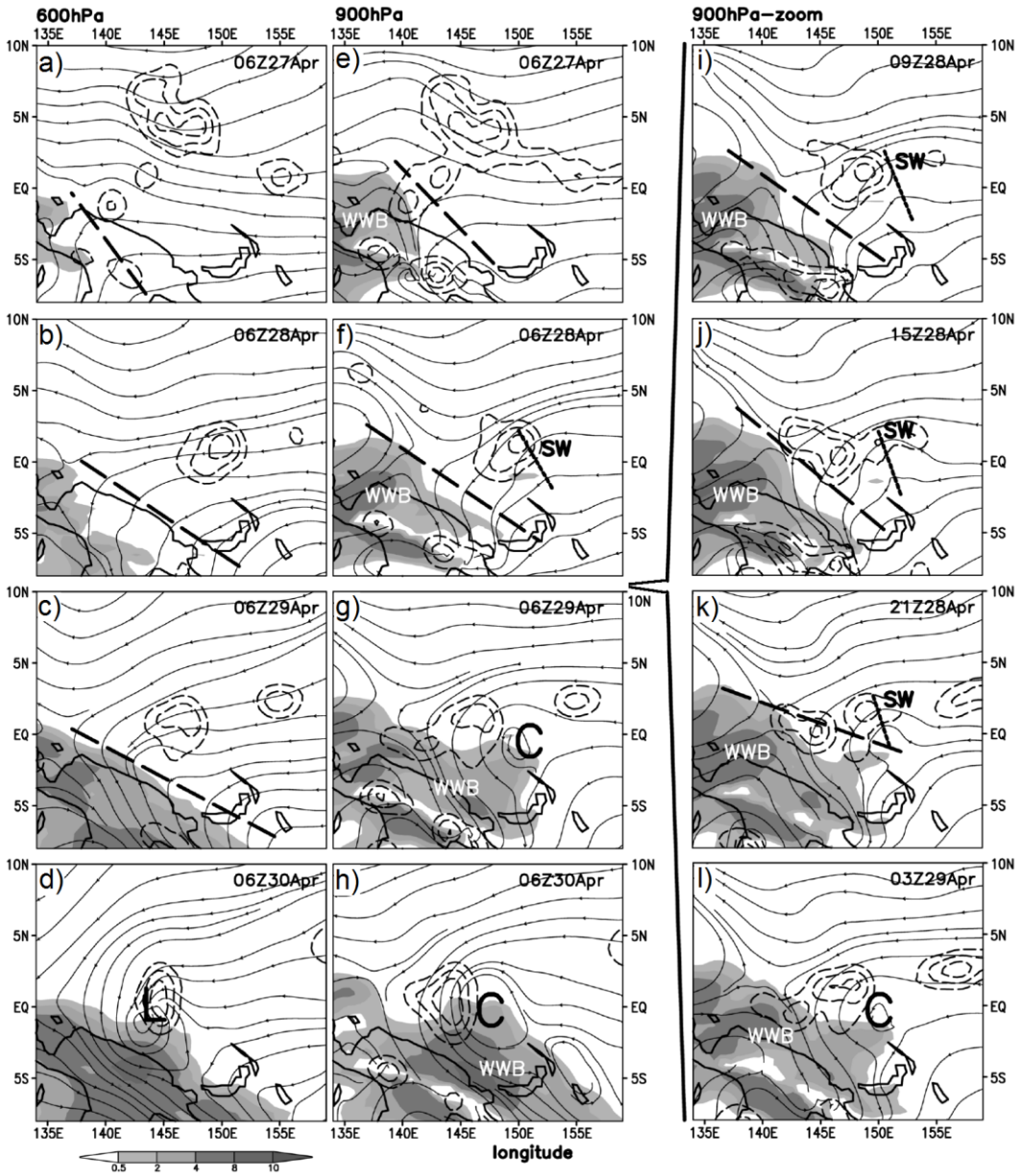


Figure 2.10. As in Fig. 2.3 for the two left panels (a) – (h), but with radar reflectivity (dashed contours at 5, 15, 25 dBZ) from 0600 UTC 27 (top) to 0600 UTC 30 (bottom) April 2006 at daily intervals. In the right panel, as in (e) – (h), but at 6-h intervals during 0900 UTC 29 (i) – 0300 UTC 30 April (l). Heavy dashed (dotted) diagonal lines denote major trough (short wave, SW) axes. Symbols "C" ("L") represent pre-Chanchu closed circulations at 900 hPa (600 hPa). Fields in the left panels (right panel) are averaged during a ±6-h (3-h) period.

Although the SW does not show a clear signal in the 600-hPa streamlines (cf. Figs. 2.10b and 2.10f), its precipitation field approaches the preexisting trough axis in a manner similar to that at 900 hPa but at a later time. That is, a closed cyclonic

circulation does not occur at 600 hPa until 30/06-78 (Fig. 2.10d), which is 21 h later than that seen at 900 hPa due to the phase difference between the two levels. Both circulation centers develop roughly on the equator (Figs. 2.10d,h). In the DRY simulation, an inverted trough exists at 600 hPa at 30/06-78, but it does not exhibit a closed circulation (not shown). Thus, the distribution of a large area of mostly stratiform precipitation near the trough axis (Fig. 2.10d) suggests an important role of midlevel convergence in stretching the preexisting vorticity for the formation of the pre-Chanchu vortex. This will be detailed in Chapter 3.

*2.5.2. Effects of the vertically tilted vortex*

An important characteristic of the tilted WWB-vortex is that significant upward motion and deep convection occur exclusively on the downtilt-right side of the vortex, i.e., to the right of the upward tilt (Fig. 2.10h). Little attention has previously been given to the relationship between the tilted vortex, convective organization and TCG. Fig. 2.11b shows that the tilted WWB vortex is characterized by a dipole of the vertically tilted potential temperature anomalies ($\theta$'), with a positive $\theta$' layer above a negative $\theta$' layer. Such a vertical thermal structure is hydrostatically consistent with a tilted low-pressure system that coincides *roughly* with the distribution of the vortex circulations. We believe that some mass-wind adjustment, though occurring at a (weekly to monthly) timescale much longer than that typically at higher latitudes, could still account for the generation of the tilted *synoptic-scale* vortex, given the thermal structures, or vise versa, over the equatorial region. Of course, this hypothesis should not be operative near the equator. In fact, the low-level sub-synoptic flows, similar to those given in Fig. 2.11a, are nearly 90° across isobaric over the low-

pressure system underneath the elongated warm θ-anomaly to the north-northwest of $L_{900}$ (see Fig. 2.11a). This indicates that the balanced dynamics could not be applied to features at the sub-synoptic scale or shorter timescales herein.

Of interest is the phase relationship between the thermal anomaly, upward motion and precipitation along any cyclonic streamline within the vortex (Fig. 2.11a). The distribution of precipitation to the west of the elongated warm anomaly suggests that the warming results likely from convectively generated compensating subsidence through the returning updrafts, often associated with pre-squall mesolows or troughs (see Hoxit et al. 1976; Fig. 3b in Zhang and Gao 1989). This subsidence argument is further confirmed by the dry run in which the warm anomaly is only limited to the vicinity of the vortex center.

A natural question one may ask is: Why is deep convection favored to the north but not the south of the vortex? An examination of the equivalent potential temperature ($\theta_e$) field reveals the presence of higher-$\theta_e$ air in the incoming PBL easterly flow to the north than that in the westerly flow to the south of the vortex (not shown). Clearly, the resulting θ-anomaly tends to cause isentropic ascent after air parcels pass the positive θ' ridge axis, enhancing the uplifting of the incoming high-$\theta_e$ air. The cyclonic-downstream advection of cloud/precipitation particles and their subsequent evaporative cooling would induce moist downdrafts, enhancing the cold anomaly underneath the middle portion of the tilted vortex (cf. Figs. 2.11a,b). This, in addition to isentropic descent after passing the negative θ' ridge axis, diminishes the likelihood of convective development on the downtilt-left side of the vortex.

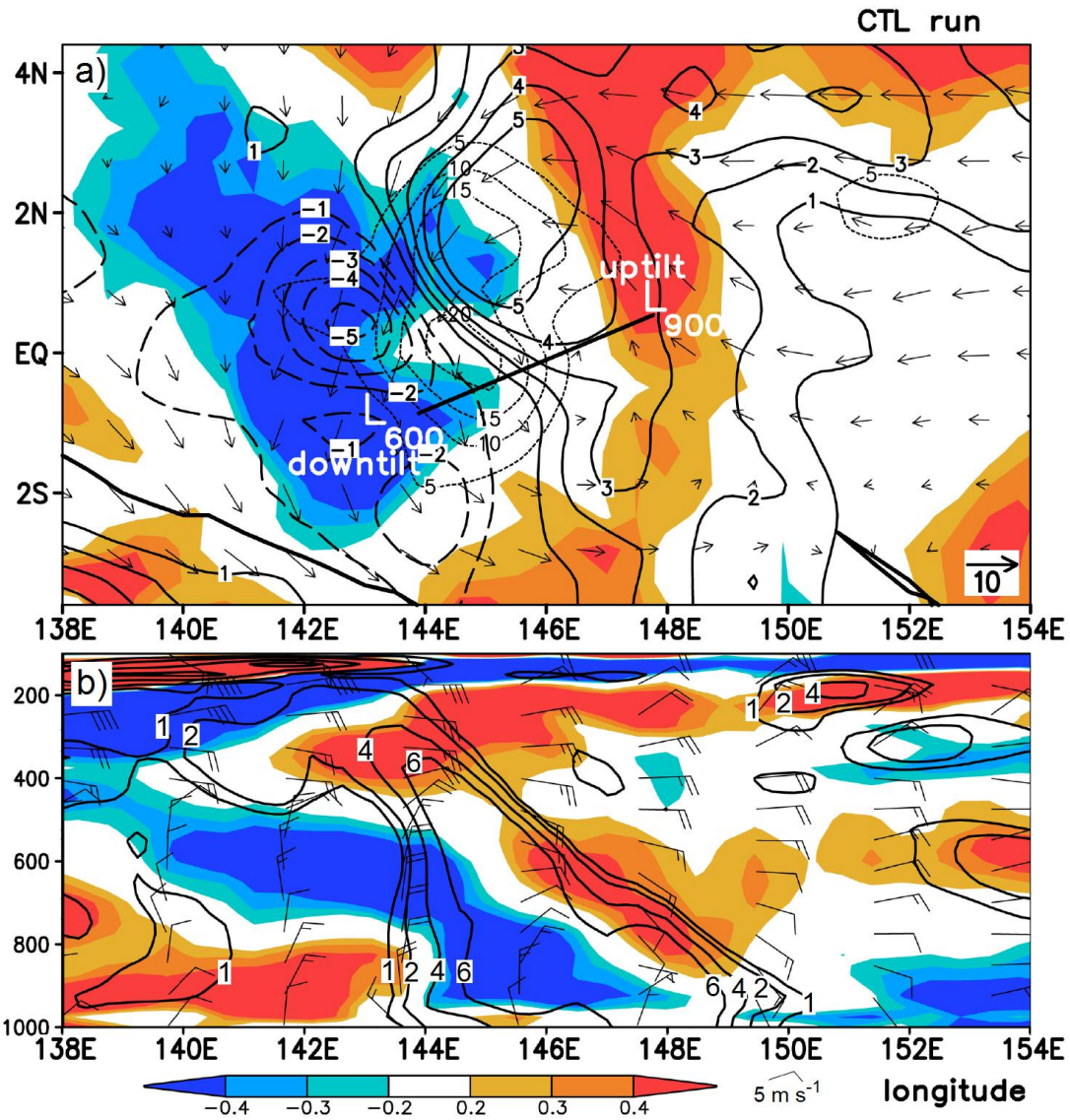


Figure 2.11. (a) Horizontal distribution of the simulated mean potential temperature (θ) anomalies (K, shaded), radar reflectivity (dotted, every 5 dBZ), and vertical motion (solid/positive, dashed/negative, every 1 cm $s^{-1}$) at 700 hPa, valid at 0600 UTC 30 April (±3-h time mean). Horizontal wind vectors (700 hPa) and the vortex tilt (heavy solid line) between 600 hPa ($L_{600}$) and 900 hPa ($L_{900}$) are shown. (b) As in (a) but for the west-east vertical cross section along the equator of θ-anomalies (shaded), relative vorticity (solid contours at 1, 2, 4, and 6 x $10^{-5}$ $s^{-1}$), and horizontal wind barbs.

Note that the above-mentioned thermal and vertical motion relationship resembles that of the isentropic ascent (descent) on the downtilt-right (-left) side of an idealized TC-like vortex by Jones (1995). However, the two differ substantially in horizontal scale, degree of vertical tilt, and more importantly dynamic mechanisms

(i.e., dry vs. moist, barotropic vs. baroclinic, balanced vs. equatorial). The rainfall generation mechanism is also distinct from that in mature TCs exhibiting enhanced upward motion on the downshear side (Zhang and Kieu 2006) and more clouds/precipitation on the downshear left side (Frank and Ritchie 1999; Black et al. 2002).

Because of the convectively generated lower surface pressures, the low-level vortex center tends to move north-northwestward. Meanwhile, convectively generated upright vortices, to be examined in Part II of this series of the papers, increase the midlevel cyclonic vorticity to the north, and tend to "absorb" the background vorticity associated with the WWB-vortex through horizontal convergence, thereby leading to an increasingly vertically erect vortex that could commence intensification as an upright TC. In their study of westward-tilting equatorial MRG waves during the MJO, Dickinson and Molinari (2002) found that precipitation occurred to the north of the waves, causing their "transition" into TD-type disturbances, but no mechanism for the "transition" was discussed. Thus, the results herein suggest that the tilted WWB-vortex interacting with the moist easterly flows in the PBL could provide a favorable environment for the organization of deep convection to the north, and it is deep convection that plays an important role in vertically aligning the cyclonic circulations, causing the genesis of Chanchu.

*2.5.3. The aborted genesis*

Although it is not possible to validate the aborted genesis, it is of interest to examine why TCG could temporarily occur near the equator and why it is later aborted. Prior to the aborted genesis at 1/15-111, the tilted vortex is characterized by

an elongated area of precipitation in its northern semicircle (Fig. 2.12e). Thus, the genesis scenarios similar to those discussed in the preceding subsection appear during the 1/15-111 – 2/18-138 period, including the increased midlevel cyclonic vorticity by deep convection north of the surface low, and the absorption of the WWB-vortex related vorticity. As a result, the vortex becomes nearly upright by 1/15-111, in association with an inner-core convective band that develops in a convergence zone about 30 km to the north of the vortex center (see Fig. 2.12f). Because the latent heating occurs in the inner-core region, it is much more effective in spinning up the vortex than that in the outer region (Hack and Schubert 1986). It is important to note that even though the midlevel circulation center becomes nearly upright with its low-level counterpart in the vicinity of the convective band, the outer regions of the vortex continue to exhibit vertical tilt, as indicated by the highly asymmetric circulation at 600 hPa. Thus, the tilted WWB-vortex continues to support precipitation generation on the downtilt-right during the aborted genesis period (Fig. 2.12). Almost no precipitation occurs to the south of the vortex, i.e., downtilt-left.

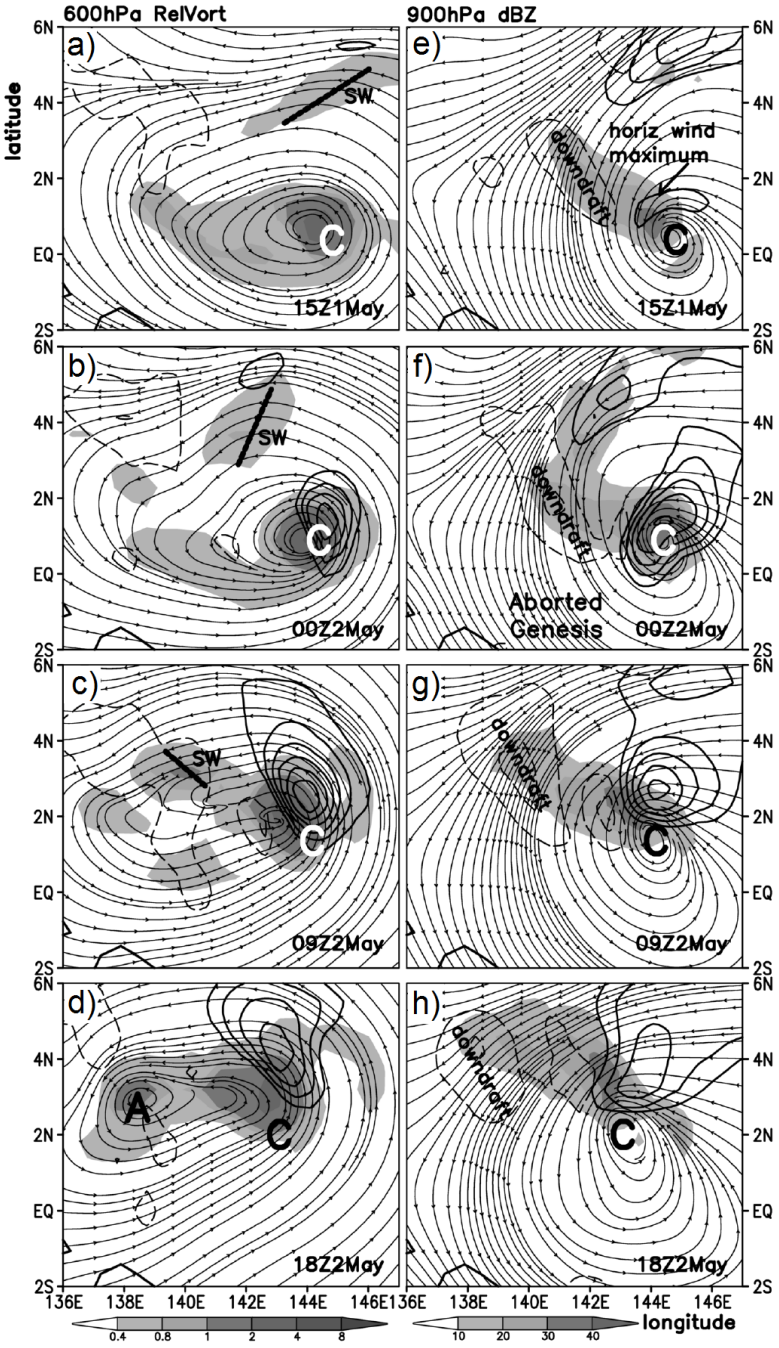


Figure 2.12. Horizontal distribution of (a) – (d) 600-hPa relative vorticity (shaded, x $10^{-5}$ $s^{-1}$) and (e) – (h) 900-hPa radar reflectivity (shaded, dBZ) at 9 h intervals, from 1/15-111 (top) – 2/18-138 (bottom) and superimposed with streamlines during the aborted genesis. Horizontal wind magnitude (thick solid contours at 14, 15, 16, 17, and 18 m $s^{-1}$), and descending moiton (light dashed contours at 1, 5, 10, 20, 40 cm $s^{-1}$) are shown. Symbol, "C" denotes the center of the 900-hPa closed circulation, and the heavy solid line in (a) – (c) denotes the location of a SW, which develops into 600-hPa closed circulation "A". Fields are averaged within a ±3-h period and a ±50-hPa layer.

As convection intensifies in the inner-core region, the maximum tangential winds increase rapidly (about 30 - 40%) in a deep layer between 1/15-111 and 2/00-120 (Fig. 2.12e,f), while $P_{min}$ falls from 1005 hPa to nearly 1000 hPa (Fig. 2.8). With the nearly upright vortex structure and organized deep convective bands in the inner-core regions, one may expect the beginning of TCG at 2/00-120 (Fig. 2.12b,f). However, the convective band weakens shortly after 2/00-120 due likely to the spread of cold downdraft air into the core region. That is, the intrusion of dry northwesterly flow causes evaporation of hydrometeors, which in turn induces mesoscale downdrafts in the trailing regions of the convective band (Figs. 2.12e-g), thereby aiding in the suffocation of deep convection in the inner-core region. Although the magnitude of moist downdrafts at 900 hPa in the trailing stratiform region is generally less than 10 cm $s^{-1}$ during the aborted genesis (Fig. 2.12f), they cover a large area of the western half of the vortex. Of course, TCG is not generally favored at such low latitudes (~1ºN).

Once the inner-core deep convection weakens (Fig. 2.12g), convectively generated cyclonic vorticity tends to be advected within the larger-sized tilted pre-Chanchu vortex, especially at the mid- and upper-levels (Figs. 2.12c,d), and thus an increased vertical tilt appears again. Meanwhile, outside of the core region, another shortwave becomes trapped within the midlevel circulation during the aborted genesis, assisting in the formation of a new closed vortex circulation "A" at 2/18-138 within the pre-Chanchu vortex (Fig. 2.12d). As a result, a broad west-east oriented elliptically-shaped midlevel vortex is situated northwest of the low-level circulation center (Figs. 2.12d and 2.12h).

*2.5.4. Relationship between vertical tilt and TCG*

Fig. 2.13 shows the subsequent evolution of the pre-Chanchu disturbance after the aborted genesis, ultimately leading to sustained genesis. At 2/21-141, i.e., 21 h after the aborted genesis (cf. Figs. 2.12b,f and 2.13a), the vortex still exhibits a significant westward vertical tilt with a distance of about 500 km between the 900- and 600-hPa circulation centers, and deep convection with a large area of trailing stratiform precipitation confined on its downtilt-right side. However, the major rainband, to be detailed in Chapter 3, is shifted far away from the 900-hPa circulation center (Fig. 2.12h) and not as intense as that occurring during the aborted genesis. In the upper troposphere, easterly and southeasterly flows are diffluent (Fig. 2.13e) and generally favorable for TC intensification when combined with the vertical shear of below 10 m $s^{-1}$ (Fig. 2.8).

By 3/15-159 (Fig. 2.13b), the orientation of the vortex tilt becomes more northwest-southeast (cf. Figs. 2.13a,b or 2.13h) as a result of differing movements between the low and midlevel circulations. That is, as discussed before, the convectively generated vortices (or lower pressures) steer the surface low northwestward, while the convectively generated midlevel vortices, or MCVs to be discussed in Chapter 3, tend to force the midlevel circulations to move northeastward. Thus, the distance between the lower and midlevel circulation centers, i.e., the vertical vortex tilt, decreases with time as long as the convective bands and associated stratiform regions can be maintained on the downtilt-right side. At 250 hPa, convective blocking leads to the northward deflection of the incoming easterly flow and pronounced diffluence behind the convective bands (Fig. 2.14f).

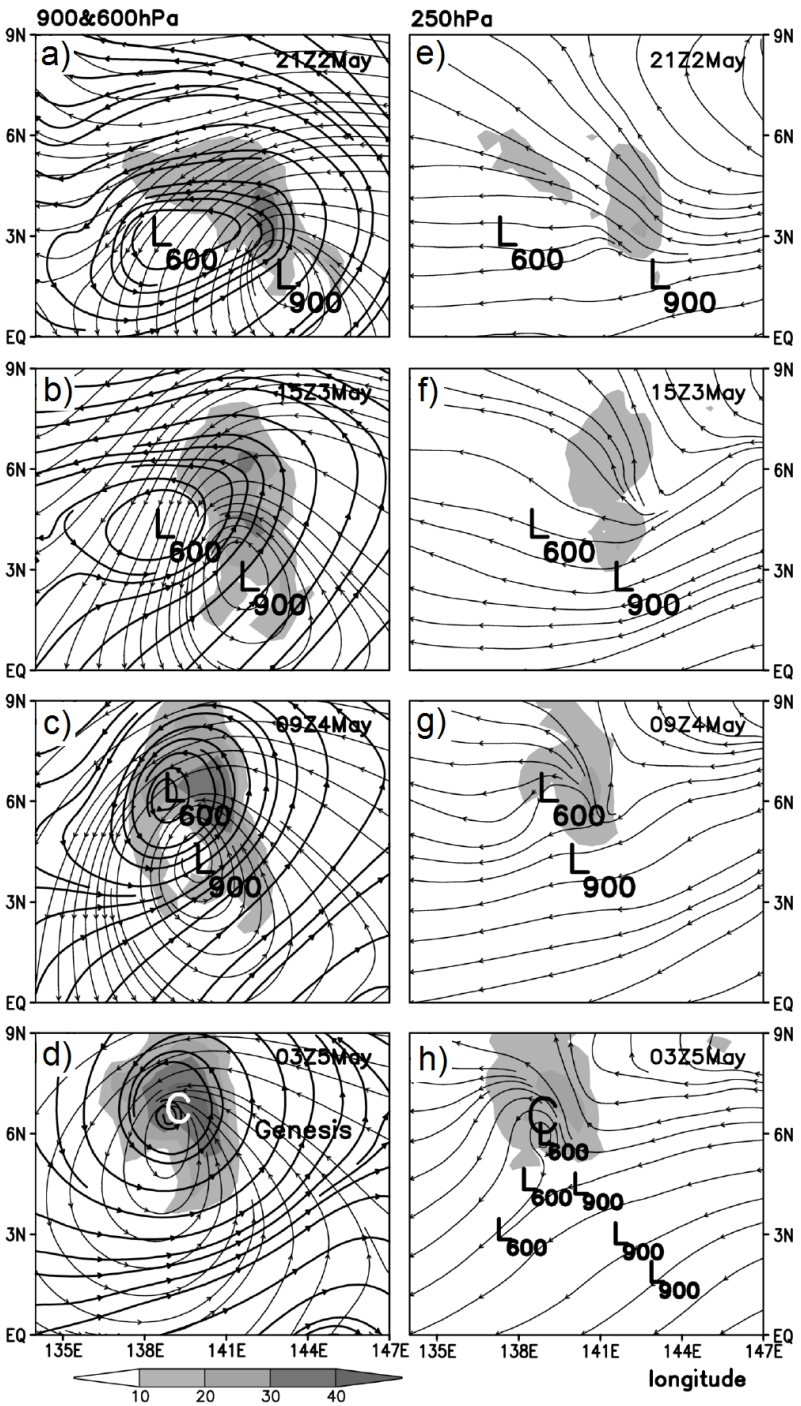


Figure 2.13. Horizontal distribution of the radar reflectivity (shading, dBZ) and streamlines at (a) – (d) 900 hPa and (e) – (h) 250 hPa from 2/21-141 (top) – 5/03-195 (bottom) at 18 h intervals. In (a) – (d) 600-hPa streamlines are superposed to show the diminishing vertical tilt of the pre-Chanchu vortex. The 600- and 900-hPa circulation centers are denoted by "$L_{600}$" and "$L_{900}$," respectively, until the genesis of Chanchu ("C") has commenced.

Subsequently, as the vertical tilt diminishes at 4/09-177, precipitation begins to wrap into the midlevel vortex (Fig. 2.13c), accelerating its spinup. By 5/03-195, the vortex becomes vertically coherent (Fig. 2.13d), nearly at the same time as the steady decrease in $P_{min}$ commences (Fig. 2.8), signifying the beginning of TCG. A closed vortex circulation even could be seen at 250 hPa at this time (Fig. 2.13h). Note that even though the circulation *centers* are vertically coherent from 900 to 250 hPa, significant 900 – 600-hPa vertical shear (Fig. 2.13d) still exists in the far-field flow. The earlier rainband appears now as a spiral band, and the southern semicircle remains nearly precipitation-free as the previously distinct regions begin to intertwine. To summarize, the final two days of pre-genesis can be characterized by an increasingly vertically upright, northward moving vortex (i.e., from 900 to 250 hPa) as determined by the development of deep convection in the northern semicircle of the pre-Chanchu disturbance, leading to the surface cyclogenesis by 5/00-192 (Fig. 2.13h).

### *2.6. Summary and conclusions*

In this study, the larger-scale structures and evolution prior to and during the genesis of Typhoon Chanchu are analyzed in the context of the early 2006 tropical season using NCEP's FNL, satellite observations, and 11-day numerical simulations with the WRF-ARW model. It is found that the MJO, likely influenced by an eastward-propagating Kelvin wave, provided the necessary low-level convergence and rotation for the development of a precursor disturbance, particularly through a WWB that propagated near the equator from the Indian Ocean into the Pacific Ocean during late April 2006. It is shown that the 11-day simulation captures well many

larger-scale features during the formation of Chanchu, including the propagation and structure of the WWB, the initial spinup of the pre-Chanchu disturbance at the eastern periphery of the WWB, and the general track and intensification of Chanchu. Although the simulated intensification begins two days prior to that observed, genesis occurs at nearly the same location along the track.

Fig. 2.14 shows a conceptual model of several larger-scale processes leading to the genesis of Chanchu (2006), based on both the observations and model simulation. First, an eastward-moving WWB associated with the MJO facilitates the development of a westward tilted cyclonic disturbance where the WWB interfaces with the easterly trades (Fig. 2.14a). Barotropic mechanisms likely play an important role in the formation of the closed circulation associated with the vertically tilted pre-Chanchu disturbance. Second, the tilted WWB-vortex interacting with the moist easterly flows in the PBL assists in the organization of deep convection on its downtilt-right side. Moreover, the vortex circulations at individual levels deviate northward toward the area of ongoing deep convection and associated enhanced vorticity, causing a decrease in the vertical tilt with time. Third, sustained surface cyclogenesis commences as the vortex becomes upright in the vertical (Fig. 2.14c), despite the fact that the periphery still remains tilted and the northern convection continues as a spiral rainband.

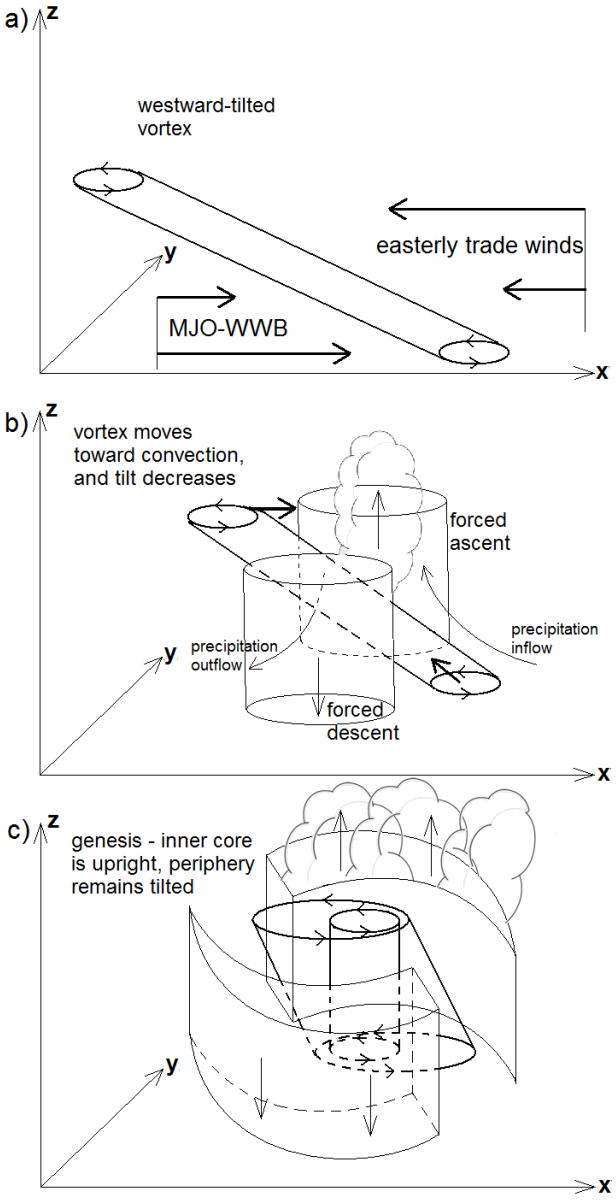


Figure 2.14. Conceptual model for (a) the development of a westward-tilted vortex at the interface of the WWB and easterly trades, (b) its associated ascent (descent) on the downtilt-right (downtilt-left) side and the distribution of deep convection on the downtilt-right of the vortex, and (c) the final vertical alignment of the vortex centers leading to the self-sustained genesis.

Although previous studies have shown the westward-tilted structure of the MJO/WWB (e.g., Sperber 2003) and associated Kelvin waves (Straub and Kiladis 2003) in the West Pacific, few have discussed the implications of the tilt on TCG. Of

particular importance are the processes, associated with the diabatic heating on the downtilt-right side, that precede the transition of the precursor tilted vortex into a vertically coherent tropical cyclone. A comparison with a dry sensitivity simulation suggests that the diabatic heating indeed plays an important role in determining the northward deviation. Note that this study serves to establish a baseline for the genesis of Chanchu using only the coarse mesh of the quadruply-nested simulation. In Chapter 3 of this dissertation, we will conduct analyses of mesoscale processes ongoing during the final two days of pre-genesis using the finer nested simulation dataset, with the goal of clarifying the evolution of the northern convective processes and their impact on impending TCG.

# Chapter 3: Mesoscale evolution of precipitation and tropical transition of the baroclinic vortex

## *3.1. Introduction*

Tropical cyclogenesis (TCG) remains an enigmatic phenomenon because many of the processes that precede genesis are not well observed at the mesoscale. While the pre-conditions for TCG are well established (e.g., Gray 1998) and persist year round in the Western North Pacific (WNP), the organization of deep convection that precedes and causes TCG is not yet well understood. However, as our ability to observe the tropical atmosphere has improved over the years, much progress has come toward the understanding of TCG at smaller scales.

Recent observational and modeling studies view TCG as a stochastic phenomenon (Simpson et al. 1997) involving various mesoscale interactions that lead to the upscale growth of cyclonic vorticity and eventually result in a self-sustaining surface cyclonic circulation. Ritchie and Holland (1999) found that almost all TCG cases in the West Pacific develop in association with at least one mesoscale convective system (MCS), which can often spawn mesoscale convective vortices (MCVs) (Zhang and Fritsch 1987; Bartels and Maddox 1991; Fritsch et al. 1994; Harr and Elsberry 1996). MCVs often persist in the lower to mid-troposphere after MCSs decays, and several studies have identified MCVs (Harr et al. 1996; Zhang and Bao 1996) and vortex mergers (Simpson et al. 1997; Ritchie and Holland 1997; Kieu and Zhang 2008) as precursors to TCG. As individual MCVs develop within close proximity, they may interact and merge into a larger and stronger MCV, particularly if several small MCVs exist within a larger cyclonic circulation, such as the West

Pacific monsoon trough (Simpson et al. 1997). The phenomenon of vortex mergers is widely believed to play an important role in some TCG cases, and Houze (2004) suggested that MCVs are the building blocks of tropical cyclones (TCs). Recently, Kieu and Zhang (2008) found that the genesis of Tropical Storm Eugene (2005) resulted from the merging of two mesovortices, spawned from MCSs within the Intertropical Convergence Zone (ITCZ). Obviously, the result of merging vortices is the formation of a larger and stronger lower-tropospheric vortex. But for a sustained TCG process to take place, cyclonic circulation must increase near the surface.

Two pathways have been proposed to understand the development of near-surface vorticity *during genesis*, and they are often referred to as top-down (Bister and Emanuel 1997) and bottom-up (Zhang and Bao 1996a,b; Hendricks et al. 2004; Montgomery et al. 2006), in reference to the vertical direction of vorticity growth. However, little work has been done to understand the development and organization of storm-scale circulations *during the pre-genesis stage*, i.e., a slowly-evolving stage prior to TCG. In particular, it remains uncertain whether or not accumulation of cyclonic vorticity or a build-up of cyclonic circulation can occur within a tropical depression (TD) in which scattered deep convection is often widespread (e.g., see Zehr 1992).

It appears that previous studies have focused more on the development of MCSs than the resulting cyclonic vorticity in relation to the TD-scale circulations during pre-genesis. For example, Zipser and Gautier (1978), hereafter ZG78, analyzed the largest MCS during the GARP Atlantic Tropical Experiment (GATE) that occurred within a slowly-intensifying TD. ZG78 found that as the MCS' cloud shield evolved

from circular in shape to more comma-shaped with time, the midlevel circulation center occurred westward of that at the low levels (see Figs. 6 and 7 therein). Despite the large size of the MCS, ZG78 detected no low equivalent potential temperature ($\theta_e$) moist downdrafts. The three-dimensional (3D) structures and evolution of the storm-scale vorticity in their case was unknown due to the lack of high-resolution observations over the tropical ocean.

In Chapter 2 of this dissertation (i.e., Hogsett and Zhang 2010), we presented an 11-day (i.e., 0000 UTC 27 April – 0000 UTC 8 May) cloud-resolving simulation of the genesis of Typhoon Chanchu (2006) that occurred in the near-equatorial West Pacific during the active phase of the Madden-Julian Oscillation (MJO) using the quadruply nested (54/18/6/2 km) version of the Weather Research and Forecast (WRF) model. Results show that a synoptic westerly wind burst (WWB) associated with the MJO accounts for the generation of a westward-tilted vortex with organized cyclonic rotation up to 400 hPa, hereafter the titled WWB-vortex, which gives rise to the development of deep convection at a preferred location (i.e., on the downtilt-right side). Genesis of Chanchu from the WWB-vortex, which forms near the equator almost a week prior to genesis, takes place near 192 h into the model integration, valid at 0000 UTC 5 May 2006 (hereafter 5/00-192), and after a long incubation period of the incipient tilted WWB-vortex. The pre-genesis period is characterized by an increasingly upright vortex as a result of persistent convective overturning on the downtilt-right side of the vortex. Although the simulated genesis begins 2 days prior to that observed, it occurs at nearly the same location as observed along the track.

The objectives of the present study are to (i) examine the 3D structures and evolution of several MCSs and an MCV in relation to the tilted WWB-vortex during the pre-genesis stage; (ii) clarify the impact of convectively generated vortices (CGVs) on the transition of the tilted vortex to TC Chanchu and the roles of the MCSs prior to genesis; and (iii) gain insight into the trigger of TCG as the tilted WWB-vortex is transformed to an upright orientation. The objectives will be achieved using cloud-resolving simulations of the case mostly from the 6-km resolution domain, unless otherwise mentioned.

The next section shows the distribution of larger-scale flows and precipitation with respect to the vertically tilted WWB-vortex prior to and during the genesis stage in order to provide a general framework for the subsequent discussion of tropical transition processes. Section 3.3 describes the 3D structures and evolution of four MCSs in relation to the tilted WWB-vortex as well as their vortical contributions to the system-scale rotation during a two-day period prior to TCG. Section 3.4 presents the transition of the WWB-vortex from a weak baroclinic system to a warm-cored TC and discusses the trigger of TCG. A summary and concluding remarks are given in the final section.

*3.2. An overview of pre-genesis*

Fig. 3.1 provides an overview of the low- and midlevel evolution of the horizontal flows and relative vorticity as well as the simulated radar reflectivity prior to and at the early stage of the genesis of Chanchu. At 3/00-144 (i.e., 48 h prior to genesis; see Figs. 3.1a,e), the vertically tilted WWB-vortex circulations are occurring at scales of more than 1000 km, with the 600-hPa center (denoted as “A” in Fig. 3.1a)

located about 450 km to the west-northwest of the 900-hPa center (denoted as "C" in Fig. 3.1e); this horizontal distance between A and C represents the degree of vertical tilt of the WWB-vortex between 600 and 900 hPa. A south-north-oriented convective rainband, as defined by a large gradient of radar reflectivity, develops to the north of C on the downtilt-right side of the tilted WWB-vortex, which is a favorable location for isentropic lifting of the moist MBL air (Jones 1995), as discussed in detail in Chapter 2. The mid- and upper-level cyclonic flows account for the generation of extensive trailing stratiform clouds to the north and west of the convection (Fig. 3.1e). A cyclonic vorticity ($\zeta^+$) band, denoted by "V," will be shown in section 3.3 as an MCV corresponding to the leading rainband. The associated cyclonic vorticity generated by precipitation processes serves to depress the local flow fields into a deep midlevel trough, with another relatively weaker vorticity center situated in the trailing stratiform region (Fig. 3.1a).

Of importance is that A and V are collocated within a midlevel large cyclonic envelope modulated by the WWB, which is a favorable configuration for merger (Simpson et al. 1997). Indeed, A and V begin to merge by 4/00-168 (Fig. 3.1b). Of interest is that unlike the vortex merger in Kieu and Zhang (2008), the present merging process is confined more to the midlevels and does not cause significant changes in the surface flow fields (see Fig. 3.2a). The resulting vortex AV contracts and exhibits a more circular shape with the peak $\zeta^+$ of greater than $2 \times 10^{-5}$ $s^{-1}$ near the vortex center at 5/00-192 (Fig. 3.1c). Meanwhile, the centers of AV and C become nearly collocated, signifying the genesis of Chanchu with a comma-shaped rainband in its inner-core region.

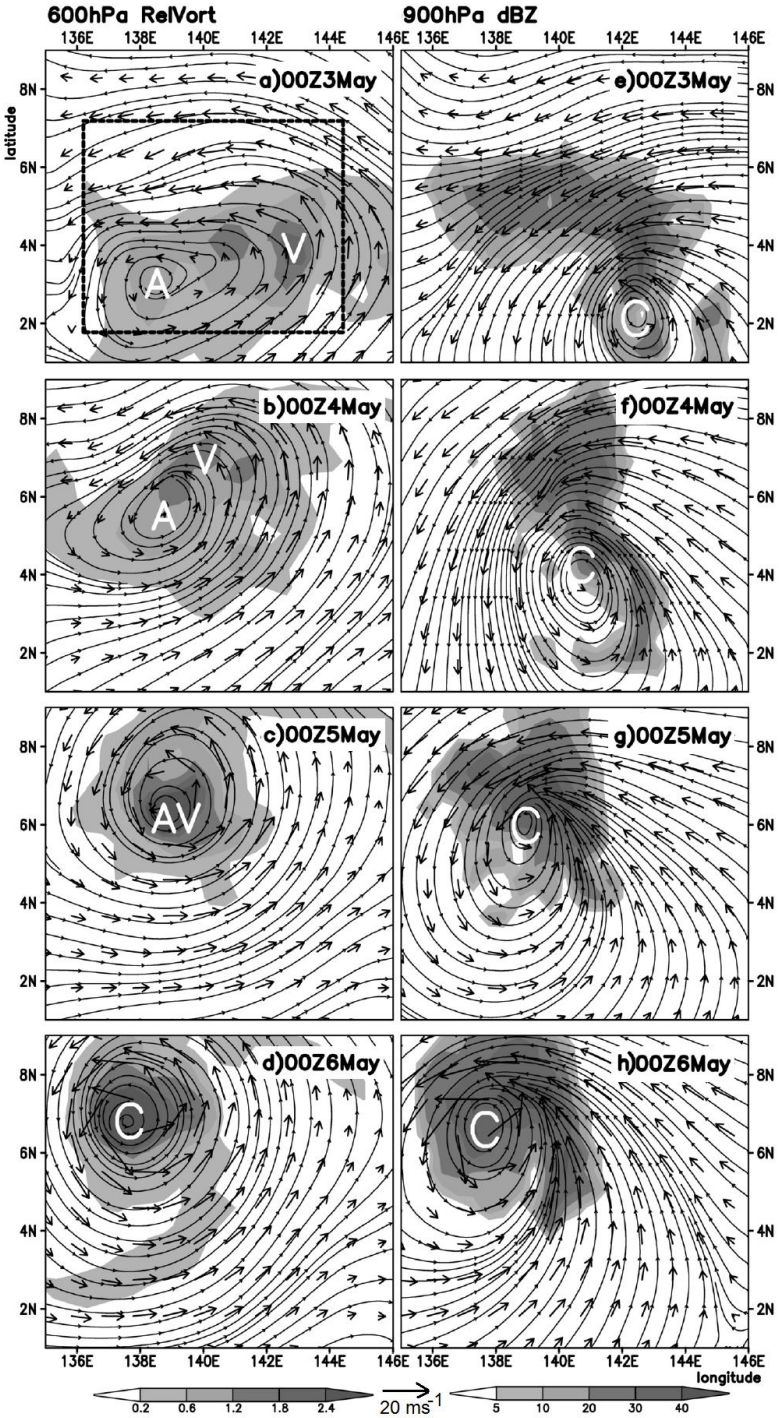


Figure 3.1. Horizontal distribution of (a) – (d) the 600-hPa flow vectors and streamlines as well as the (500-700 hPa) layer-averaged relative vorticity (shaded, $10^{-4}$ $s^{-1}$); and (e) – (h) the 900-hPa flow vectors and streamlines as well as radar reflectivity (shaded, dBZ), given at 24-h intervals, from the 6 – 9 day simulations, valid between 0000 UTC 3 – 0000 UTC 6 May 2006, over the 54-km resolution domain. Letters, "A", "C", "V", and "AV" denote the location of the peak relative vorticity associated with the Pre-Chanchu vortex at 600- and 900-hPa, an MCV, and the merger of A and V, respectively; similarly for the rest of figures. The heavy box in (a) denotes the area of focus for Fig. 3.3.

The time series of the minimum sea-level central pressure ($P_{min}$) at high temporal resolution, given in Fig. 3.2a, shows that the storm intensity fluctuates significantly with roughly a daily cycle, but it does not deepen continuously until 5/00-192. During the pre-genesis period, $P_{min}$ remains above 1000 hPa, which is even higher than the value at the earlier stages, and the maximum surface wind ($V_{max}$) generally remains below 20 m $s^{-1}$. [Note that the magnitudes of $P_{min}$ and $V_{max}$ shown herein are greater than those shown in Chapter 2 due to the use of different (6 vs. 18 km) resolution data.] While the magnitude of $V_{max}$ exceeds the threshold for a TD throughout pre-genesis, the location of $V_{max}$ during 3 – 5 May appears to be closely associated with the distribution of *four MCSs*, hereafter referred to as MCS1-4 (their durations are marked in Fig. 3.2a), that develop to the north of the low-level circulation center C. They are distinct in structure and intensity from a fifth convective structure: a weak, arc-shaped rainband that wraps around the eastern semicircle of C (Figs. 3.1f,g). Of interest is that the life cycles of the four MCSs coincide well with the fluctuation of $P_{min}$, but have little long-lasting impact on the typical metrics of storm intensity, as TCG does not occur until near the end of MCS4. Of particular relevance to the present study is that the *midlevel* cyclonic vorticity ($\bar{\zeta}_{600}$) begins to increase at 3/00-144, and accelerates shortly after 4/00-168, more than doubling in magnitude between 3/00-144 and 5/00-192 (Fig. 3.2b). On the other hand, the *low-level* relative vorticity ($\bar{\zeta}_{900}$) increases by only 20% during the same period. Note that $\bar{\zeta}_{900}$ remains nearly constant since 1/00-96, at which time the first closed surface isobar is formed (see Chapter 2), and commences its slow

amplification after the arc-shaped rainband around C increases its intensity and coverage (cf. Figs. 3.2b and 3.1f). Similarly, only small changes in the mean surface wind speed ($V_{mean}$) and the mean surface heat fluxes (HFX) occur during the pre-genesis stage in spite of continued MCS development (Fig. 3.2a). Note that all the vortex- or storm-scale variables presented herein are calculated by using an area of 400 km × 400 km following the 900-hPa circulation center C, except for $\bar{\zeta}_{600}$ that is calculated following the 600-hPa circulation center A (and AV post-merger). In addition, we define the storm- and system-scale as the above area average centered at C, and the (600 km × 600 km) area average centered between A and C including the rainband to the north, respectively. The different behaviors between the low- and mid-level rotational development and their relation to the four MCSs will be the subjects of the next two sections.

The simulated Chanchu begins to intensify after 5/00-192, as shown by continuous increases in $V_{max}$, $V_{mean}$, HFX, $\bar{\zeta}_{900}$, $\bar{\zeta}_{600}$, and drops in $P_{min}$, when the midlevel vortex AV aligns vertically with the low-level vortex center C (cf. Figs. 3.1c,g and 3.2a,b). Note that TCG in the present case occurs after more than 5 days of intensity fluctuations at the TD stage, during which period the near-surface circulation with $V_{max} > 15$ m $s^{-1}$ is a persistent feature. Apparently, such a long time scale for the onset of TCG is attributable to the vertical tilt of the WWB-vortex, despite the obvious organization of deep convection and increase in the midlevel rotation through the convective enhancement and vortex-merging processes (Figs. 3.1a and 3.2b). Nevertheless, even though the circulation centers become coherent in the vertical at the onset of TCG, the vertical wind shear (VWS) between 900 and 400

hPa in the near-storm environment remains significant (i.e., > 15 m $s^{-1}$, see Fig. 3.2b). It should be mentioned that the 400-900 hPa (rather than the typical 200-900 hPa) layer VWS is utilized herein because this is the layer in which the tilted WWB-vortex is embedded (see Figs. 3.3b and 3.4b).

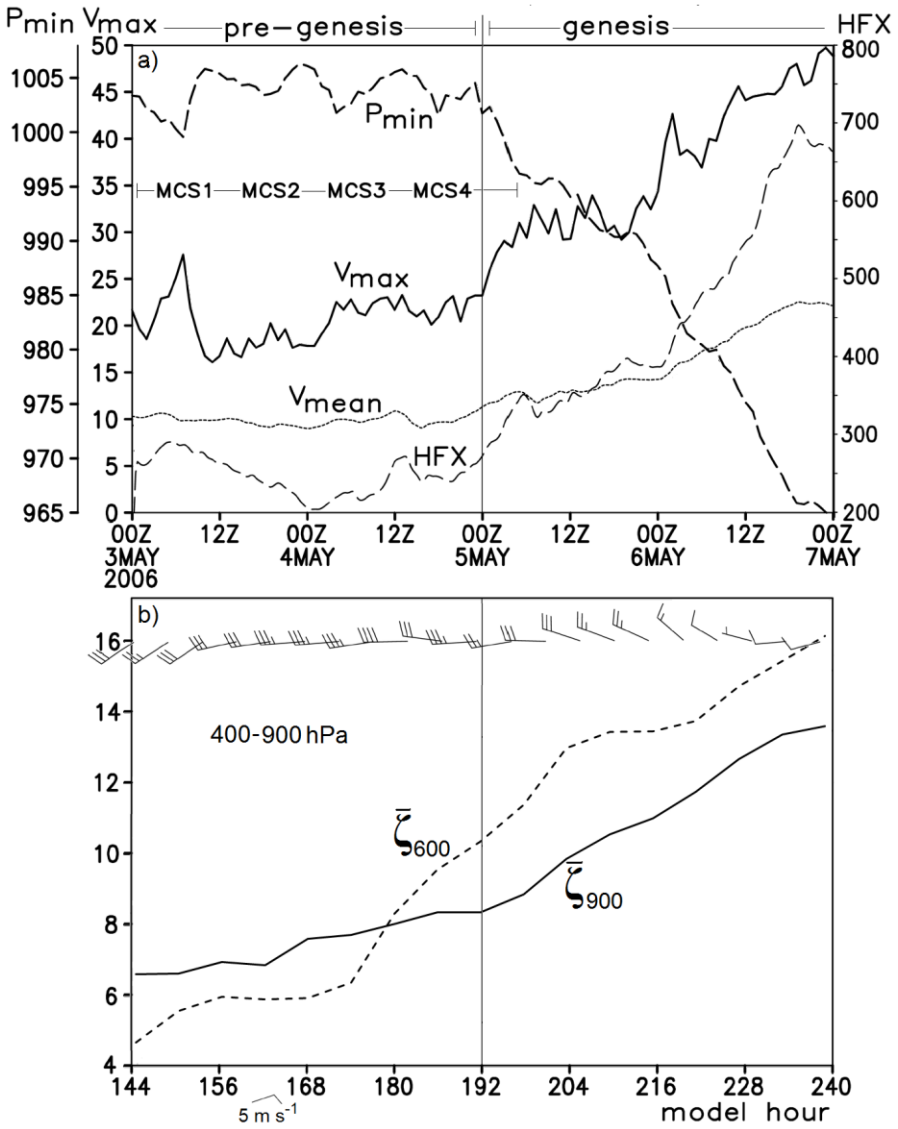


Figure 3.2. (a) Time series (at 60-min intervals) of the minimum central pressure ($P_{min}$, hPa), the maximum surface winds ($V_{max}$, m $s^{-1}$), and the area-averaged (400 km × 400 km) surface latent and sensible heat fluxes (HFX, W $m^{-2}$) and surface wind ($V_{mean}$, m $s^{-1}$) during the 4-day ($\Delta x$ = 6 km) simulation (i.e., 3/00-144 – 7/00-240), which follows the circulation center C; (b) as in (a), but at 6-hr intervals for the area-averaged relative vorticity ($10^{-5}$ $s^{-1}$) centered at A at 600 hPa ($\bar{\zeta}_{600}$) and centered at C at 900 hPa ($\bar{\zeta}_{900}$), and the area-averaged vertical shear (a full barb is 5 m $s^{-1}$) between 400 and 900 hPa centered at C. The thin vertical line at 0000 UTC 5 May demarcates the pre-genesis and genesis periods.

In summary, while the MJO accounts for the formation of the tilted WWB-vortex, as detailed in Chapter 2, it appears to be the CGVs and their merging into the WWB-vortex (e.g., A-V merger) that play some roles in the intensification of the midlevel rotational flows. When the WWB-vortex becomes upright, *TCG commences and continues as long as deep convection could persist in the inner-core regions*. In Chapter 2, we have shown an example of aborted genesis with $V_{max}$ reaching 18 m $s^{-1}$ near 2/00-120, at which time an upright vortex forms as a result of the interaction between CGVs and the WWB-vortex. However, TCG is aborted shortly after deep convection weakens, and subsequently the WWB-vortex becomes westward-tilted again. Thus, our discussion of pre-genesis that follows will involve mesoscale events after the aborted genesis, i.e., beginning from 3/00-144.

### *3.3. Development of four MCSs and their vortical contributions*

In this section, we focus on the important roles of the four MCSs, as well as the arc-shaped rainband, in achieving the transition from a tilted to an upright vortex leading to TCG. Their general precipitation structures and the formation of the above-mentioned MCV will also be examined.

#### *3.3.1. Mesoscale flow structures at an early pre-genesis stage*

At 3/00-144, the near-surface disturbance exhibits a closed circulation with $P_{min}$ ~ 1004 hPa near 3ºN (Fig. 3.3d). An elongated, north-south-oriented flow (and moisture) convergence line, as indicated by intersecting streamlines, appears in the MBL to the north of C (i.e., on the downtilt right side), which is associated with a tropical squall line MCS1, which corresponds to the above-mentioned leading

rainband with strong radar reflectivity (cf. Figs. 3.3c,d and 3.1e). This MCS is still at its early development stage at this time. To the west of the leading convective line is an extensive area of trailing stratiform precipitation due to the presence of the pronounced easterly flows in the mid- to upper- levels (Figs. 3.3a-c).

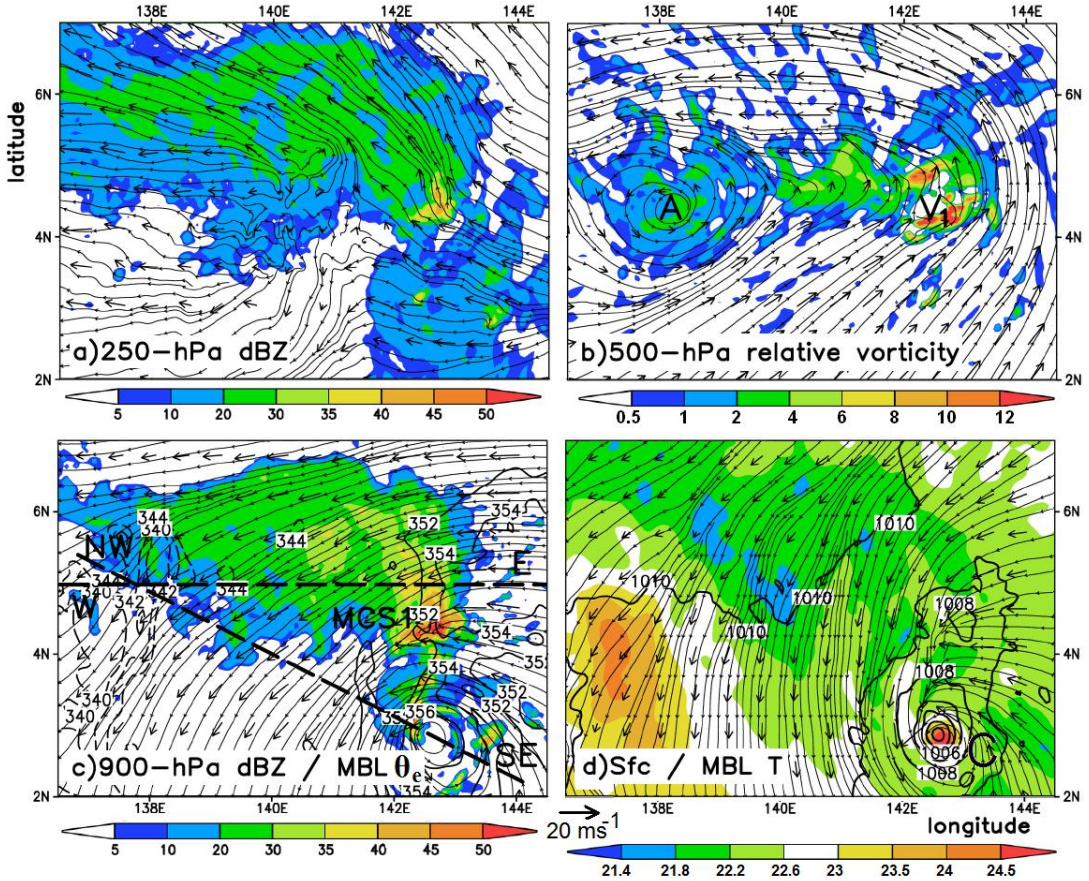


Figure 3.3. Horizontal distribution of (a) the 250-hPa radar reflectivity (shaded, dBZ); (b) the 500-hPa relative vorticity (shaded, $10^{-4}$ $s^{-1}$); (c) the 900-hPa radar reflectivity (shaded, dBZ) and the surface – 900 hPa layer-averaged equivalent potential temperature (contoured at 340, 342, 344, 352, 354, and 356 K); and (d) the surface – 900 hPa layer-averaged temperature (shaded, °C) and the sea-level pressure (contoured at 1-hPa intervals), superimposed with the horizontal flow vectors and streamlines at the individual levels, that are taken at 3/00-144 from the 6-km resolution domain. Symbol "$V_1$" in (b), denotes a convectively-generated vorticity center (see text). The heavy dashed lines W – E and NW – SE in (c) denote the location of the vertical cross sections used in Fig. 3.4.

A west-east vertical cross section, taken through MCS1 (Fig. 3.4a), shows a vertical mesoscale flow pattern that is similar to that shown by Gamache and Houze

(1982) for a typical tropical squall line, including the lifting of high-$\theta_e$ air in the MBL easterly flow, strong ascent in the leading convective line, weak ascent (descent) above (below) the melting level in the trailing stratiform region, and a deep layer of front-to-rear (FTR) moist inflows. This flow pattern acts to continually generate precipitation particles to maintain the large stratiform region, covering an area of nearly 80000 $km^2$ (Fig. 3.3c), which is about twice of the maximum size documented by Yuter and Houze (1998) in a study of WNP MCSs.

It is evident from Figs. 3.3b and 3.4b that MCS1 produces a (upright) deep layer of significant cyclonic vorticity (e.g., $\zeta^+ \sim 12 \times 10^{-4}$ $s^{-1}$ at 500 hPa) along the leading line and weaker vorticity (e.g., $\zeta^+ \sim 2 \times 10^{-4}$ $s^{-1}$ at 500 hPa) in the stratiform region, which are superimposed with a *broad but shallow* cyclonic circulation ($\zeta^+ \sim 0.5 \times 10^{-4}$ $s^{-1}$) associated with the WWB-vortex tilting northwestward from its surface location C to the back edge of the stratiform region at 400 hPa. The deep tilted vortex is only roughly 150 - 200 hPa deep, as defined by $\zeta^+ \sim 0.5 \times 10^{-4}$ $s^{-1}$ (Fig. 3.4b), with little cyclonic vorticity above or below the layer, e.g., below 600 hPa (Fig. 3.3c) or above 500 hPa (Fig. 3.3a).

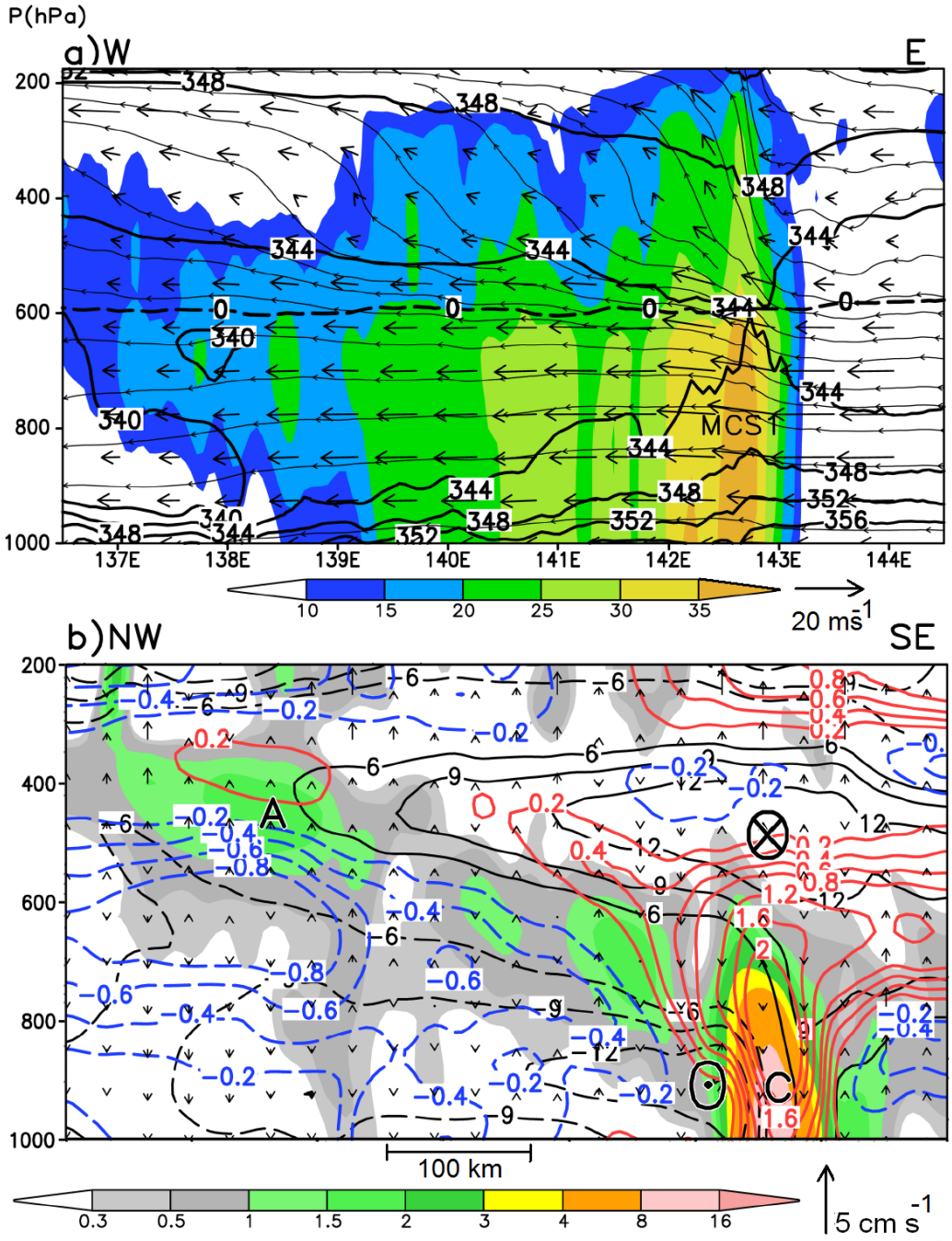


Figure 3.4. (a) West-east vertical cross section of radar reflectivity (shaded, dBZ), equivalent potential temperature (at intervals of 4 K), superimposed with the melting level (heavy dashed line) and in-plane flow vectors and streamlines (vertical motion multiplied by a factor of 10). (b) Northwest-southeast vertical cross section of the relative vorticity (shaded, $10^{-4}$ $s^{-1}$), the cross-plane wind speed (contoured, ± 6, 9, 12, and 15 m $s^{-1}$) into (out of) the vertical plane with their maximum magnitude marked by a cross (dot) symbol, superimposed with deviation temperatures (heavy contours, ± 0.2, 0.4, 0.6, 0.8, 1.2, 1.6 and 2.0 °C) and vertical motion vectors. They are taken at 3/00-144 along lines given in Fig. 3.3c. Note that all the fields have been averaged laterally within 54 km in (a) and during a 3-h period in (b) in order to capture representative structures of (a) MCS1 and (b) the tilted WWB-vortex, respectively.

Of importance is that the tilted WWB-vortex has a cold-cored[1] baroclinic structure with large VWS and a weak warm layer above A, as compared to the warm-cored low-level circulation C with nearly upright isotaches in the lowest 300-hPa (Fig. 3.4b). Because of the tilted circulations, horizontal flows change direction with height, with large (directional) VWS across the vortex layer. (Stronger VWS occurs along the WWB axis, which is about 450 km to the south of the vortex core, as shown in Fig. 2.5a in Chapter 2.) One may note that the vertical cross-plane flow structures, i.e., the near-northerly flow below and a near-southerly flow above the vortex layer, resemble those associated with a midlatitude cold front, with the vortex layer corresponding to the "frontal zone". A thermal gradient of 2.8°C (300 km)$^{-1}$ between the cold and warm cores corresponds qualitatively well with the large VWS in the vortex layer. This thermal gradient is weaker than that in cold-cored systems that developed into TCs at higher latitudes (e.g., Bracken and Bosart 2000; Davis and Bosart 2003).

It should be pointed out that because of the shallowness, the closed cyclonic circulations associated with the tilted WWB-vortex at individual levels are not always aligned in one vertical cross section between the lower- and mid-level centers (i.e., A and C). So the horizontal flow fields at different levels aloft are sometimes used herein to help gain insight into the 3D structures and evolution of the pre-Chanchu disturbance.

[1] The thermal anomalies are denoted herein by deviation temperatures that are obtained by subtracting the slice-mean at individual levels in the cross section.

Note that the tilted vortex core (or its peak cyclonic vorticity) at 3/00-144 is mostly distributed along the southern edge of the cloud/precipitation regions at each level, except near the western edge (cf. Figs. 3.3a,c and 3.4b), confirming again the favorable location of the northern semicircle (i.e., downtilt-right) for convective development. In particular, the northern semicircle provides both the necessary background vorticity for vortex stretching near the equator, as well as isentropic ascent to trigger convection. In fact, the cyclonic vorticity along the leading line of MCS1 is much stronger than that associated with the WWB-vortex, and it induces a deep trough that is superimposed with the broad closed circulation in the midtroposphere (Fig. 3.3b). Twenty hours later, this trough becomes a closed MCV at 600 hPa (see Figs. 3.5a-f). As will be seen in the next section, the midlevel vortex-vortex interaction plays an important role in aligning the closed cyclonic circulations in the vertical because of the intense cyclonic vorticity generated within the leading convective line.

It should be mentioned that the horizontal flow structures shown in Fig. 3.3 appear similar to the intensifying TD analyzed by ZG78 in which an MCS developed in the northern semicircle and the midlevel circulation center was not only located westward of the low-level center, but also exhibited a trough that extended northeastward from the center toward the region of active convection. Data limitations prevented ZG78 from ascertaining the complete 3D structures (i.e., any tilt that may have existed) of the developing TD. Our results show clearly how the tilted vortex exhibits coherency from the surface to 400 hPa (cf. Figs. 3.3b,c and 3.4b). As

shown in Chapter 2, the coherent vertical tilt first develops prior to April 30 when closed circulations form in the lower half of the troposphere.

While the WWB-vortex core remains mostly free of precipitation, its northwestern one-third portion is situated above the stratiform region, where some stratiform clouds/precipitation appear as a result of the advection by the northerly flow beneath the vortex layer (Fig. 3.4b). As precipitation falls through the low-$\theta_e$ layer below (Fig. 3.4a), evaporatively- (and melting-) driven moist downdrafts occur at the trailing stratiform region, more significantly in the region between A and MCS1 (see Fig. 3.3d). The downdrafts account for the generation of the lowest-$\theta_e$ air at 900 hPa, with a $\theta_e$ value (i.e., 340 K) similar to that in the 600-800 hPa layer, and a west-east $\theta_e$ gradient in the lower troposphere (cf. Figs. 3.3c and 3.4a). Because the precipitation available for evaporation in the downdrafts diminishes below 800 hPa, the *cyclonically* forced descent tends to occur more dry adiabatically, leading to the local warming near the surface to the south of A (Fig. 3.3d). As will be seen later, the development of moist downdrafts and the associated thermodynamic properties help understand the life cycle of each MCS under study.

In the next subsections, we focus more on the structures and evolution of MCS1 – MCS4, as well as their implications to TCG. For this purpose, we have superimposed in Fig. 3.5 the simulated radar reflectivity with streamlines at 600 and 900 hPa at 4-h intervals to show how deep convection evolves with respect to the tilted WWB-vortex and what impact each MCS produces on the vortex. Although the precipitation structure shown in Fig. 3.5 indicates that the transition between the four MCSs is a continuous process, we discretize the evolution herein in accordance with

the convective morphology and mesovortex mode along the leading line and their influences on the time series of $P_{min}$ (see Fig. 3.2a).

*3.3.2. Life cycle of MCS1: Squall line*

It is evident from Figs. 3.5a-d that the typical tropical squall line structures associated with MCS1 change significantly during the period of 3/00-144 – 3/12-156. Specifically, the extraordinarily large stratiform region, as shown in Fig. 3.3, shrinks with time as the midlevel elliptic circulation switches from its west-east to southwest-northeast orientation with a growing area of flows in opposite directions to those in the layers below. It almost dissipates by 3/12-156 when the 900- and 600-hPa flows behind the leading line become opposite in direction (Fig. 3.5d). Meanwhile, a bow-shaped convective segment appears in the northern leading line, similar to that commonly observed in midlatitude squall lines in the presence of the rear-to-front (RTF) flows (e.g., Houze et al. 1989; Zhang et al. 1989), while the southern convective segment is displaced to the west semicircle of the low-level circulation. As a result, the leading convective line shifts from its north-south orientation to northeast-southwest (cf. Figs. 3.5a and 3.5d).

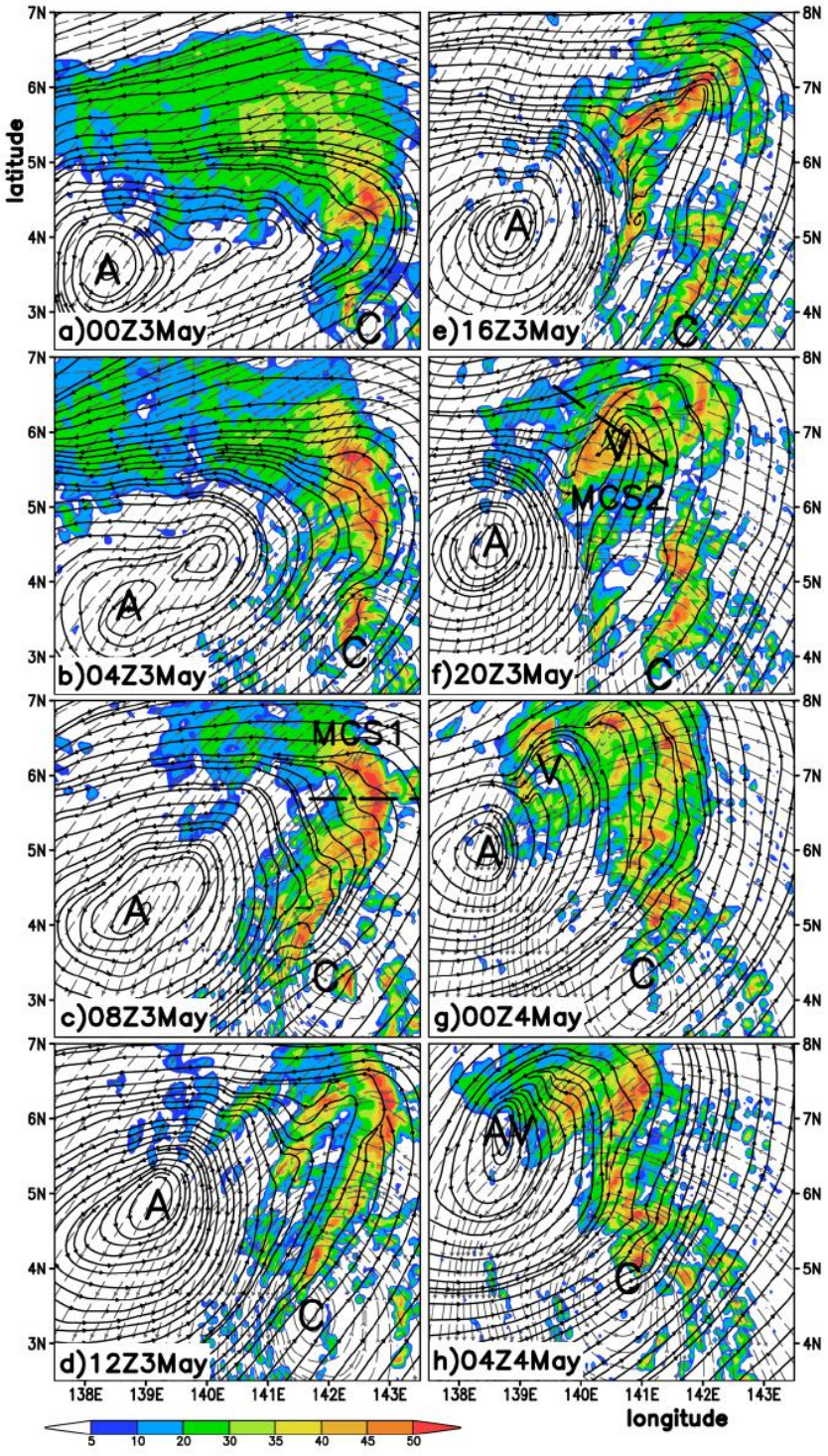
a)00Z3May
b)04Z3May
c)08Z3May
d)12Z3May
e)16Z3May
f)20Z3May
g)00Z4May
h)04Z4May
MCS1
MCS2
A
C
V
latitude
longitude
7N
6N
5N
4N
3N
8N
138E
139E
140E
141E
142E
143E
5
10
20
30
35
40
45
50

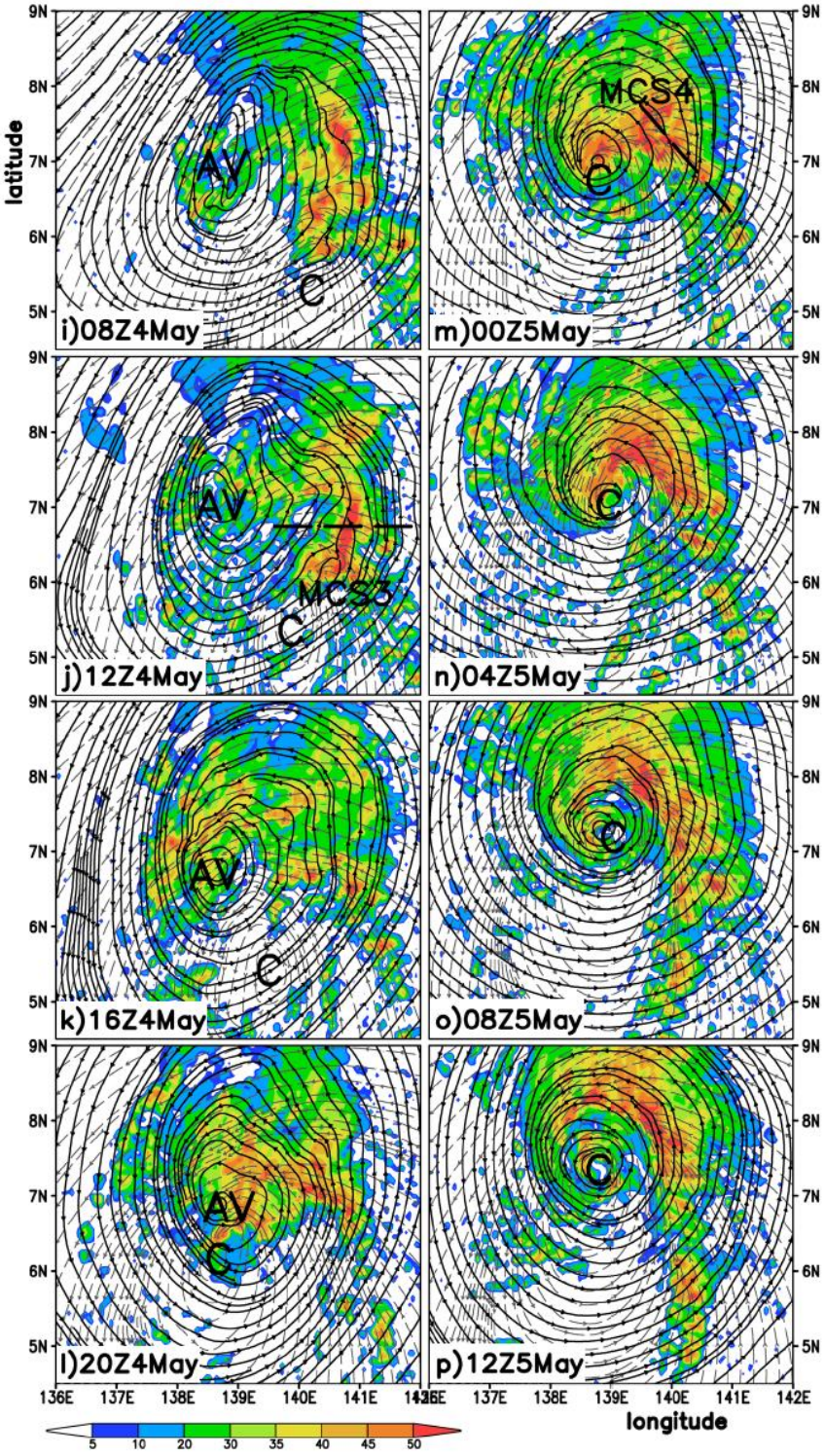


Figure 3.5. The evolution of the 900-hPa radar reflectivity (shaded, dBZ) at 4-h intervals between (a) 3/00-144, and (p) 5/12-204 from the 6-km resolution domain, superimposed with the 600-hPa (heavy solid) and 900-hPa (light dashed) streamlines. The path of vertical cross sections (heavy dashed) during the mature stage of MCS1 in (c), MCS2 in (f), MCS3 in (j), and MCS4 in (m) are denoted.

Although no RTF flow is evident in the present case due to the presence of deep FTR flows, the increasing streamline curvature at the northern end of the squall line suggests the formation of an MCV that may weaken or alter the FTR flows. By 3/12-156 (Fig. 3.5d), a southwest-northeast oriented inverted trough develops behind the leading line and becomes almost a separate MCV entity at 3/20-164 (see V in Fig. 3.5f). As shown in Zhang (1992), the northern segment of a squall line favors the generation of an MCV due to the tilting of horizontal vorticity associated with the local large VWS, the so-called bookend vortex by Weisman and Davis (1998). MCVs, such as V, are a typical mesoscale phenomenon near the end of the life cycle of midlatitude MCSs (Zhang and Fritch 1988; Menard and Fritsch 1989; Bartels and Maddox 1991), but few studies have previously examined the MCS/MCV system near the equator where the Coriolis force nearly vanishes. The increasing streamline curvature associated with the MCV tends to help shrink the stratiform region by reducing the midlevel FTR flows behind the leading convective line. In addition, the hook-shaped flow pattern allows the wrap-around of deep convection along the leading line and the generation of moist downdrafts to the rear portion of the MCV as the northeasterly moist air is lifted above the low-level cold pool in this downtilt-right side of the tilted vortex (see Figs. 3.5d and 3.7a).

A vertical (normal-line) cross section through the central portion of the bow-shaped convective line, given in Fig. 3.6a, shows a deep FTR inflow layer that decreases in magnitude up to 600 hPa, where the low-level easterly flows veer to the along-line direction with little normal-line flows above. Strong upward motion occurs in the leading line with the most intense cyclonic vorticity in the midlevel, which is

consistent with the subsequent generation of an MCV (cf. Figs. 3.6a and 3.5a-f). Although the MCV is about 350 km northeast of the mid- and low-level circulation centers at 3/12-156, together with the cyclonic vorticity along the leading line it represents the vortical contribution of MCS1 to the midlevel storm-scale rotation (Fig. 3.2b), especially when all mesovortices of different sizes are congregated. Clearly, only deep convection at the southern end of the squall line could possibly affect the intensity of the surface $P_{min}$ (i.e., associated with C), but it is not effective as it radiates outward in a linear mode rather than wraps around as a spiral band. As shown in Chapter 2, the southern semicircle of the tilted WWB-vortex is distributed with descending motion and lower-$\theta_e$ air (also see Fig. 3.4a). In addition, large local VWS over C's core region, specifically a 600-hPa jet of > 12 m $s^{-1}$, tends to suppress convective development there (see Fig. 3.4b).

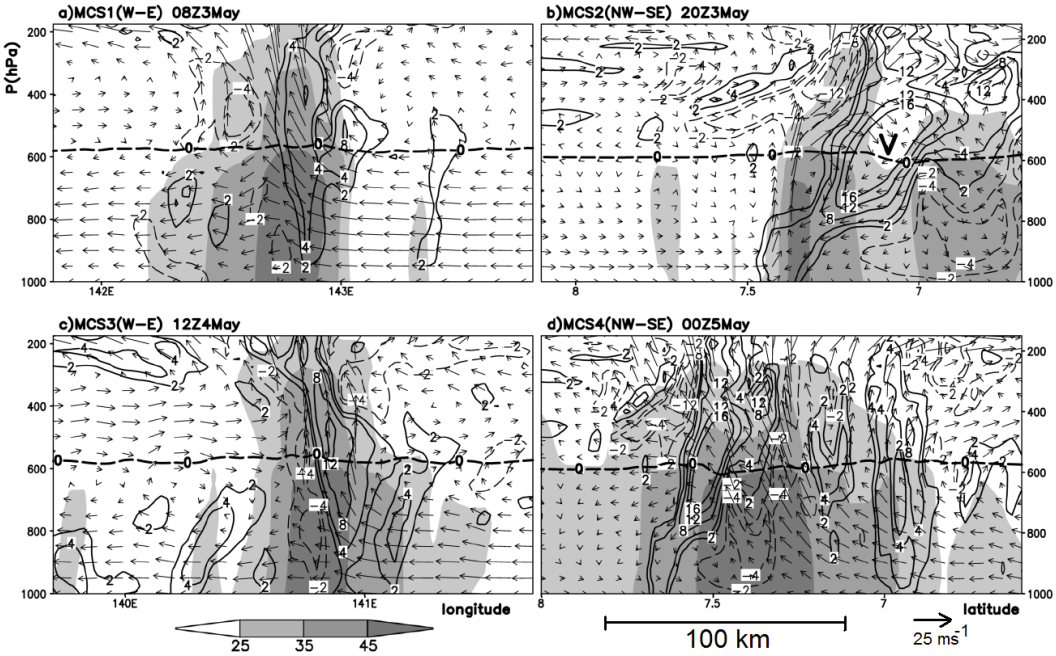


Figure 3.6. Vertical cross sections of the radar reflectivity (shaded, dBZ), and relative vorticity (contoured at ± 2, 4, 8, 12, and 16 × $10^{-4}$ $s^{-1}$), superimposed with in-plane flow vectors, associated with (a) MCS1; (b) MCS2; (c) MCS3; and (d) MCS4, that are taken nearly along the low-level flows given in Figs. 3.5c, 3.5f, 3.5j, and 5m, respectively. Vertical

motion for the in-plane vectors is enhanced by a factor of 10, and the heavy dashed lines denote the melting level.

Fig. 3.6a also shows that at the early stage of the MCV, weak RTF flow does occur in the 600 – 400 hPa layer, but with little descending motion and it does not penetrate to the leading line as that described in a typical squall system (Houze et al. 1989). This helps explain why the leading line exhibits little eastward movement (Figs. 3.5a-d). The RTF flow becomes more pronounced as the MCV enters its mature stage (see Figs. 3.5f and 3.6b).

*3.3.3. Development of MCS2: Two unique convective episodes*

In general, the midlevel streamlines exhibit diffluence within the leading convective line, and confluence ahead and behind it (cf. Figs. 3.5a-d). But at 3/12-156, we can see midlevel convergence occurring at the back edge of the hook-shaped rainband where the RTF and FTR flows meet (Fig. 3.5d). This tends to cause the development of descending motion along the flow interface (e.g., see Houze et al. 1989), and moist downdrafts below (see Figs. 3.7a,b), leading to the subsequent suppression of deep convection along the leading line (cf. Figs. 3.5d and 3.5e). The dissipation of MCS1 leaves behind the well-developed MCV (i.e., V in Fig. 3.5f), which at its mature stage has a diameter of about 50 km and a depth of 400 hPa (Fig. 3.6b). This MCV is likely generated via tilting of horizontal vorticity and intensified through vortex stretching associated with the midlevel convergence (and descent) of two FTR flows with respect to the "hook-shaped" rainband. The FTR flow at the back edge occurs due to the triggering of deep convection at the westward-advancing outflow boundaries (cf. Figs. 3.5d-g and 3.7b). As this "back-edge" convective segment moves westward, the hook-shaped rainband expands in coverage. However,

it loses convective signature by 4/04-172, as V merges with A (see AV in Fig. 3.5h), especially after new convection develops along the previously dissipated convective line on the east following a few hours recovery period of the conditionally unstable MBL (cf. Figs. 3.5e-g), although this period is much shorter than that discussed by Raymond (1995).

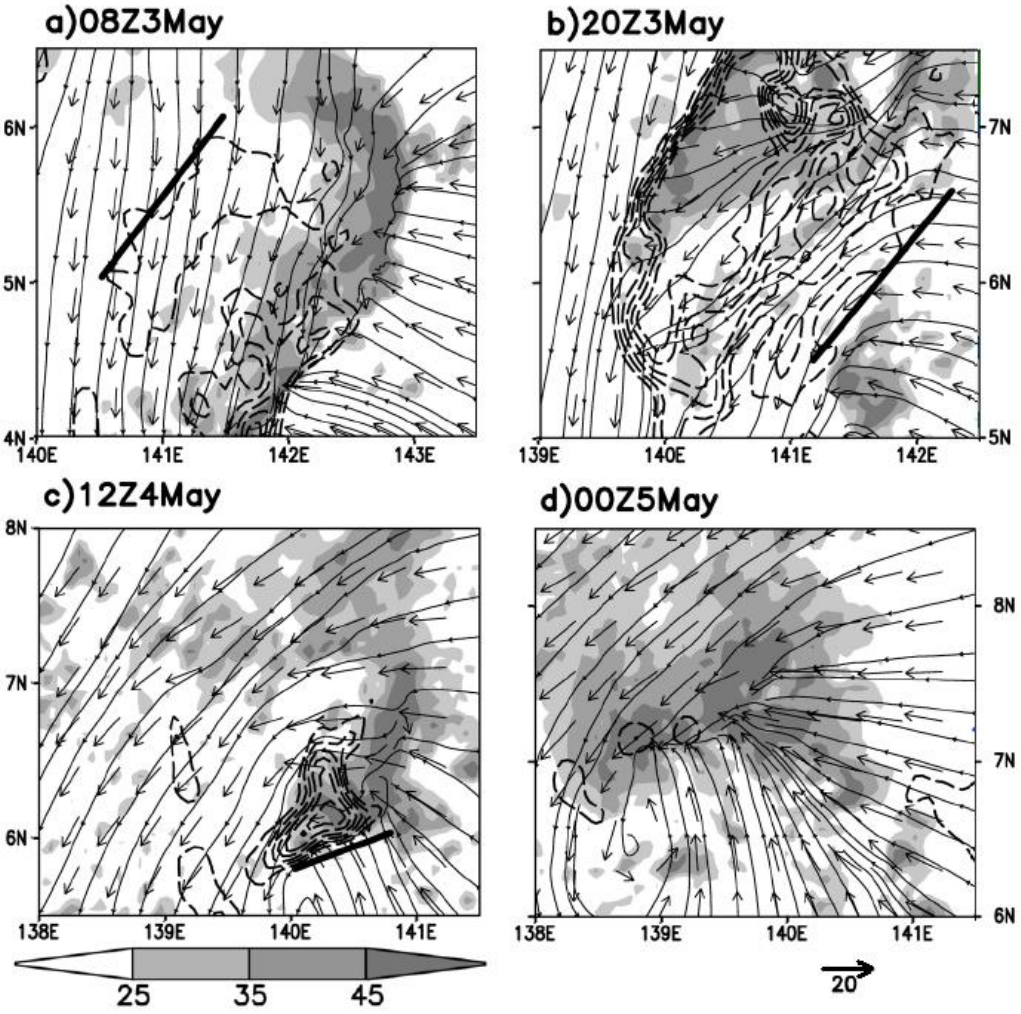


Figure 3.7. Distribution of the horizontal flow vectors, streamlines, and radar reflectivity (shaded, dBZ) at 900 hPa, superimposed with the 950-hPa temperature (dashed at intervals of 0.2°C between 22 and 23°C) showing the cold pool associated with (a) MCS1 at 3/08-152; (b) MCS2 at 3/20-164; (c) MCS3 at 4/12-180; and (d) MCS4 at 5/00-192. Heavy solid lines in (a) – (c) denote the edge of the cold pool where the subsequent MCS develops.

Note that unlike the conceptual model of Houze et al. (1989), this MCV does not accompany significant stratiform clouds because of the above-mentioned outward convective expansion in a moist tropical environment. Of interest is that the shallow midlevel circulation A translates nearly 200 km northward during the 12-h period (cf. Figs. 3.5e-h) due to the presence of the midlevel convergence associated with the westward-propagating MCV. This vortex-vortex interaction appears to account for the intensification of the midlevel cyclonic vorticity that accelerates after 4/06-174 prior to genesis, i.e., after the merger of AV (cf. Figs. 3.2b and 3.5h). In this regard, we may consider the midlevel merging of mesovortices with the tilted vortex as the temporal "storage" of cyclonic vorticity for the subsequent TCG after the cyclonic circulations at all levels become vertically coherent.

It is evident from Figs. 3.5e-h that MCS2 consists of two convective segments: the "back-edge" convective line and the rejuvenated convection to the northeast (Figs. 3.5e,f) and east of V (Fig. 3.5g). As a whole, MCS2 looks like a question-mark-shaped rainband as A and V begin to merge (Figs, 3.5g). Meanwhile, the weak arc-shaped rainband associated with the low-level circulation C becomes more significant with time (cf. Figs. 3.5f-h). Of interest is that MCS2 and the arc-shaped rainband are distributed closely along the mid- and lower-level streamlines (Figs. 3.5b-j), respectively, and both develop in the low-level cyclonic inflows where uplifting is favored. As mentioned earlier, MCS1-3 are more associated with the tilted-vortex dynamics, i.e., on the downtilt-right (Jones 2003), whereas the forced MBL convergence accounts for the generation of the arc-shaped rainband, which occurs intermittently even during the earlier stages of pre-genesis (e.g., see Fig. 3.5a).

However, the latter always remains weak and shallow due to the suppression by large local VWS and the presence of lower-$\theta_e$ air in the western semicircle. Nonetheless, the arc-shaped rainband appears to account for the slow evolution of the lower-level warm-cored circulation and the amplification of $\bar{\zeta}_{900}$ after 4/00-168 (cf. Figs. 3.2b and 3.4b), as will be further shown in section 3.4. Apparently, the present clouds/precipitation asymmetries differ substantially from those shown in other TCG cases (e.g., Kieu and Zhang 2009; Braun et al. 2010) because of the tilted WWB-vortex.

*3.3.4. MCS3: Transition to a spiral rainband*

After the merger of V and A (i.e., as AV) in the midtroposphere, another cycle of convective development (MCS3), following closely that associated with MCS1, takes place on the downtilt-right side of the tilted WWB-vortex. This convective cycle includes the generation of a squall line, a trailing stratiform region in the northern semicircle of AV (Fig. 3.5i), albeit much less extensive than that of MCS1 due to the smaller spatial extent of FTR flows (cf. Figs. 3.5i and 3.5a), and a bow-shaped convective segment with significant midlevel confluence/convergence (Fig. 3.5j). Associated with the bow-shaped convective region is the development of an RTF flow at the central portion and an FTR ascending flow with intense cyclonic vorticity along the leading line, which resemble to a certain degree those associated with MCS1 (cf. Figs. 3.6a and 3.6c). The magnitude of midlevel cyclonic vorticity along the leading line of MCS3 is significantly greater than that in MCS1, as indicated by the increased streamline curvature, due to the absorption of CGVs (see Fig. 3.2b).

However, even though the RTF flow at 4/12-180 is more extensive than that of MCS1 at 3/08-152, only a trough appears to the east of AV (Fig. 3.5j). Apparently, a well-developed MCV fails to develop in MCS3 because of the reduced vertical tilt of the WWB-vortex. That is, the horizontal distance between the midlevel and 900-hPa vortex centers (i.e., A and C) has decreased from about 450 km at 3/00-144 to 200 km by 4/16-184. As a result, the arc-shaped rainband northeast of C is displaced northward to intersect with the southern part of the squall line (cf. Figs. 3.5i and 3.5j), quickly eliminating the bow-shaped portion of the leading line (cf. Figs. 3.5j and 3.5k). As the vertical tilt of the WWB-vortex centers is further reduced, the remnants of MCS3 merge with the arc-shaped rainband to form a comma-shaped rainband with stratiform clouds in the outer region (Fig. 3.5l). Convective cells are thus more distributed along the lower-level inflows in close proximity (i.e., less than 100 km) to the vortex centers (Figs. 3.5k,l). In fact, some convective precipitation appears at the midlevel vortex (AV) center, although it is initiated to the north and away from the low-level center C. It is well known that latent heat release close to the vortex center is very effective in deepening the surface cyclone (Hack and Schubert 1988), and presumably in intensifying the midlevel circulation as well. The genesis of Chanchu takes place shortly after the vortex circulations become vertically coherent (Figs. 3.5l,m).

*3.3.5. MCS4: Formation of a spiral rainband*

While TCG begins at 5/00-192 after the WWB-vortex becomes upright as a result of more than 5-days of continuous convective development, its larger-scale rotational flows still remain highly asymmetric, especially in the lower troposphere

(Figs. 3.5m and 3.7d). For example, the 900-hPa circulation remains meridionally elongated with convectively distorted flow to the north of C (see Figs. 3.7d and 3.5p), whereas the midlevel circulation AV becomes increasingly symmetric with time due to the continued absorption of CGVs (see Figs. 3.1 and 3.5). Moreover, the low-level confluent inflows into (diffluent outflow from) the rainbands are highly convergent (divergent), leading to the formation of a well-developed spiral rainband, defined as MCS4, roughly along the low-level streamlines (Figs. 3.5n-p). Axisymmetrization appears in the midlevel, as revealed by more stratiform clouds in the western semicircle, but not in the lower-level diffluent regions where few convective cells could be triggered. Convective precipitation associated with MCS4, i.e., the incipient primary rainband of Chanchu, is best described at this stage as occurring on the downshear left (Frank and Ritchie 1999; Black et al. 2002), i.e., to the north of the west-southwesterly VWS vector (Fig. 3.2b).

Unlike MCS1 – MCS3, MCS4 does not exhibit significant moist downdrafts (cf. Figs. 3.7a-d), which is attributable to the continued moistening of atmospheric columns in the inner-core region. A vertical cross section along the spiral rainband in the inner-core region (Fig. 3.6d) shows prevailing cyclonically slantwise upward motion that is peaked at the midlevel as a result of the convective mixing of moist entropy, and the convectively generated cyclonic vorticity in the inner core region of MCS4, just like those typically seen in the eyewall of a hurricane (Liu et al. 1997). In this sense, MCS4 is quite unique compared to MCS1 – MCS3. In fact, the four MCSs have different characteristics in terms of orientation and shape, generation of MCVs and moist downdrafts, and dynamical lifting mechanisms (e.g., downtilt-right vs.

downshear-left, and cold pool). Although more case studies are needed, the different MCSs may be typical of the convective evolution leading to TCG from a large-scale tilted vortex.

*3.3.6. Convective contribution to the system-scale cyclonic vorticity*

To help reveal the net contribution of the MCSs, let us first take a look at the tilted WWB-vortex structures prior to 3/00-144 from a dry simulation (hereafter DRY), in which diabatic heating is turned off while holding all the other parameters identical to the control run (hereafter, CTL) presented in Chapter 2. Without the diabatic heating, the WWB-vortex exhibits a more axisymmetric shape but much less vertical tilt than those in CTL (cf. Figs. 3.8a,b and 3.3b,c). In addition, the circulation size in DRY is relatively larger at 900 hPa but much smaller at 500 hPa due to the lack of diabatically aided spin-up and midlevel CGVs, respectively. This explains about 5-hPa central pressure difference after the 144-h integration between the two runs (i.e., 1003 hPa in CTL vs. 1008.5 hPa in DRY). The WWB becomes shallower and less extensive in the absence of diabatic heating, as indicated by the easterly flow to the southeast of A (Fig. 3.8a). In particular, deep convection in CTL distorts substantially the vortex circulations to the north, especially by generating an intense midlevel trough, accounting for the vortex's general northward displacement (see the location of $A_{dry}$ near the equator in Fig. 3.8a versus A near 4°N in Fig. 3.3b).

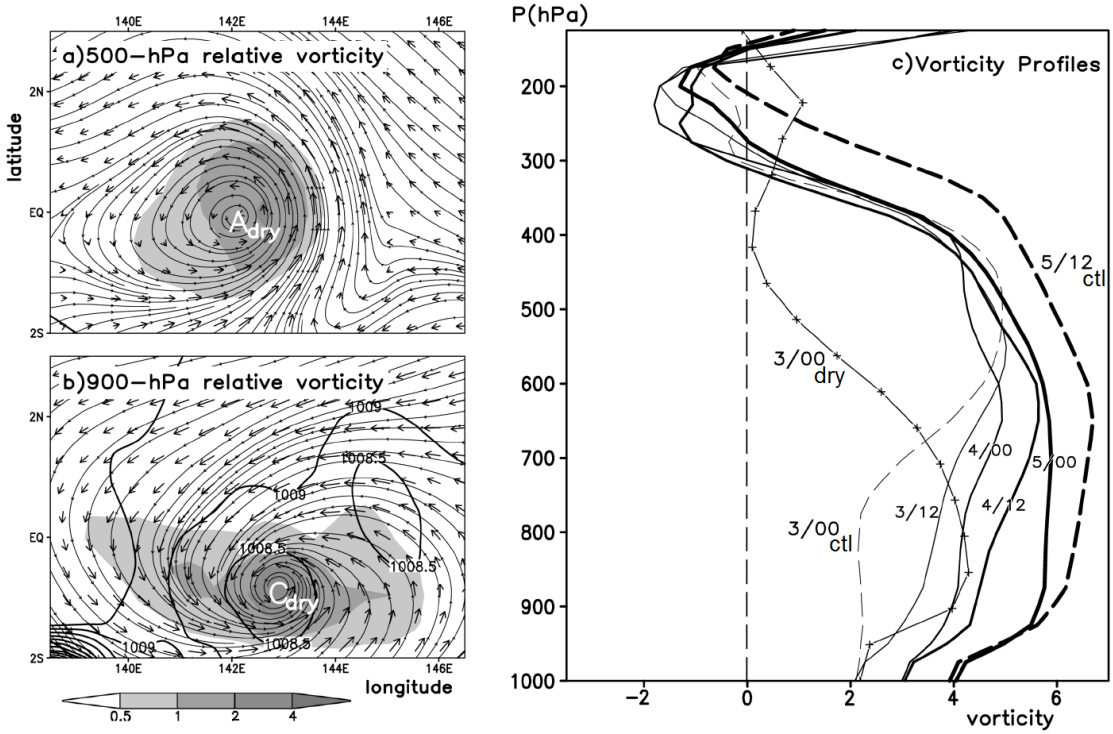


Figure 3.8. Horizontal map of the relative vorticity (shaded, $10^{-4}$ $s^{-1}$), streamlines and flow vectors at (a) 500 hPa, and (b) 900 hPa from the 144-h dry run with the same size but a different area from that for Figs. 3.3b,c. Solid lines in (b) denote the sea-level pressure field. (c) Vertical profiles of the system-scale relative vorticity (x $10^{-5}$ $s^{-1}$) at 12-h intervals between 3/00-144 and 5/12-204. The 3/00 profile from the 144-h dry run is also given.

Fig. 3.8c summarizes the vortical contributions of the four MCSs to the *system-scale* rotation at 12 h intervals. The mean vorticity profile in DRY at 3/00-144 is peaked near 850 hPa where the WWB is maximized, whereas the CTL profile is peaked near 500 hPa where the vorticity generation in the stratiform region is most pronounced (e.g., Figs. 3.6a-d). A comparison of the two profiles indicates that the diabatic heating, prior to 3/00-144, acts to enhance (suppress) midlevel (low-level) cyclonic vorticity at the system scale, and increase the depth of the WWB-vortex circulation. Note though that while the low-level system-scale vorticity in CTL is weaker than that in DRY due to the cold downdraft effects, the local circulation of C and its minimum central pressure are still much stronger. As the stratiform clouds

decay after 3/00-144, the local peak vorticity near 500 hPa decreases slightly. However, continued convective development can account for the amplification of the system-scale cyclonic vorticity, which grows most rapidly between 900 and 600 hPa. The relatively small growth of the system-scale vorticity in the lowest 100-hPa layer, even after 5/00-192, could be attributed to the downward decreased vortex circulation size, in addition to the MBL frictional effects. Although we reserve a detailed investigation of the vorticity generation mechanisms for Chapter 4 of this series of papers, it is sufficient to state from Fig. 3.8 that the contribution of the MCSs to the WWB-vortex system is a net increase of cyclonic vorticity in a deep layer of the troposphere.

### *3.4. Thermodynamic transition*

We have shown above the transformation of the tilted WWB-vortex to an upright one leading to TCG at 5/00-192. Davis and Bosart (2004) referred to the thermodynamic transformation of such a baroclinic disturbance to a warm-cored TC as tropical transition, in contrast with extratropical transition from a TC to an extratropical disturbance. Clearly, it is mostly the CGVs of different scales that are responsible for such a tropical transition, based on the results presented above. However, it remains unclear how such a thermodynamic transformation occurs as a baroclinic vortex transitions to a warm-core TC. For this purpose, Fig. 3.9 shows the vertical cross sectional evolution of the relative vorticity, tangential winds and thermal anomalies of the WWB-vortex prior to and shortly after TCG. Note that the immediate influences of the MCSs could not be included in the cross sections, since they occur on the downtilt-right side of the tilted vortex where favorable upward

motion and latent heating are present (see Fig. 3.5).

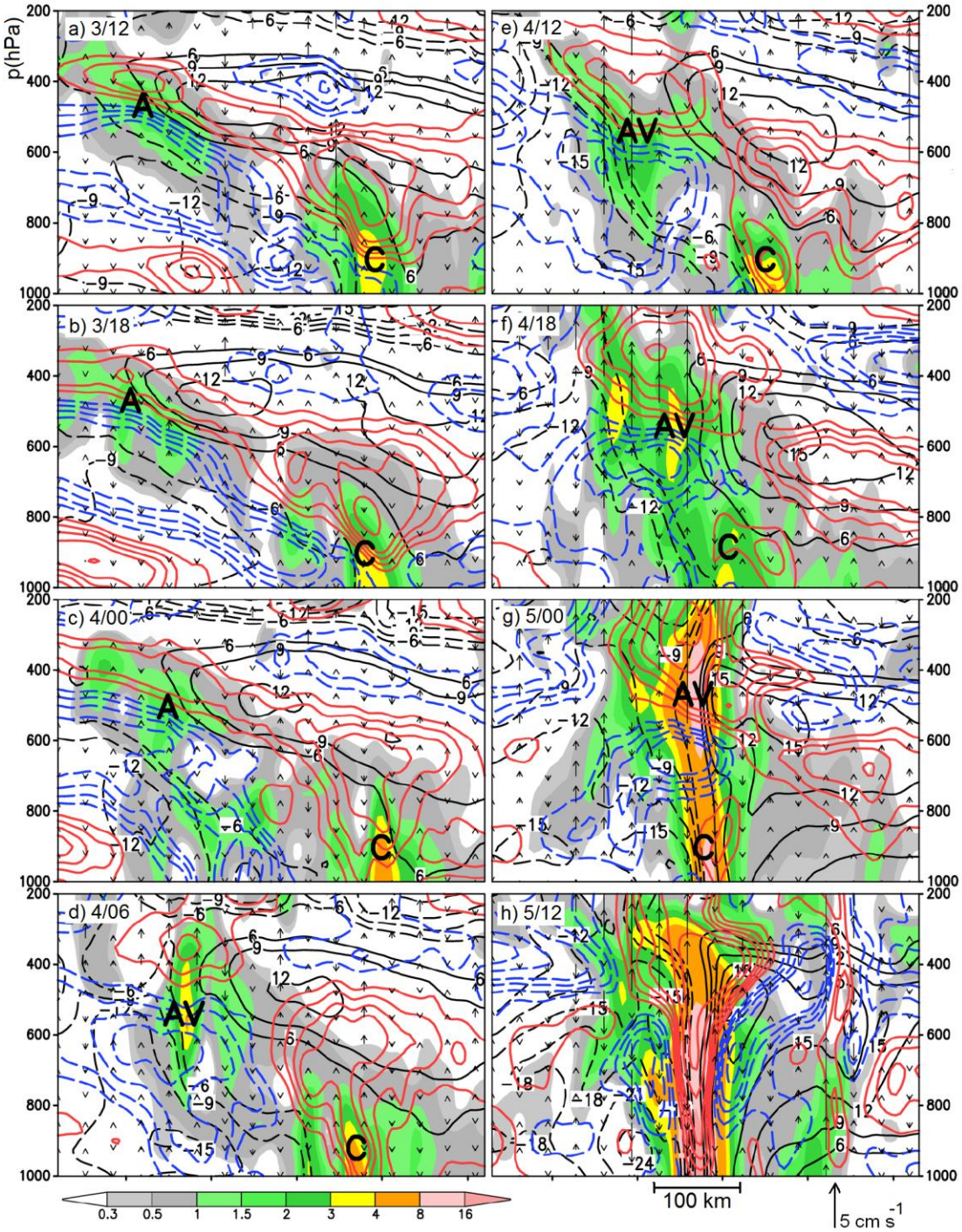


Figure 3.9. Vertical cross sections of the relative vorticity (shaded, $10^{-4}$ $s^{-1}$), the cross-plane wind speed into (out of) the vertical plane as black solid (dashed) contours (at 3 m $s^{-1}$ intervals), superimposed with deviation temperatures (colored contours, ± 0.2, 0.4, 0.6, 0.8, 1.2, 1.6 and 2.0°C), and vertical motion vectors. They are taken at (a) 3/12-156; (b) 3/18-162; (c) 4/00-168; (d) 4/06-174; (e) 4/12-180; (f) 4/18-186; (g) 5/00-192; and (h) 5/12-204 from the 6-km resolution domain. Each field has been laterally averaged within a 36-km to show more representative features.

It is obvious that the WWB-vortex decreases its vertical tilt during the pre-genesis period (Figs. 3.9a-g), namely, the horizontal distance between A and C decreases from 450 to 200 km during the 24-h period of 3/12-156 and 4/12-180. However, the mid- and low-level vortex layers appear to evolve separately by different mechanisms. That is, the midlevel vortex A amplifies in both magnitude and depth in the layers where little precipitation is present, so it must result from the absorption of the MCV and CGVs from several MCSs, as discussed in section 3.3. By comparison, the low-level circulation C maintains a nearly constant magnitude owing to the latent heat release along the arc-shaped rainband nearby, but its depth remains below 700 hPa until 4/18-186. Significant upward motion near the center of AV can be noted, which is convectively rooted in the rainband associated with C (cf. Figs. 3.9e-f and 3.5j-m). Thus, the tilted vortex exhibits two peak cyclonic vorticity centers with large circulation asymmetries prior to genesis (see Figs. 3.9a-e). All these differ from those observed in the dry simulation, in which the positive relative vorticity is more uniformly tilted between 500 and 900 hPa (Figs. 3.8a,b).

There are also two radii of the maximum tangential wind (RMW) during pre-genesis: one in the 400-600 hPa layer and the other in the lowest 200-hPa layer, and they persist even 12 h after genesis, i.e., at 5/12-204 (see Figs. 3.4b and 3.9). Specifically, the midlevel peak tangential wind in the cross sections increases from 12 to 21 m $s^{-1}$ with reduced asymmetries while its associated RMW decreases from near 500 km at 3/00-144 to 150 km at 4/18-186, and to about 50 km at 5/12-204, indicating the spin-up of the midlevel cyclonic circulation. In contrast, the low-level

tangential winds increase slowly, e.g., from 12 to 15 m $s^{-1}$ during this same period, but more rapidly to 24 m $s^{-1}$ by 5/12-204; and they remain highly asymmetric even after TCG. All these are consistent with the growth of the system-scale cyclonic vorticity shown in Figs. 3.2b and 3.8c, and the circulation structures shown in Fig. 3.5.

One can see from Fig. 3.9 that large VWS in tangential flow (e.g., > 24 m $s^{-1}$ between 400 and 900 hPa at 3/12-156) is always present across the tilted vortex layer, which is consistent with the thermal gradient across the layer with a tilted warm (cool) layer above (below). Moreover, the vertical thermal couplet associated with AV is gradually separated from the low-level counterpart as the midlevel vortex amplifies. At some stage, AV resembles to a certain degree a barotropic vortex with a warm column above a cold one (e.g., see Figs. 3.9d,e), just like a single MCV shown in Zhang and Bao (1996b, see Figs. 3.4 and 3.5 therein). Of interest is that AV's cold column gradually erodes into the low-level C's warm-core region as the horizontal distance between the two shrinks. It is this cold erosion with low-$\theta_e$ air (Fig. 3.3c) into C's circulation that appears to play an important role in "braking" the growth of the low-level circulation, as indicated by the elevation and weakening of its associated warm column (cf. Figs. 3.4b and 3.9a-f). It also accounts for the suppression of deep convection on the downtilt-left side of the WWB-vortex through weak mesoscale subsidence, as evidenced by a warm anomaly underneath AV (see Figs. 3.9a-c and 3.3d).

Of significance is that AV's cold anomaly could erode into and eliminate entirely the upper portion of C's warm core even when AV and C are vertically

aligned at 5/00-192. Apparently, the transformation of the WWB-vortex to a warm-cored TC would not be complete if such a cold anomaly is present. Nonetheless, the vertical alignment could cause a net increase of the warm-core depth (and intensity) above C, which would hydrostatically result in the surface pressure falls and the triggering of the wind-induced surface heat exchange (WISHE) processes (Emanuel 1987), as indicated by the increased surface winds, surface heat fluxes and pressure falls (see Figs. 3.2a and 3.9f-h). In this regard, the vortical contribution of deep convection to the midlevel system-scale cyclonic vorticity, as shown in Figs. 3.2b and 3.8, should be considered as the slow build-up of a balanced warm core that can cause hydrostatic pressure falls at the surface while increasing the midlevel cyclonic rotation, especially when it is superimposed onto a low-level cyclonic circulation. Indeed, the midlevel cold anomaly in the core region is completely gone shortly after the genesis of Chanchu, thereby achieving the thermodynamic transformation to a deep warm-cored TC (cf. Figs. 3.9g,h). The subsidence warming induced by diabatic heating in the inner-core region must play an important role in eliminating the cold anomaly.

The trigger of the WISHE processes leading to TCG has attracted some attention in the recent literature. Kieu and Zhang (2008) show the important role of vortex merger in the rapid increase of surface heat fluxes and the trigger of TCG leading to Tropical Storm Eugene (2005). From the simulation of an idealized mesovortex, Nolan (2007) finds that the key to TCG is the convective moistening over a sufficient depth of the troposphere in the core region of the vortex. A recent study by Camargo et al. (2009) also shows that the relative humidity (RH) is the most

important contribution of the MJO to TCG. To examine to what extent Nolan's finding could be applied to the present case, the pressure-time cross sections of several area-averaged quantities centered at C during a 3-day period encompassing the pre-genesis and genesis stages are given in Fig. 3.10, which shows that RH and $\theta_e$ remain nearly constant prior to 4/00-168, with RH < 80% above 900 hPa. Subsequently, both quantities increase. That is, the storm-scale RH of 85% (80%) extends to 850 (750) hPa after the life cycles of MCS1–MCS3, and then remains nearly steady during the life cycle of MCS4. Such high RH is considered by Nolan (2007) as one of the preconditions for TCG, but the genesis of Chanchu and rapid increase in surface fluxes and surface $\theta_e$ value in the present case do not occur until the vortex becomes upright during the life cycle of MCS4. This implies that a deep-layered humidification of the troposphere may be at most a necessary but not sufficient condition for TCG. On the other hand, given the moist environment, we may state that *the formation of an upright vortex in the present case is a sufficient condition for the trigger of TCG*. The intense warm-cored column allows the rapid fall of central pressure, leading to the positive feedback between the sea-surface winds, heat fluxes, and latent heat release, i.e., the trigger of the WISHE process (see Fig. 3.2). This mechanism may account for the tropical transition of many Atlantic TCs that have a baroclinic origin (Davis and Bosart 2004).

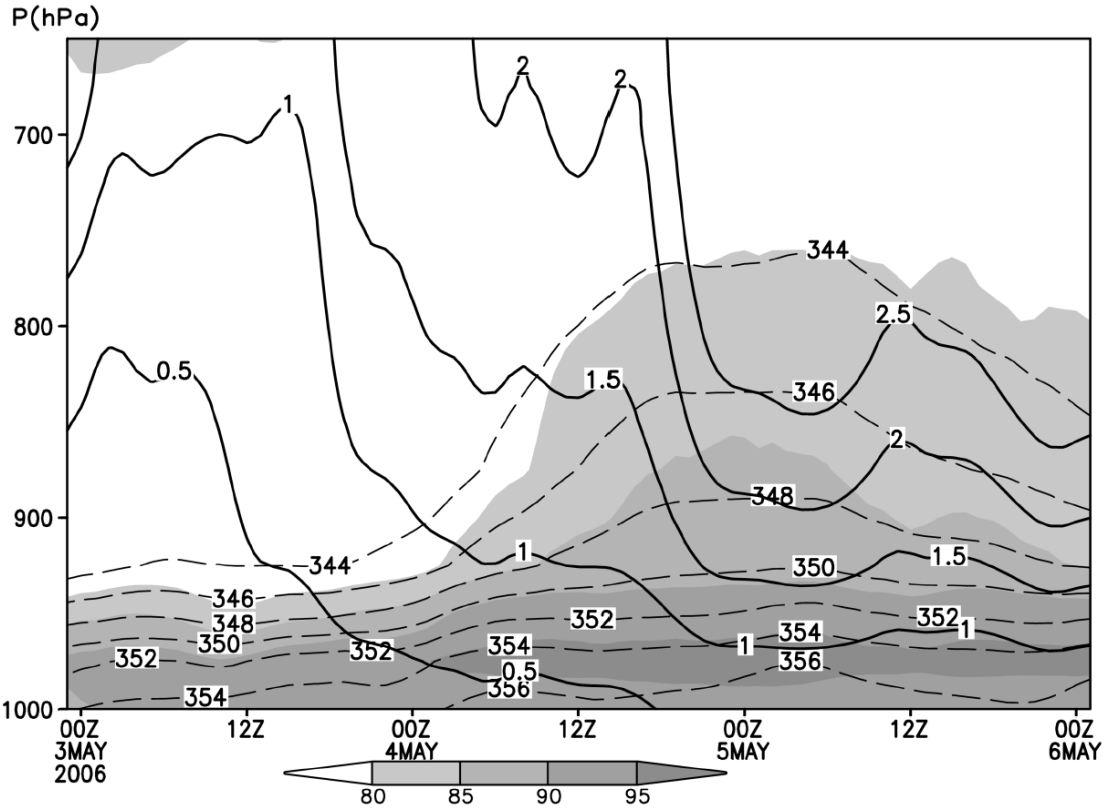


Figure 3.10. Pressure-time cross section of the storm-scale relative humidity (shaded, %) and equivalent potential temperature ($\theta_e$, dashed contours at intervals of 2 K above 344 K), and vertical motion (heavy solid contours at intervals of 0.5 cm $s^{-1}$) during the period of 3/00-144 and 6/00-216 from the 6-km resolution domain.

*3.5. Summary and conclusions*

In this study, we examined the life cycles of four major MCSs and the resulting thermodynamic transformation of a tilted WWB-vortex to the warm-cored Typhoon Chanchu (2006) near the equator. This is achieved through analysis of an 11-day cloud-resolving simulation of the case presented in Chapter 2 of this series of papers. The tilted WWB-vortex is shown to exhibit an elevated cold-cored layer below and a weak warm column above with large VWS across the vortex layer, and a surface-based warm-cored layer in the lowest 300 hPa that persists during pre-genesis; the cold and warm cores are separated over a horizontal distance of over 450 km. The

upper-level warm column increases in depth and intensity as a result of absorbing convectively generated cyclonic vorticity, including an MCV, from the MCSs. Despite the continued convective development during pre-genesis, the surface-based vortex remains as a TD with little deepening for more than 2 days due to the presence of large VWS. The subsequent superimposition of the midlevel baroclinic vortex with the lower-level warm-cored vortex triggers the genesis of Chanchu as the vertical tilt of the WWB-vortex diminishes.

Results show that the MCSs, developing on the downtilt-right side of the WWB-vortex, develop as a squall line with trailing stratiform precipitation and an MCV at an early stage, to two arc-shaped convective clusters, and finally to a spiral rainband as the WWB-vortex decreases its vertical tilt. Once the rotational flows intensify sufficiently near the onset of genesis, the results conform to the downshear-left generation of precipitation associated with an upright TC vortex. Results also show that earlier MCSs tend to produce more intense cold pools, transforming intermittently to a new-shaped MCS under the influence of the tilted vortex. But few cold pools could be found when the downtilt right side of the WWB-vortex becomes sufficiently moist, especially within the final large MCS, i.e., the spiral rainband exhibiting broad and deep slanting updrafts with little downdrafts. Despite the convective moistening of the lower troposphere, the genesis of Chanchu is not triggered until the cold-cored WWB-vortex begins its transformation to a deep warm-cored tropical cyclone.

Of importance is that the system-scale circulations intensify more rapidly in the midtroposphere than the layers below during the pre-genesis stage. The

amplification of the midlevel vortex circulations, which are out of phase with the lower-level circulations, could be attributed to the accumulation of an MCV and convectively generated cyclonic vorticity, thereby accounting for the formation of the above-mentioned deep warm columns aloft. In Chapter 4 of this series of papers, we will continue to examine the impact of convective processes on the amplification of the midlevel circulations during the pre-genesis stage, but at the convective scale using the 2-km resolution model results, and attempt to understand the mechanisms whereby the *surface* circulation amplifies after the WWB-vortex becomes vertically upright.

# Chapter 4: Storm-Scale Genesis of Chanchu

## *4.1. Introduction*

A sufficient mechanism or a so-called trigger of tropical cyclogenesis (TCG) continues to elude understanding. Precursor disturbances of wide-ranging origin can provide favorable conditions for TCG, but the processes that comprise TCG within each precursor scenario are still largely unknown. The general lack of understanding of TCG can probably be ascribed to the dearth of comprehensive observational data in the global TCG areas, as the geneses of other rotating storms that occur over land (e.g. the midlatitude cyclone and the supercell) are more thoroughly understood. Might it be possible that TCG, similar to the evolution of other rotating storms, occurs in a relatively invariant manner despite the array of TC precursors?

The air-sea interaction (WISHE, Emanuel 1987) by which a pre-existing tropical disturbance can undergo self-sustaining intensification is well understood, but the manner in which the lucky minority of pre-existing disturbances reaches the threshold for the invocation of WISHE is the essence of the TCG problem. From a dynamic point of view, the vorticity must increase sufficiently near the ocean surface, and at a scale significantly smaller than that of its precursor. Recent studies on TCG frame the problem of near-surface vorticity production in the top-down, bottom-up paradigm, where the threshold for WISHE is reached by stochastic processes. For example, deep vortical hot towers (Hendricks et al. 2004) may amalgamate and result in the upward growth of vorticity, or mesoscale convective vortices (MCVs) may interact (Simpson et al. 1997) in the midlevels and increase their penetration depth

toward the surface. The implicit stochasticity in both TCG pathways provides no obvious avenue by which to improve the predictability of TCG.

The TC is not the only phenomenon for which the development of an intense vertical column of mesoscale vorticity persists as a research issue. Supercells (Browning 1964) are intense rotating thunderstorms, characterized always by strong mesocyclones in the midlevels and sometimes by strong low-level rotation and an attendant tornado. The mechanisms responsible for the generation of midlevel vorticity in supercells are well known as the tilting of environmental shear-generated horizontal vorticity and subsequent stretching in deep updrafts (Barnes 1970; Rotunno 1981). While tilting of horizontal vorticity by an updraft creates two symmetric counter-rotating vortices, the vast majority of supercells exhibit cyclonic rotation (Davies-Jones 1985). Maddox (1976) and Klemp and Wilhelmson (1978) showed that the predominance of cyclonic supercells is associated with their preferred development in environments in which the shear vector turns cyclonically with height. The turning of the shear vector selectively enhances (suppresses) updraft growth on cyclonic (anticyclonic) flank of the updraft (Rotunno and Klemp 1982), leading to net generation of cyclonic midlevel vorticity.

The mechanisms for low-level vorticity generation in the supercell are similarly related to the cyclonically-turning shear vector, which favors the development of low-level streamwise horizontal vorticity (Davies-Jones 1984), i.e., that which has a component parallel to the flow. Parcels with streamwise vorticity immediately acquire cyclonic vorticity when tilted by an updraft and are subsequently stretched (Klemp and Rotunno 1983). A reason for the relative success in

understanding supercell low-level spin-up is that the convective structure of the supercells that sometimes spawn tornadoes is well-known and can be identified prior to the development of the tornado, allowing rapid mobilization of nonstationary observation networks near the incipient storm (e.g. the VORTEX field experiment, Rasmussen et al. 1994). Up to now, however, no such general structure of tropical convection that may spawn a mesoscale TC circulation has been identified; of course, observational challenges in the TCG environment are enormous.

Lemon and Doswell (1979) draw an analogy between the qualitative similarities of the supercell and the midlatitude cyclone, with the primary difference being horizontal scale. Tornado formation occurs in an area known as the hook echo, which is a radar manifestation of the downdraft wrapping around the updraft. The explosive midlatitude cyclone exhibits a similar comma-shaped cloud structure at peak intensity, as the storm occludes. The comma cloud typically marks the end of midlatitude baroclinic intensification, as the upper- and lower-level circulation centers become vertically stacked. The location of minimum surface pressure in both a tornado and a midlatitude cyclone occurs at the interface of the wrap-around precipitation and the clear slot. Both systems reach peak intensity as the clear slot develops, and both weaken soon after occlusion. Marquis et al. (2009) show observations of a Texas tornado that appears completely encircled by low-$\theta_e$ air at peak intensity, i.e. after the occlusion.

In terms of horizontal scale, the TC falls between the supercell and the midlatitude cyclone, both of which undergo amplification of near-surface vorticity. The TCG process has not been thoroughly compared to the geneses of other rotating

storms up to now for an obvious reason: the other geneses occur in highly sheared environments, while it is widely understood that vertical shear is unfavorable for TCG. The few studies on the baroclinic development of TCs are thus limited in number and confined to the midlatitudes where shear can be significant (e.g. Davis and Bosart 2001; Zhang and Bao 1996). Hulme and Martin (2009) found that TCG is favored when the occlusion of a midlatitude cyclone occurs warm ocean water, the so-called tropical transition.

While recent studies on TCG seem to represent a growing consensus that the bottom-up route is more plausible (Houze et al. 2009; Kieu and Zhang 2009) than top-down, the present chapter aims to frame the TCG problem in the context of more well-understood rotating storms and provide evidence that TCG may indeed proceed in a more deterministic manner than that provided by the top-down, bottom-up frameworks. As a first step, it has been noticed that genesis is often preceded by a large, coherent MCS that contains an exceptionally broad, downdraft-free updraft region (Houze et al. 2009; Hogsett and Zhang 2009b) and can take on the comma (or more conventionally "spiral band") shape (Zipser and Gautier 1978; Stossmeister and Barnes 1992). The present chapter revisits TCG in the deep tropics as a unique sub-synoptic phenomenon that, at least for the present case, can be placed in a spectrum of rotating storms that spawn near-surface vortices, at a scale between midlatitude cyclones and the supercell.

In Chapter 2, we presented a cloud-resolving simulation of the genesis of Typhoon Chanchu, which developed in the near-equatorial west Pacific during the active phase of the MJO. The westerly wind burst associated with the MJO

modulated low-level vorticity and convection, and Chanchu developed after an eight-day pre-genesis period. We found that because the WWB tilted westward with height, the resulting vortex also tilted westward with height, leading to forced isentropic ascent on its downtilt-right side. During the lead-up to genesis, the tilted vortex became more vertically upright in the presence of persistent downtilt-right precipitation.

In Chapter 3, we investigated the mesoscale evolution of the pre-genesis, downtilt-right precipitation, which took the form of squall lines and convective clusters with large areas of stratiform precipitation. One of the MCSs left a strong MCV in its wake that merged with and strengthened the midlevel circulation, in the manner discussed by Ritchie and Holland (1997). The first three of four MCSs left cold outflow near the surface, along which the subsequent MCSs developed. The fourth and final MCS (i.e., MCS4) left no cold pool prior to genesis, though it exhibited larger size than any of the previous three and exhibited a downdraft-free updraft region and a spiral shape, similar to those investigated by Zipser and Gautier (1978) and Houze et al. (2009). Apparently, the first three MCSs served to precondition the environment by raising low- and midlevel RH.

In Chapter 4 of this dissertation, we present results from the finest 2-km nest of the WRF simulation discussed in Chapter 2 and emphasize the evolution of MCS4 in a preconditioned and sheared (at the storm scale) environment. The finest nest tracks the low-level pre-Chanchu circulation from 3 – 7 May. The purposes of the present chapter are to (i) demonstrate how the genesis of Chanchu is related to the evolution of MCS4, which deforms into a spiral band and eventually occludes; (ii)

show that near-surface cyclonic vorticity is preferentially generated along a near-surface convergence zone; (iii) propose a unique pathway to genesis.

The next section provides an overview the storm-scale evolution of the incipient Chanchu before and after the threshold of TCG. Section 4.3 discusses the mechanisms by which the midlevel circulation intensifies prior to TCG. Section 4.4 shows the processes by which near-surface vorticity is rapidly enhanced and concentrated into a TC-scale circulation. Section 4.5 discusses the implications of the occlusion of MCS4. Section 4.6 compares the present TCG and the geneses of other rotating storms, and conclusions are given in the final section.

## *4.2. Storm-scale evolution*

In this chapter, we focus almost exclusively on the 24-h period centered on the onset of TCG, i.e. model hours 180 – 204, valid between 1200 UTC 4 May – 1200 UTC 5 May, hereafter 4/12-180 – 5/12-204. In this section we provide an overview of the near-storm environment, which we consider a roughly 500 x 500 km area that contains the entire tilted vortex and the relevant downtilt-right precipitation while following the storm.

### *4.2.1. 12 h prior to genesis*

During the 12 h prior to genesis, the large scale vertical shear remains below 6 m $s^{-1}$ (Fig. 2.8) and thus favorable for storm intensification. The storm scale 900 – 400 hPa shear, on the other hand, remains westerly (Fig. 4.1) with a nearly constant magnitude of 20 m $s^{-1}$ throughout the period under study. Since the incipient disturbance exhibits a northwest-southeast vertical tilt and peak vorticity occurs in the midlevels (see Fig. 4.2), the westerly 900 – 400 hPa shear in Fig. 4.1 can be

considered as "self-imposed" by the midlevel portion of the tilted vortex onto that in the low levels. Because the relative vorticity of the pre-Chanchu disturbance diminishes above 500 hPa (see Fig. 4.2), perhaps the typical shear calculation that extends into the upper troposphere is not appropriate during the pre-genesis period. For this reason, we confine the subsequent discussion to the vertical shear between the 400 and 900 hPa levels.

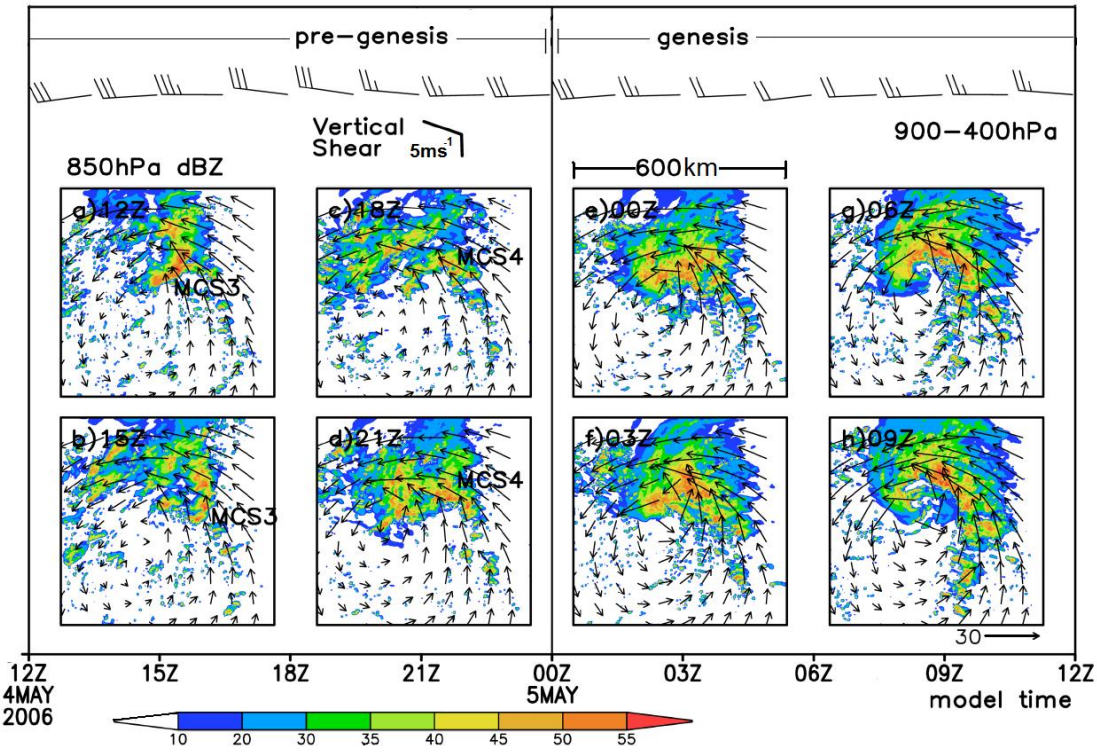


Figure 4.1. Time series (90 min) of the area-averaged (500 x 500 km) vertical shear (m $s^{-1}$) between 900 – 200 hPa (heavy barbs) and 900 – 500 hPa (light barbs) between 1200 UTC 4 May – 1200 UTC 5 May. In (a) – (h), the horizontal distribution of 850-hPa precipitation fields (dBZ, shaded) from the finest 2-km nest, superposed by the 850-hPa flow vectors from 1200 UTC 4 May – 1200 UTC 5 May, at 3-h intervals.

The precipitation during pre-genesis (Fig. 4.1a-d) is triggered and maintained by forced isentropic ascent on the downtilt-right (i.e. north) side of this tilted vortex (Jones 1995; Frank and Ritchie 1999), as detailed in Chapter 2, while the downtilt-left half remains largely precipitation-free. The downtilt-right precipitation consists of

MCS3, which propagates from west to east and decays (Fig. 4.1a,b), and MCS4, which subsequently develops along the cold pool of MCS3 (Fig. 4.1c) and begins to take on the spiral shape by 4/21-189 (Fig. 4.1d). As MCS4 intensifies, the magnitude of the area- and layer-mean vertical motion doubles during the 6 h prior to genesis (Fig. 4.2), during which time the vertical tilt diminishes from nearly 200 km to less than 50 km (Chapter 3, Fig. 3.9). During the rapid intensification of MCS4, the mean 600-hPa vorticity increases by 7 x $10^{-5}$ $s^{-1}$ during the 9 h prior to TCG (Fig. 4.2), while the mean vorticity at 900-hPa increases by only 4 x $10^{-5}$ $s^{-1}$ and the minimum pressure remains relatively constant. The mechanisms by which the midlevel vortex intensifies prior to the onset of TCG will be discussed in the next section.

*4.2.2. Onset of genesis*

As mentioned above, the midlevel vertical shear does not diminish as TCG begins (Fig. 4.1). MCS4 transitions into a primary rainband (Figs. 4.1e,f), which is typical of incipient TCs (Willoughby et al. 1984), and by 5/03-195 the low-level circulation begins to exhibit a small-scale intense circulation south of the peak spiral band convection (Fig. 4.1f). By 5/06-198 (Fig. 4.1g) a nascent eye begins to appear and the comma shape is even more obvious. The persistence of a 20 m $s^{-1}$ 900 – 400 hPa shear (Fig. 4.1) during TCG shows clearly that the vortex still exhibits some vertical tilt. As discussed in Chapter 2, only in the immediate vicinity of the circulation center is the vortex upright. The spiral band persists in a highly vertically sheared environment. Thus the downtilt-right thinking can be applied to the pattern of precipitation for some time after the onset of genesis. The notion that the inner core exhibits less tilt that the far-field flow can be seen in Fig. 4.1h: a quasi-axisymmetric

area of precipitation is obvious near the upright core, but the outer rainband continues to exhibit a spiral structure. The physical relationship between the spiral band and vertically sheared flow will be discussed in the next section.

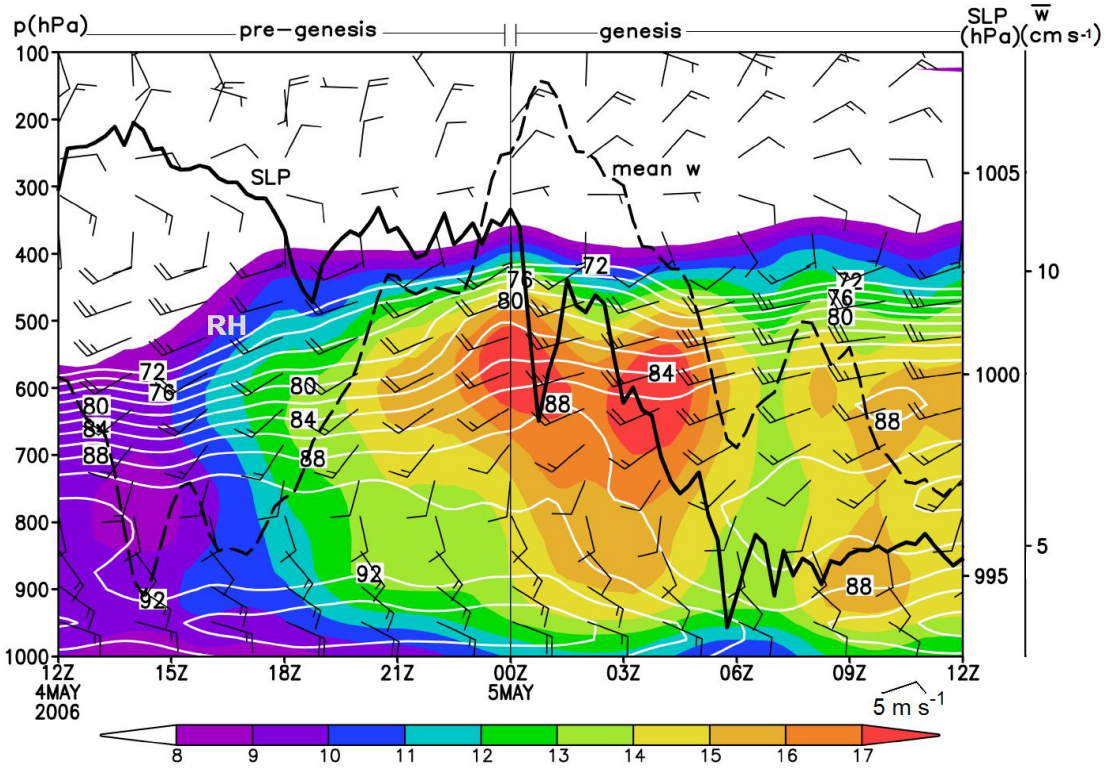


Figure 4.2. Time–height cross section (15 min) of the area-averaged (500 x 500 km) relative vorticity (x $10^{-5}$ $s^{-1}$, shaded), relative humidity (%, contoured at intervals of 3% above 72%), and wind barbs (m $s^{-1}$, 2-h intervals). The minimum surface pressure (solid contour, hPa) and the 900 – 400 hPa mean area-averaged (500 x 500 km) vertical motion (dashed, cm $s^{-1}$) are superposed.

The minimum central pressure begins to fall rapidly near 5/00-192 (Fig. 4.2) and decreases by 11 hPa during 5/00-192 – 5/06-198. We consider this the onset of TCG. In Chapter 3, we show that during pre-genesis the mean vertical motion and RH increase in association with the low-level humidification and the intensification of MCS4, i.e., preconditioning (Nolan 2007). Interestingly, the storm-scale RH and mean vertical motion *decrease* during the first 6-h period of rapid deepening (Fig.

4.2). The temporary dehumidification and decreasing upward motion suggest the increasing prevalence of downdrafts in the low- and mid-troposphere. A goal of this chapter is to reconcile the apparent discrepancy between midlevel downdrafts and concurrent rapid intensification. *How does rapid spin-up occur at the surface when the mean vertical motion is rapidly decreasing?*

After the initial 6-h deepening period, the surface pressure ceases deepening temporarily, low-level RH begins to increase again, and area-averaged low-level relative vorticity exhibits a temporary minimum (Fig. 4.2). After this 6-h period of intensity maintenance, Chanchu deepens at a more constant rate throughout the remainder of the simulation (Chapter 3, Fig. 3.2a). *Why does intensification, in terms of minimum pressure, cease (temporarily) after the initial onset of TCG?* In the next two sections we attempt to answer the above questions.

## *4.3. Midlevel vortex enhancement*

To understand genesis, we must first understand why the midlevel vorticity increases more rapidly than the near-surface vorticity prior to the onset of TCG. To this end, we aim to understand the relationship between the vertical wind shear and the transition of MCS4 into a spiral band (c.f. Figs. 4.1d,h). The vertical structure of the wind profile in the highly-sheared, near-MCS4 environment may hold the key to genesis (Fig. 4.2).

### *4.3.1. Potential mechanism for midlevel generation*

Supercell thunderstorms are also well-known to exhibit a rapid increase in cyclonic midlevel rotation due to their prevalence in environments with veering wind profiles (Fig. 4.3a). As shown by Rotunno (1981), the midlevel rotation in a supercell

arises due to the tilting of environmental westerly vertical shear by a vigorous updraft, which leads to a pair of counter rotating vertical vortices. However, because the shear vector rotates cyclonically with height (i.e., it veers), Rotunno and Klemp (1982) showed that dynamically-induced vertical pressure gradients develop on both flanks of the updraft such that the cyclonically rotating member of the pair (i.e. that to the right of the midlevel shear) is favored for enhanced vertical motion and new updraft growth. The vertical motion associated with the anticyclonic member of the tilt couplet, conversely, is suppressed. Thus environments with a cyclonically curved hodograph favor a net increase in midlevel cyclonic vorticity via tilting of shear-generated horizontal vorticity by updrafts.

Fig. 4.3b shows that the hodograph in the present case exhibits cyclonic turning with height, similar to that characteristic of the most intense supercells, which always develop intense midlevel mesocyclones and often spawn near-surface vortices. Of course, the hodograph is simply another method of representing the veering wind profile shown in Fig. 4.2. The implication is that every discrete updraft triggered in this environment will not only tilt environmental shear vorticity, but will acquire net cyclonic vorticity due to preferential generation on the cyclonic flank (in this case, to the south).

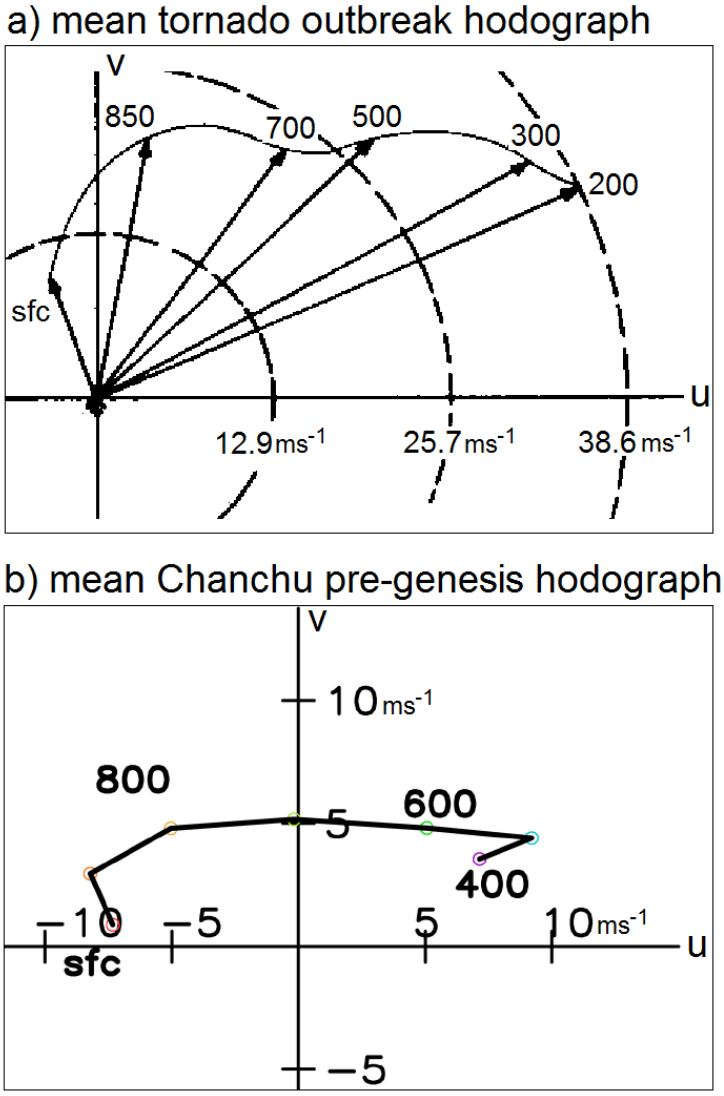


Figure 4.3. Hodographs for (a) the average of 23 soundings taken in the proximity of a tornado outbreak, adapted from Maddox (1976), and (b) the area-averaged (500 x 500 km) environment prior to the genesis of Chanchu. Note the cyclonic turning with height in (a) and (b).

*4.3.2. Midlevel vortex structure*

In order to demonstrate the mechanisms for the increase in midlevel vorticity, we show the storm-scale structure of the pre-Chanchu disturbance in Fig. 4.4, during the transition to genesis from 4/21-199 – 5/0330-195.5. The simulation captures a broad cyclonic circulation at 500 hPa (Fig. 4.4a), a poorly organized MCS4 (Fig.

4.4e) northwest of the 850-hPa circulation center at 4/21-189, and a weak convergence zone near the surface (Fig. 4.4i). The convergence zone separates a relatively low-$\theta_e$ airmass beneath MCS4 from the high-$\theta_e$ airmass, which feeds into MCS4 from the southeast. The temperature gradient across this convergence zone (not shown) does not exceed 1 K.

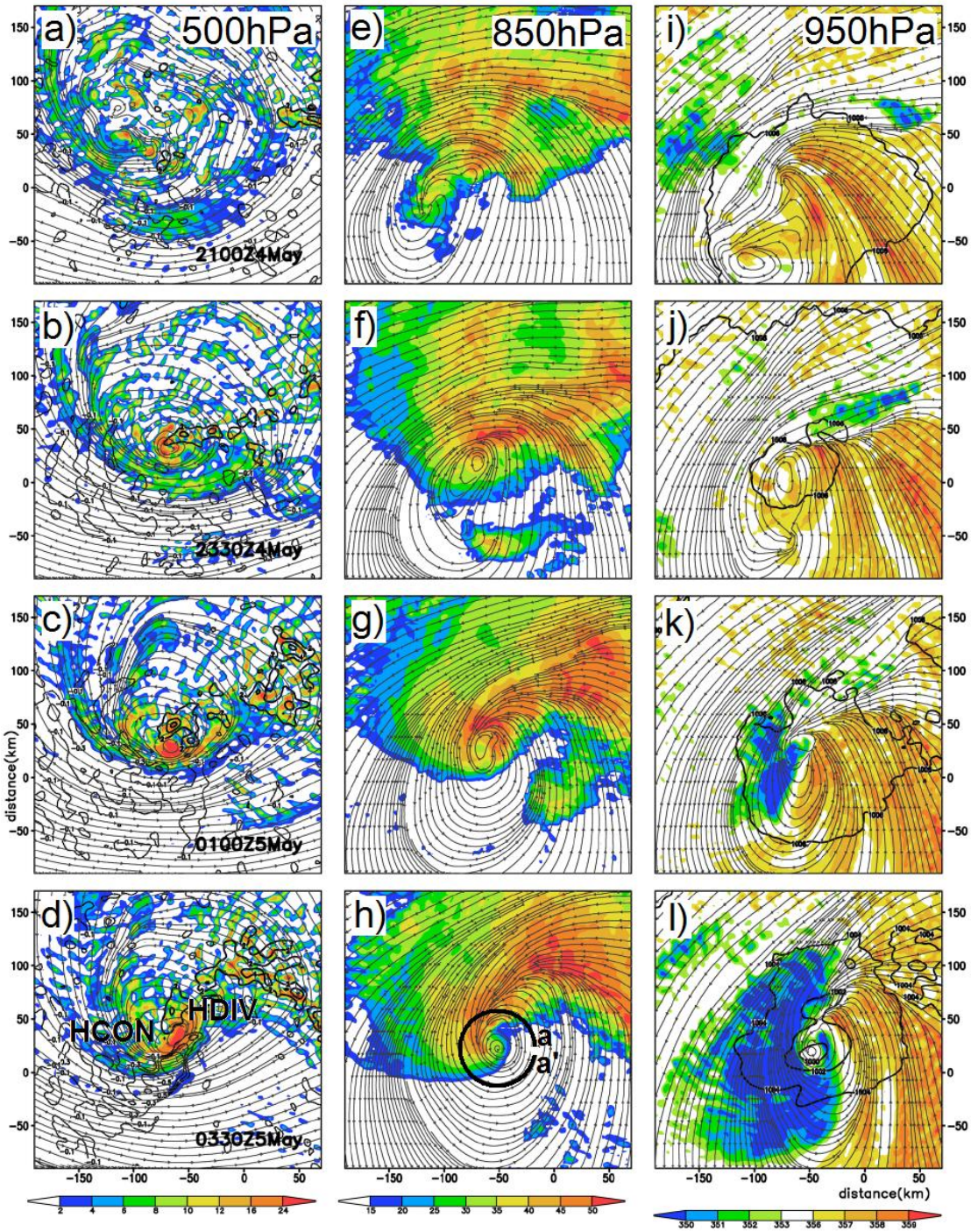


Figure 4.4. Horizontal distribution of (a-d, left panel) 500-hPa relative vorticity (x $10^{-5}$ $s^{-1}$), (e-h, center panel) 850-hPa radar reflectivity (dBZ), and (i-l, right panel) 950-hPa equivalent potential temperature $\theta_e$ (K), all shaded from 2100 UTC 4 May (top row) – 0330 UTC 5 May (bottom row) at 150-min intervals. In (d), areas of enhanced horizontal convergence (HCON) and divergence (HDIV) are shown. In (h), the path of the circular cross section (a – a') for Figure 4.7 is shown as the heavy solid arc. In (i-l), surface pressure (at intervals of 1 hPa) is contoured, and streamlines are superposed at each level.

By 4/2330-191.5, a well-defined 500-hPa vorticity maximum develops within the circulation center (Fig. 4.4b), and in association with enhanced midlevel difluence downstream of the center (Fig. 4.4b), convection organizes along the increasingly sharp convergence zone (Fig. 4.4j). Of interest is that the 500-hPa vorticity maximum develops not in the center of the 500-hPa circulation, as might be expected from a series of random vortex mergers. Instead it develops along the southern periphery of the broad midlevel circulation (Fig. 4.4b) and immediately to the south of the strongest upward motion (Fig. 4.4b).

The location of peak midlevel vorticity is not coincidental or random. Instead, the vertical motion associated with the intensifying convection tilts the shear vorticity, which leads to preferential generation on the southern flank of the updraft. The 500-hPa vorticity maximum develops at exactly the location where the 500-hPa flow passes over the 850-hPa circulation center (c.f., Figs. 4.4b,f), i.e., where the horizontal shear is greatest (not shown), and to the south of the updraft maxima. This process is summarized in Fig. 4.5, and begins with the shear-generated horizontal vorticity that generally points northward in the midlevels (Fig. 4.5a). As updrafts associated with MCS4 tilt the horizontal vorticity, a vertical vorticity couplet (Fig. 4.5b) is created with anticyclonic (cyclonic) vorticity generation to the north (south). Because the shear vector turns cyclonically with height, the southern cyclonic member of the tilting couplet is favored for strengthening (Fig. 4.5c) on the southern flank of the convection (Fig. 4.4b). On the northern flank of the updrafts, cyclonic vorticity is suppressed.

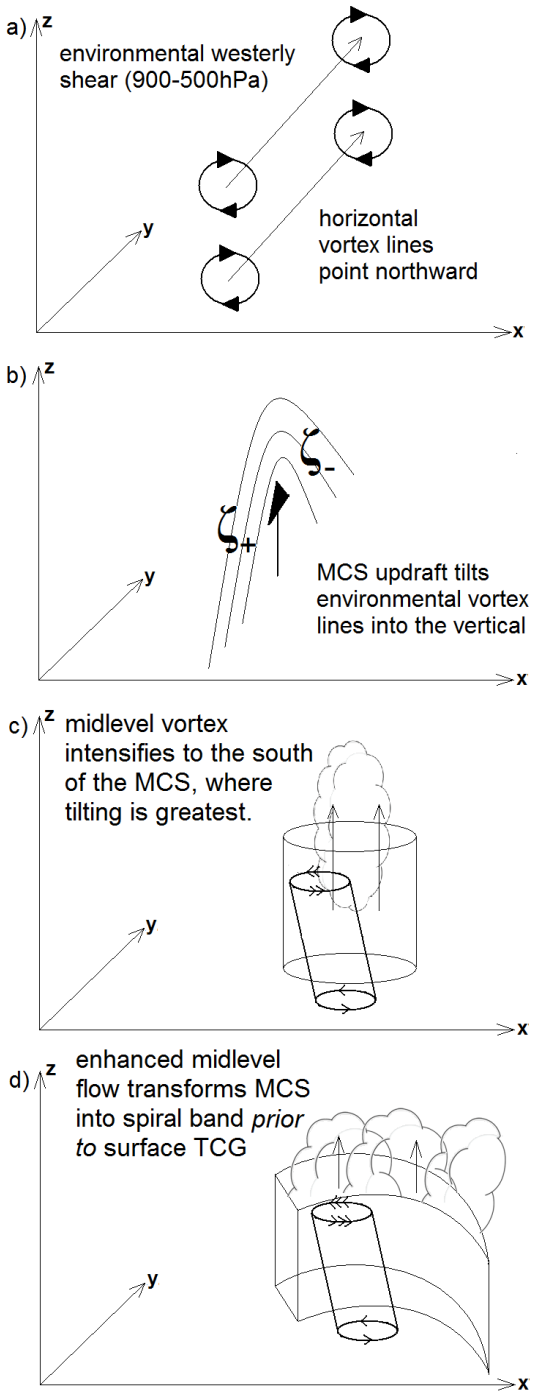


Figure 4.5. Conceptual model of midlevel intensification.

The increasingly intense midlevel vortex (Fig. 4.4c) remains peaked at the southern periphery of MCS4, which begins its transition into a spiral band (Fig. 4.4f) in response to increasing midlevel flow that advects the western (eastern) portion of

the MCS southward (northward). The only plausible explanation for the MCS-to-spiral-band transition is rapid midlevel vortex enhancement on the *southern flank* of the MCS. This process begins to occur prior to the onset of TCG (Fig. 4.5d), similar to the manner in which a supercell develops an inflow notch and "hook echo" just prior to the tornado phase. It is in this way that midlevel tilting-generated vorticity on the flank of the MCS4 triggers the transition from a general MCS into a spiral band. In section 4.4 we investigate the detailed structure of this convection in the context of the surface vortex spin-up.

In Fig. 4.6, we show the mean structures during the first 2-h period of TCG to further understand the ongoing processes. It is obvious from Fig. 4.6a that the location of the surface circulation occurs at the tip of the, for lack of a better term, "hook echo." However, because the circulation center in the midlevels is displaced slightly northwest of that in the low levels (cf. streamlines Figs. 4.6a,d), the local vertical shear in the core region remains large during this period. The implication of the vertical shear for the present discussion is that horizontal vorticity may be large, and thus in the vicinity of strong upward motion (or more specifically horizontal gradients of vertical motion), the vorticity tilting term may continue to be important for the evolution of the spiral band.

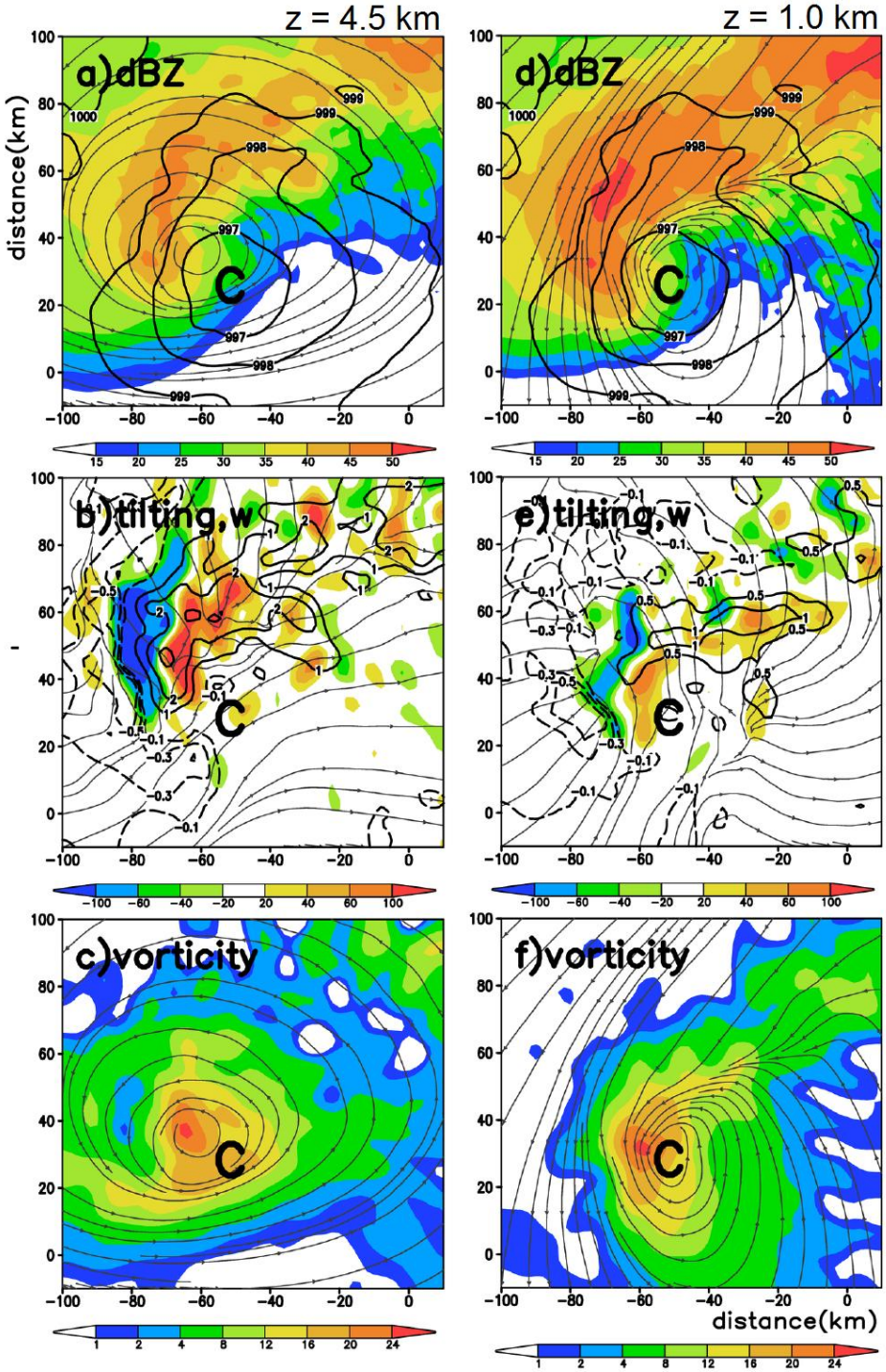


Figure 4.6. Horizontal distribution of radar reflectivity (dBZ, shaded, top row) and surface pressure (hPa, contours), the vorticity tilting term ( x $10^{-8}$ $s^{-2}$, shaded, middle row), and relative vorticity (x $10^{-4}$ $s^{-1}$, shaded, bottom row) at 4.5 km (a-c, left panel) and 1 km (d-f, right panel), taken as the 2-h average during 0230 - 0430 UTC 5 May. The horizontal streamlines are superposed in the top and bottom panels, and the local vertical shear streamlines between (b) 3.5 – 5.5 km and (e) 0.2 – 1.5 km are superposed in the middle panel.

In fact, Fig. 4.6b shows that the midlevel vertical motion exhibits a spiral pattern associated with the updrafts within the convective band. The local vertical shear has a component perpendicular to the gradient of vertical motion within the spiral band (see shear streamlines in Fig. 4.6b). As the updraft within the spiral band tilts the shear-generated horizontal vorticity, a dipole structure appears in the vortex tilting term. The tilting enhances (suppresses) cyclonic vorticity radially-inside of the spiral band. This process is simply a modification of the simplistic processes described in Fig. 4.5, and it has two consequences. First, midlevel vorticity exhibits a *net increase* to the downshear-right of the peak updraft, where the tilting is large (Fig. 4.4b-d), thus ensuring that the midlevel circulation center (and vorticity maximum, Fig. 4.4d) remains displaced toward the downshear-right flank of the peak convection (Fig. 4.6a). Second, the net vorticity generation inside the spiral band tends to deflect the midlevel vortex toward the tilting (Fig. 4.6c), which moves it closer to a vertically stacked position with the low-level vortex.

The negative portion of the tilting dipole occurs radially outside of the spiral band, and its magnitude is actually larger than the positive tilting due to the enhancement by the downdraft occurring on the outside (Fig. 4.6b). As found by Rotunno and Klemp (1982), the tilting-generated midlevel vorticity on the flanks of the updraft dynamically promote updraft (downdraft) growth on the downshear-right (-left). This suggests that while updrafts are dynamically favored inside the band, the pool of low-$\theta_e$ air that develops east of the circulation center (Fig. 4.4k) is dynamically forced from the midlevels where tilting promotes downward motion.

Of course, the net effect of the tilting dipole is not significant in an area-averaged sense, but it appears that tilting is critical to understand the location of midlevel vorticity maximum at the periphery of the MCS (Fig. 4.4b-d), the tendency of the MCS to transition into a spiral shape, and the continued location of the vorticity maximum at the flank of the spiral band. These results emphasize the criticality of the local vertical shear associated with the pre-Chanchu vortex; without vertical shear the vortex tilting term is unimportant. In fact, such a tilting mechanism has not been presented until now.

## *4.4. Initial surface deepening phase*

As the spiral band develops in association with midlevel vortex enhancement, related processes are occurring that favor near-surface TCG. Thus we aim to understand how the spiral band facilitates the 6-h period of initial surface intensification (Fig. 4.2).

### *4.4.1. Development of near-surface cold pool*

As convection intensifies by 5/01-193 along the convergence zone (Fig. 4.4g), the pool of near-surface low-$\theta_e$ air develops (Fig. 4.4k) northwest of the center and begins to advect cyclonically around the upshear portion of the low-level circulation. The low-$\theta_e$ pool develops as the mean vertical motion shifts to a negative trend (Fig. 4.2), likely as a dynamically-forced downdraft from the spiral band convection. The critical element of this evolution in relation to TCG is that the rapid deepening of surface pressure begins coincident with the formation of the surface low-$\theta_e$ pool and continues as the area covered with low-$\theta_e$ air grows larger (Fig. 4.4k,l). The low-$\theta_e$ air is thus not detrimental to genesis, as is often assumed. At 5/0330-195.5 MCS4

continues to evolve as a spiral band (Fig. 4.4h) as surface pressure continues its rapid fall (Fig. 4.4l), and a clear slot develops east of the center (Fig. 4.4h). The qualitative similarities between the processes described above and those that occur in a rapidly deepening midlatitude cyclone (Sanders 1986) and a supercell entering the tornado phase (Lemon and Doswell 1979) cannot be ignored. However, we reserve detailed comparisons for Section 4.6.

*4.4.2. Vertical structure of spiral band*

In Fig. 4.7, we show the vertical structure of the spiral band in the vicinity of the circulation center (see Fig. 4.4h). The updrafts initiate along the convergence zone in the northeast quadrant of the circulation, beneath an area of midlevel divergence (HDIV, Fig. 4.4d). Of course, HDIV is typically close to zero in the midlevels of a mature TC, but we emphasize that the processes ongoing are completely different than those within a mature TC. As parcels near the surface approach the convergence zone (Fig. 4.7, $0^o$ – $60^o$), they acquire cyclonic vorticity immediately upon ascent and take a slantwise vortical path due to the sheared flow in which they initiate. As the updrafts reach the 500-hPa level, they encounter strongly convergent horizontal flow (HCON, Fig. 4.4d), and thus ascend (descend) above (below) the 500-hPa level (Fig. 4.7, $180^o$). The most significant downdrafts occur in the southwest quadrant of the vortex, descend anticyclonically to the surface (Fig. 4.6), and likely transport the relatively low-$\theta_e$ air to the surface (Fig. 4.4l). The slantwise ascent that occurs within the sheared spiral band is critical to the longevity of the spiral band since downdrafts do not fall through and contaminate the updraft, as is well-known for supercells (Weisman and Klemp 1986).

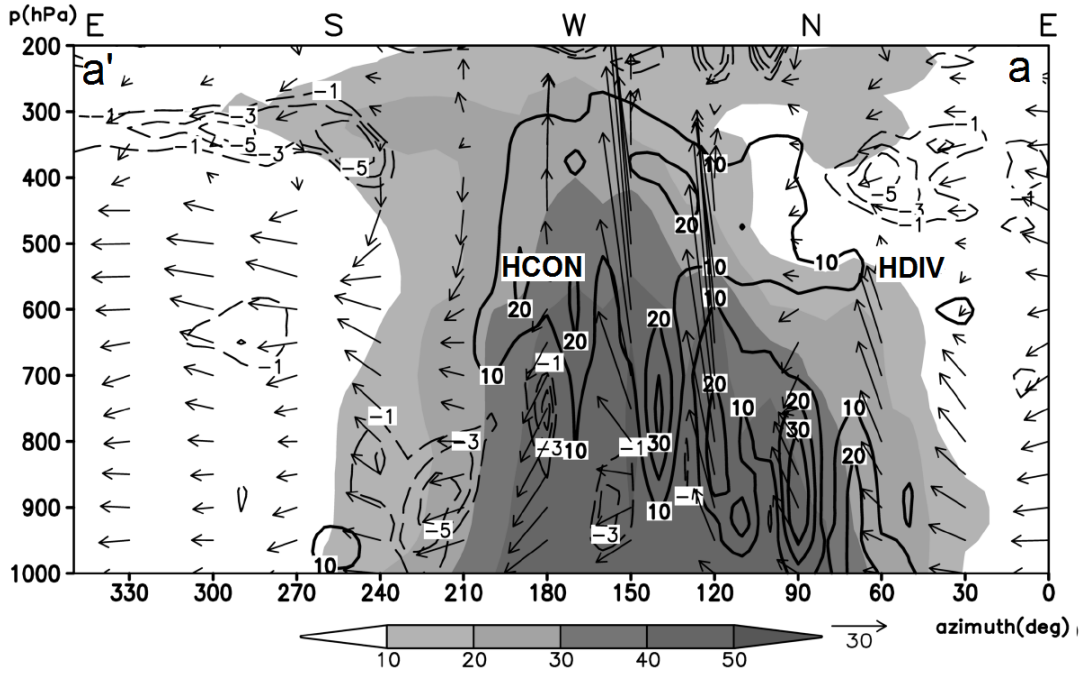


Figure 4.7. Height-azimuth cross section of radar reflectivity (dBZ, shaded) and relative vorticity (x $10^{-7}$ $s^{-1}$, contoured) at 0330 UTC 5 May, taken at a R = 30 km from the center of circulation, as shown in Figure 4.4h from a – a'. In-plane wind vectors (vertical motion enhanced by a factor of ten) are superposed. HCON and HDIV represent areas of midlevel horizontal convergence, as shown in Figure 4d.

*4.4.3. Low-level vorticity generation*

In the low levels (Fig. 4.6d), the mean precipitation structure during TCG is similar to that in the midlevels, but with a more pronounced radar reflectivity "hook." The convergence zone and circulation center lie at the inner edge of the hook. The processes by which net cyclonic vorticity is generated along the convergence zone and input into the primary circulation center are obviously critical to TCG.

Here we argue that vortex tilting plays the critical role by locally generating net cyclonic low-level vorticity along the convergence zone. Fig. 4.6e shows that the local shear vector in the vicinity of the convergence zone is southerly such that the low-level horizontal vorticity is oriented parallel to the easterly inflow along the convergence zone. Thus, the parcels flowing along the convergence zone have a

streamwise component of horizontal vorticity. To visualize the importance of streamwise vorticity in the present case, imagine a parcel flowing along the convergence zone toward the circulation center (Fig. 4.6d). As soon as the parcel encounters an updraft, the vertical cyclonic vorticity immediately increases via tilting (Davies-Jones 1984; Rotunno and Klemp 1985), and thus becomes immediately available for stretching. Conversely, a streamwise parcel that encounters a downdraft exhibits an immediate decrease in vertical cyclonic vorticity as it is tilted downward. However, since the convergence zone is updraft-dominated (Fig. 4.6e), we should expect net upward tilting and thus net vorticity generation in this region.

Fig. 4.8a shows that all of the parcels approaching the convergence zone have a streamwise component of horizontal vorticity. Thus, when the parcels that enter the convergence zone are tilted upward, net cyclonic low-level vorticity is generated along the convergence zone. The updrafts that initiate along the convergence zone are subsequently stretched along their vortical ascent, while the near-surface vorticity is advected along the boundary. As the low-level parcels along the convergence zone acquire cyclonic vorticity more rapidly than those away from the convergence zone, they take a spiral cyclonic route to the center. Streamwise vorticity is favored in environments with veering wind profiles (Fig. 4.2) and is known to be the source of low level rotation in supercell thunderstorms (Davies-Jones 1984). Because the net positive tilting occurs radially inside of the spiral band (Fig. 4.6e), each discrete updraft within the convective band tends to spiral inward toward the source of vorticity.

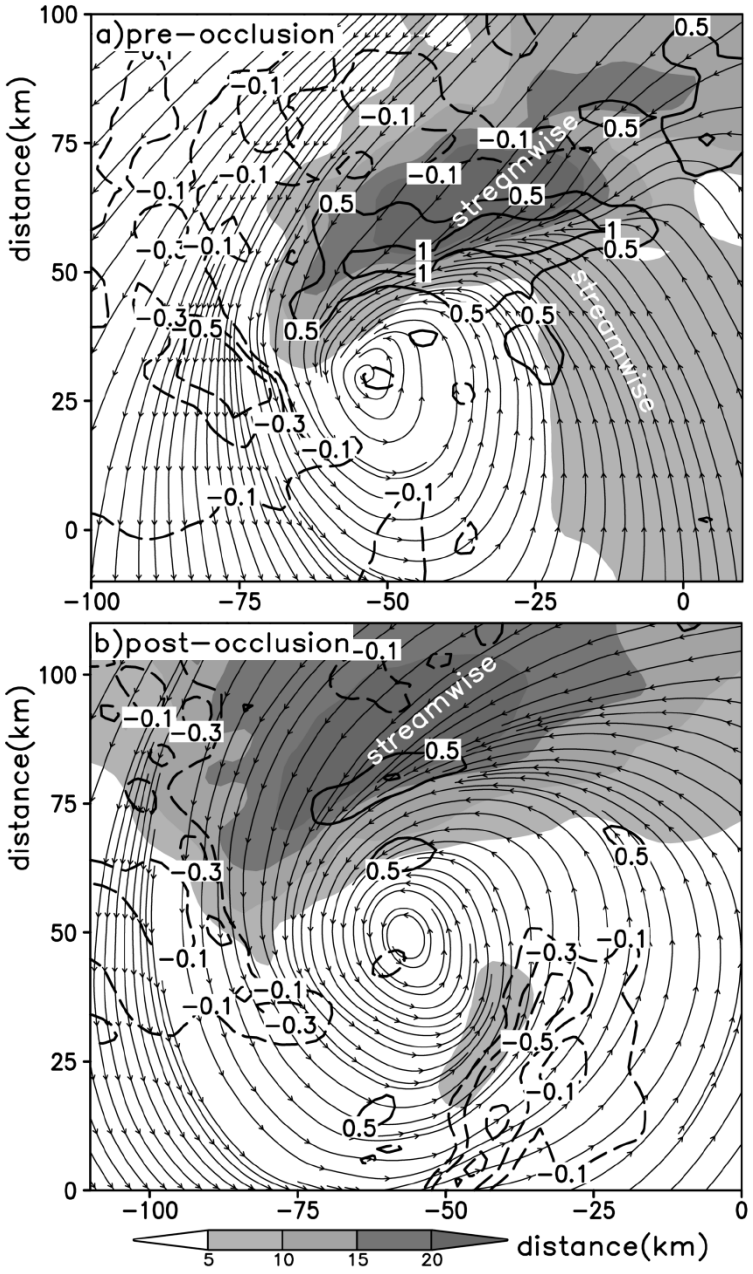


Figure 4.8. As in Fig. 4.6e, but for the mean streamwise vorticity (shaded) and vertical motion (contoured) in the sfc – 1.5 km layer during the (a) rapid intensification phase (i.e. pre-occlusion) and (b) maintenance phase (i.e. post-occlusion). Fields are time-averaged during (a) 0230 - 0430 and (b) 0730 – 0930 UTC 5 May.

Within and radially outward from the spiral band, downdrafts occur (Fig. 4.7e) and do not converge into the circulation center. It would be misleading to state that the downdrafts are *dispelled* from the circulation center; instead, there is simply

no mechanism by which they can acquire sufficient cyclonic vorticity to spiral inward at a similar rate to that occurring along the convergence zone. Thus the downdrafts remain radially outward of the inward-spiraling convective band. In this discussion of downdrafts, it is important to mention the importance of environmental preconditioning in facilitating TCG. The high environmental RH (Fig. 4.2) suppresses strong downdrafts, which could disrupt the processes ongoing along the convergence zone if they were strong enough to spread in all directions when they impacted the ground. In fact, Markowski and Richardson (2009) state that in environments with high low-level RH, the likelihood of supercell tornadoes increases due to the suppression of strong downdrafts.

*4.4.4. A discrete updraft along the convergence zone*

An individual updraft along the convergence zone is shown in Fig. 4.9a. It is the first of many similar convective features that comprise the convergence zone (near the time in Fig. 4.4f, just prior to TCG). A close inspection of this storm indicates that in scale and structure it resembles a supercell, which is not surprising since the environment in which it develops is conducive to such storm mode (Fig. 4.3b). The detailed structure of this storm is not the focus here, but of interest to TCG is that the near-surface vorticity in the "hook echo" reaches 0.01 $s^{-1}$, almost reaching the levels of a tornado. Such intense low-level vorticity cannot be generated quickly by simply stretching of ambient cyclonic vorticity. Instead, Fig. 4.9b shows that as inflow approaches the primary updraft it is indeed first tilted and then stretched. The tilting in advance of the primary updraft provides additional vorticity for stretching.

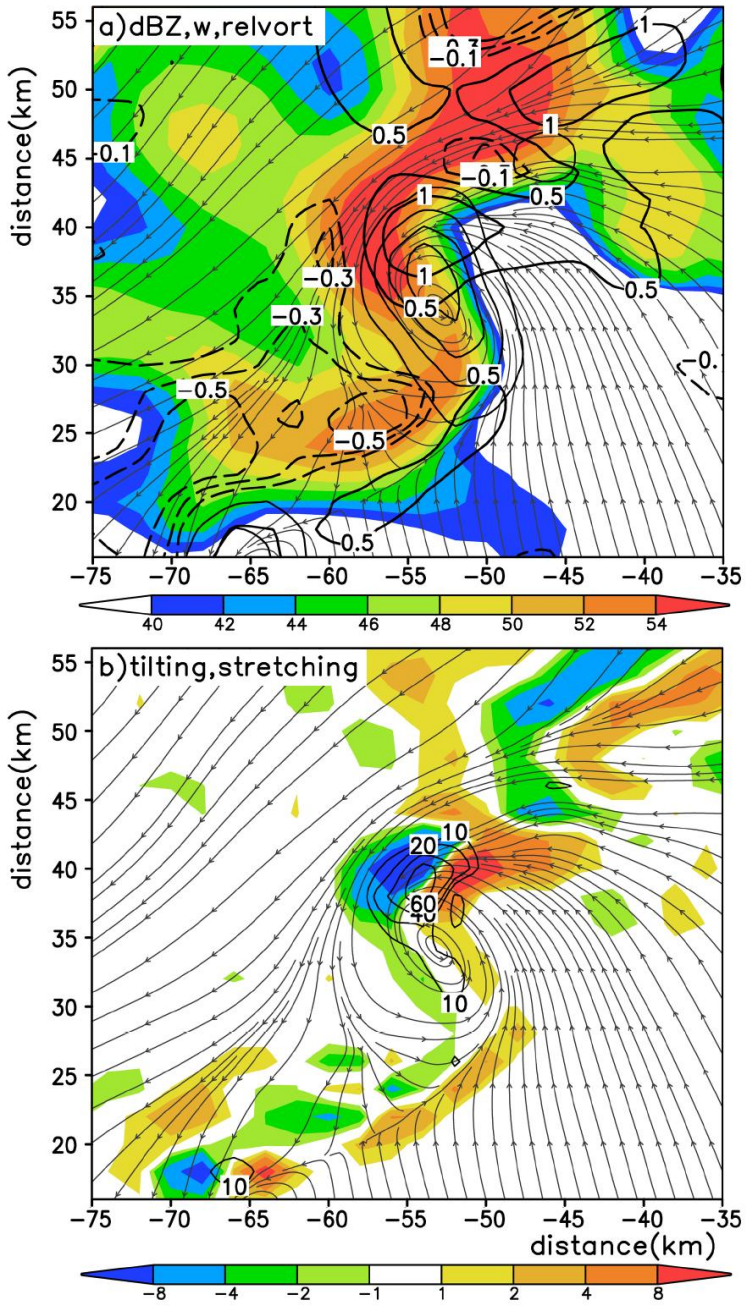


Figure 4.9. Horizontal distribution of near-surface (a) radar reflectivity (shaded, dBZ), vertical motion (heavy contours, $ms^{-1}$), and relative vorticity (light contours at 2, 4, 6, 8, and 10 x $10^{-3}$ $s^{-1}$); (b) tilting rates (shaded, x$10^{-6}$ $s^{-2}$) and stretching rates (contours, x$10^{-6}$). Streamlines at 950 hPa are superposed.

In summary, streamwise vorticity is swept into updrafts along the convergence zone, initially tilted then rapidly stretched, leading to enhanced near-surface vorticity along the convergence zone. This process occurs in many

convective cells along the convergence zone of the spiral band, and only tilting of streamwise vorticity can explain the initial development of near-surface cyclonic vorticity *available for stretching*.

*4.4.5. Vortex mergers*

The supercell described above becomes part of the initial TC-scale vortex, but its scale is of course too small to initiate WISHE. Instead, the merger of several near-surface vortices, spawned in a similar manner, merge to form the primary circulation center. This process is shown explicitly in Fig. 4.10, where vortex 1 (Fig. 4.10a, "1") consumes two additional vortices (Fig. 4.10a, "2" and "3"). Vortices 2 and 3 develop along the convergence zone where streamwise vorticity is preferentially tilted (Fig. 4.8a) and intense convection is supported by midlevel divergence (Fig. 4.4d). Vortex 2 (3) develops about 40 km (70 km) northeast of the center and advects cyclonically inward toward vortex 1. Vortices 2 and 3 are both coupled with discrete updrafts, which constantly ingest streamwise vorticity, first tilting and subsequently stretching to produce the areas of locally-enhanced near-surface cyclonic vorticity. Vortex 3 exhibits in its center an area of minimum pressure, which deepens as it approaches vortex 1.

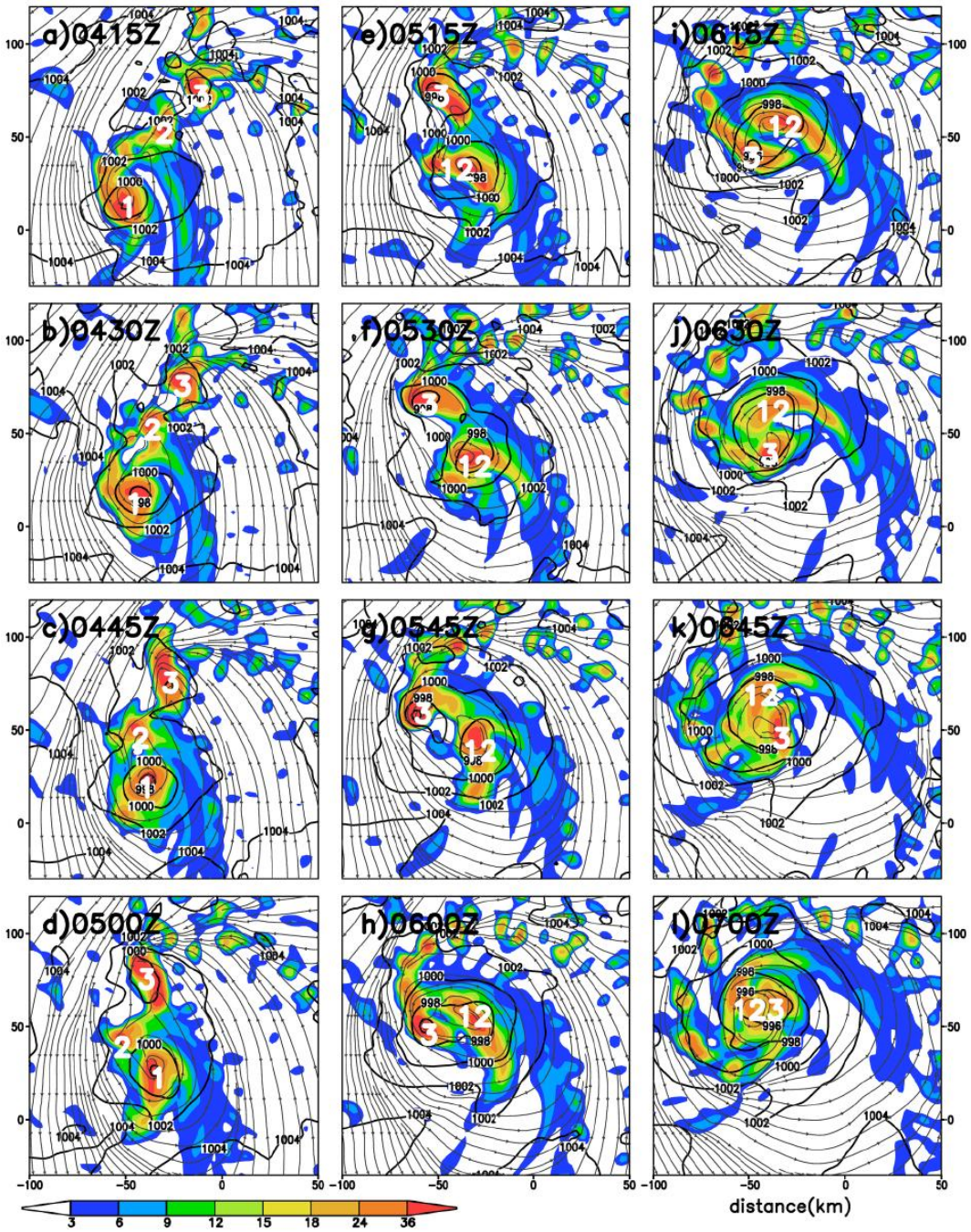


Figure 4.10. Horizontal distribution of 950-hPa relative vorticity (x $10^{-5}$ $s^{-1}$, shaded) at 15-min intervals from (a) 0415 UTC (top-left) – (l) 0700 UTC (bottom-right) 5 May. The surface pressure field (hPa, contours) and the horizontal streamlines are superposed. Symbols "1," "2," and "3" in (a) denote vortices of interest that merge into "123" by (l).

Vortex 2 merges with vortex 1 by 5/5.25-197.25 UTC (Fig. 4.10e), and by 5/06-198 (Fig. 4.10h) vortices 12 and 3 are within close proximity. The vortices

merge into a single, coherent vortex 123 by 5/07-199 (Fig. 4.10l), at which time no dominant vortices are active along the convergence zone. In fact, as the vortex mergers occur near the surface, the convergence zone rotates cyclonically around the center (Fig. 4.10). Vortex 123 exhibits a significantly lower pressure and larger physical size after the mergers (Fig. 4.10l). It is important to note that the mergers shown in Fig. 4.10 are not random mergers; instead they are related to the tendency of convection along the convergence zone to acquire net cyclonic vorticity. In this sense, *vortex mergers near the surface are simply a symptom of TCG and not the cause of TCG*. As will be discussed in the next section, significant changes to the surface vortex occur after 5/06-198, when intensification ceases temporarily (Fig. 4.2).

The processes associated with the low-level vortex amplification during the rapid deepening phase are summarized in Fig. 4.11a-c. As low-level convergence increases along the spiral band, enhanced vertical motion occurs (Fig. 4.11a). Because the low-level inflow is rich in streamwise horizontal vorticity, the updrafts immediately acquire cyclonic vorticity through near-surface tilting (Fig. 4.11b) and subsequently advect along the convergence zone toward the circulation center (Fig. 4.11c).

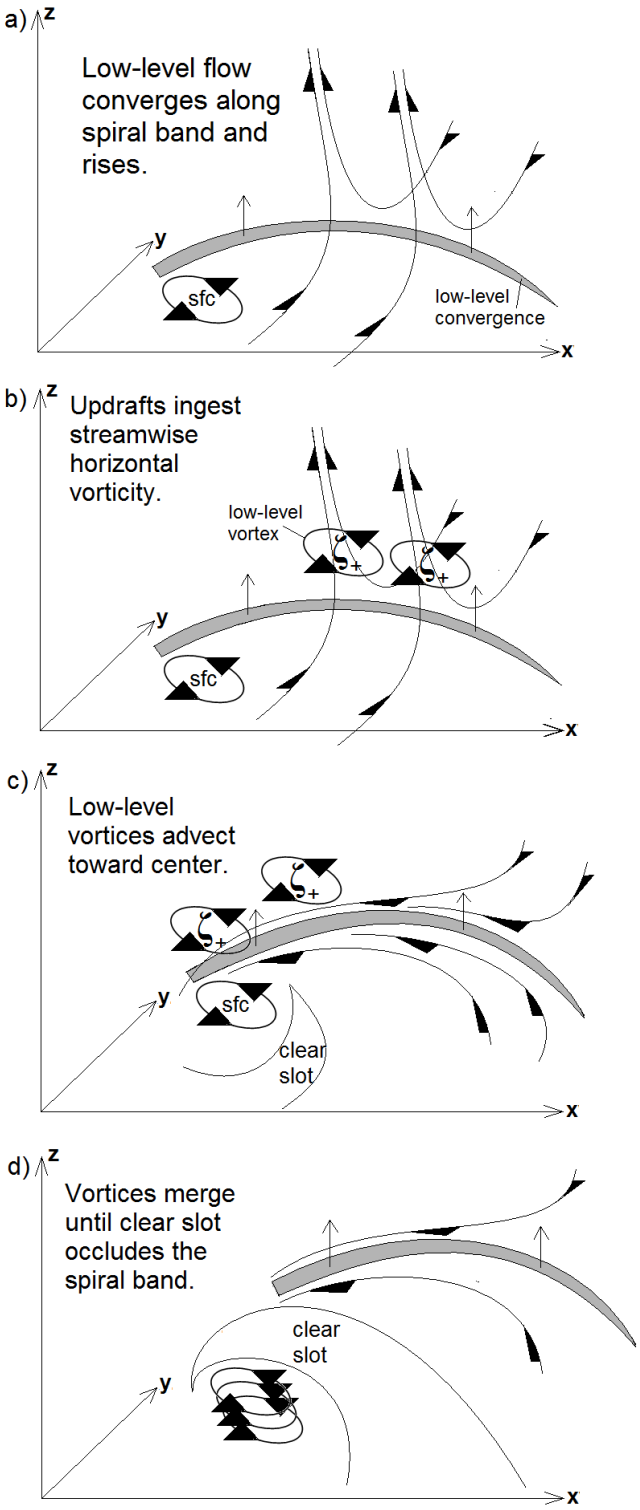


Figure 4.11. Conceptual model of the low-level rapid intensification phase.

*4.5. Intensity maintenance phase*

The processes responsible for the development of near-surface vorticity, and thus the deepening of the central pressure, occur in association with the life cycle of MCS4. At first a disorganized cluster of convection, MCS4 intensifies along a convergence zone and is composed of many cyclonically-rotating convective cells. In this section, we show how the continued evolution of the rainband temporarily causes TCG to stall.

*4.5.1. Thermodynamic characteristics of the clear slot*

As the vortex intensifies by the mergers of low-level vortices, the clear slot wraps cyclonically around the circulation center and covers an increasing spatial area to the east of the circulation center by 5/06-198 (Fig. 4.12a). The low-$\theta_e$ clear slot covers much of the southern semicircle of the low-level circulation (Fig. 4.12b), but only a small portion of the clear slot contains hydrometeors. The critical aspect of the clear slot is that although it comprised entirely of low-$\theta_e$ air near the surface, the thermodynamic characteristics within it differ greatly (c.f. Fig. 4.12b,d). In the vicinity of precipitation, the air is relatively cool and moist due to the evaporative effects of rainfall. However, at the easternmost periphery of the hook echo, an area of descending motion occurs in the clear air (c.f. Fig. 4.12a,c) and is dry and relatively warm (Fig. 4.12d).

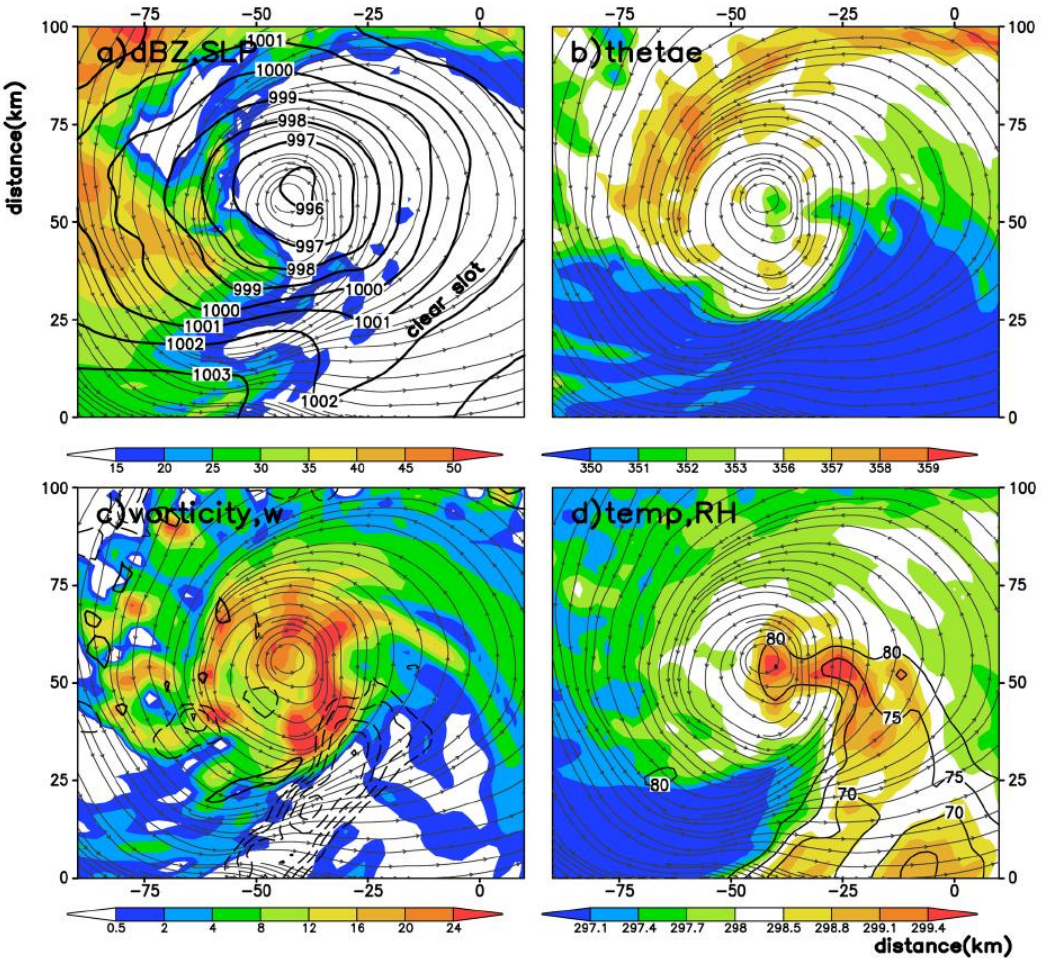


Figure 4.12. Horizontal distribution of (a) radar reflectivity (dBZ, shaded) and sea level pressure (contoured every 1 hPa), (b) $\theta_e$ (shaded), (c) relative vorticity (x $10^{-5}$ $s^{-1}$, shaded) and vertical motion (contoured at -1, -0.8, -0.6, -0.4 -0.2, 1, and 2 m $s^{-1}$); (d) temperature (shaded, K) and relatsive humidity (contoured at intervals of 5% below 80%), at 0600 UTC 5 May during the occlusion.

The dry adiabatic descent likely has its origin in the upstream midtroposphere, where downward motion is dynamically favored on the outside of the spiral band (Fig. 4.6b). Its location to the east of the "hook echo" begs for comparison with the rear flank downdraft (RFD) during tornado formation. Lemon and Doswell (1979) show that tornadogenesis often occurs as the primary updraft of the supercell collapses and downdrafts occur on the upshear side. The downdrafts that wrap cyclonically around the supercell updraft contain some combination of hydrometeors

and forced dry descent, as is evident in this case in Fig. 4.12d. The dry descent during tornado formation allows the tornado to be viewed easily without obstruction from precipitation (see Lemon and Doswell 1979, their Fig. 4). Recent observations indicate that in some cases of strong tornadoes, the RFD is indeed warm (Markowski et al. 2002). When the warm descending air reaches the ground, it spreads in all directions, some inward toward the center. Further, in a study of TCG, Stossmeister and Barnes (1992) observe what appears to be a very similar process in an intensifying TC. They show not only the comma-shaped cloud field with adjacent clear slot (their Fig. 2), but also an area of low-$\theta_e$ air within the clear slot that is warm and dry near the surface. They may have actually observed a similar phenomenon to that described herein, associated with the initial stage of TCG, which in many ways resembles the formation of a larger-scale tornado.

*4.5.2. Occlusion*

Immediately after completion of the mergers by 5/06-198, the low-$\theta_e$ clear slot completely surrounds the circulation center (Fig. 4.13i,j) and effectively cuts off the inflow to the circulation center (Fig. 4.13e,f), which then becomes displaced from the main updrafts within the spiral band (Fig. 4.11c,d). While some convection persists near the circulation center (Fig. 4.13f), the most intense convection along the convergence zone is no longer connected to the circulation center (Fig. 4.8b), which can no longer intensify via mergers, as shown in Fig. 4.10. This process can be considered as an occlusion, similar to that which occurs in a tornado (Alderman et al. 1999; Marquis et al. 2008), and herein marks the end of the first phase of genesis.

After the occlusion, the minimum surface pressure actually slightly increases (Fig. 4.2) during the ensuing 6-h maintenance period, i.e. 5/06-198 – 5/12-204.

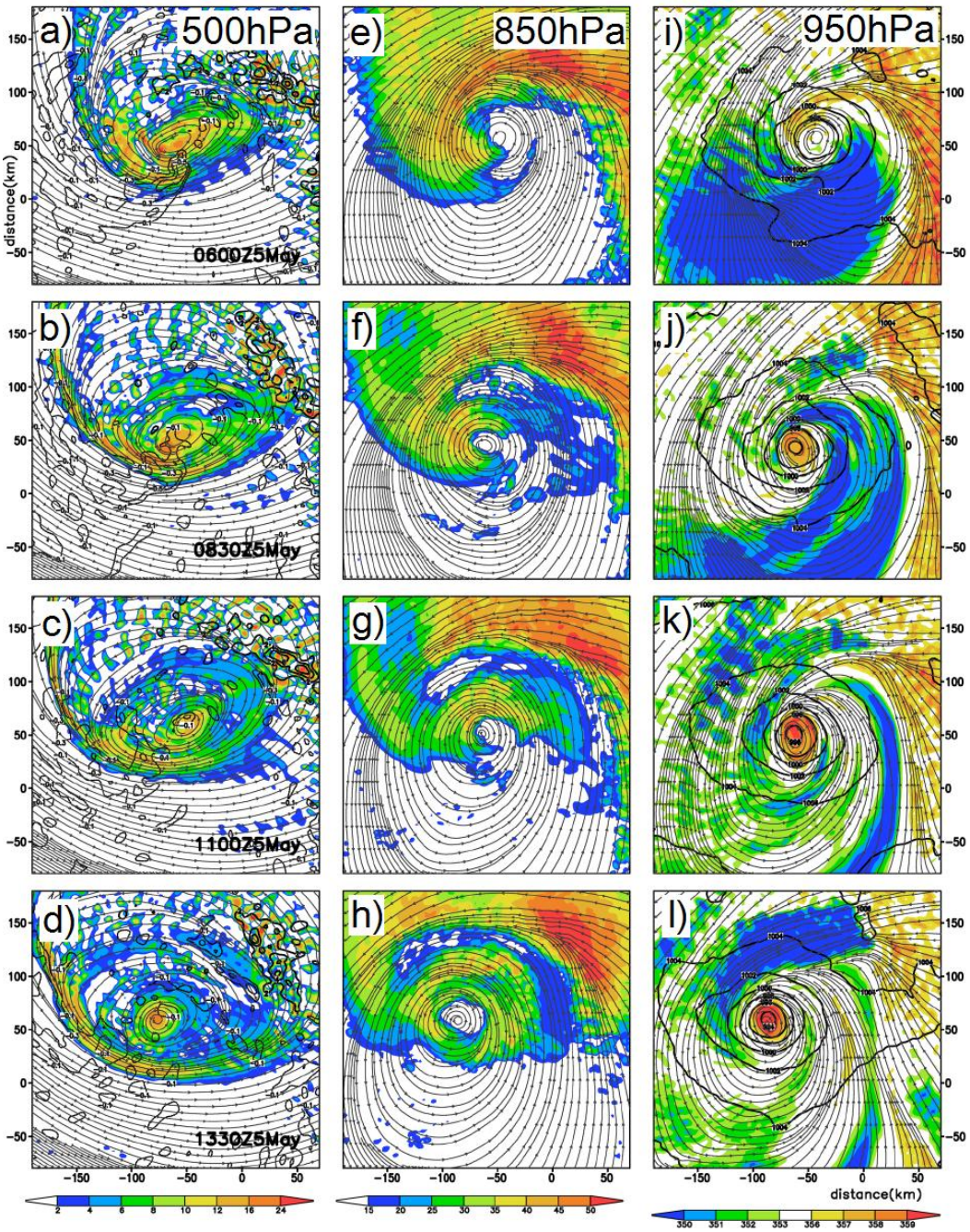


Figure 4.13. As in Fig. 4.4, but for 0600 – 1330 UTC 5 May, i.e. the maintenance phase.

An important feature of the occlusion is that it represents the final transition to an upright vortex at the center (cf. Fig. 4.13a,e). Because the circulation centers

are vertically coherent during this maintenance period, the vertical shear in the core region is very small (not shown), while the shear in the outer regions, e.g. in the vicinity of the detached spiral band, remains large. Thus the large magnitude of the 900 – 400 hPa vertical shear (Fig. 4.1) during this period is associated with peripheral differences in the circulations at 900 and 400 hPa. In this way, the conventional use of area-averaged vertical shear appears to be less applicable to the determination of likelihood of intensification during this portion of Chanchu's life cycle. Although pressure deepening ceases during this period, the detached spiral band (Fig. 4.8b) continues to ingest streamwise vorticity and likely contributes to continued storm-scale intensification (i.e., area-averaged vorticity, Fig. 4.2), but not central pressure deepening.

If the pre-Chanchu disturbance existed over land, it surely would be nearing the end of its life due to the impact of the occlusion. And, as discussed above, post-occlusion Chanchu does temporarily cease intensification. Unfortunately for those affected by Typhoon Chanchu, when the primary band of convection detaches from the circulation center, intensification only temporarily stalls. Because the near-core wind speed increases by nearly 50% (Chapter 2, Fig. 2.8) during the initial 6-h deepening period, the air-sea interaction can quickly modify the low-level low-$\theta_e$ air, which warms through fluxes of both sensible and latent heat. This is particularly true for the warm, dry air (RH < 80%) that descends into the center of the storm during the occlusion. Thus the 950-hPa $\theta_e$ increases between 5/0830-200.5 – 5/11-203 (Fig. 4.13i-l). During this 'recovery period' between 5/06-198 – 5/11-203, the $\theta_e$ increases

significantly in the nascent eye (Fig. 4.13j-l), and the storm-scale RH increases again (Fig. 4.2) after the decrease associated with the drying downdrafts.

The occluded circulation thus does not dissipate, and after the 6-h period of post-occlusion intensity maintenance (Fig. 4.2), Chanchu's intensification simply continues (not shown) in the manner more typically understood for TCs: a warm-core, vertically upright vertical structure, and a quasi-axisymmetric eyewall. The nascent eyewall can be seen in Fig. 4.13f-h.

*4.6 Discussion and conclusions*

In the case of Chanchu, TCG apparently occurs due to the interaction of convection with vertical shear, the latter of which is often ignored for TC studies. Thus it is worthwhile to note some similarities with the evolution of supercells and midlatitude cyclones, both of which are rotating storms that can develop an intense near-surface circulation in sheared environments. The horizontal scale of Chanchu is of course somewhere between the midlatitude cyclone and supercell thunderstorm, but the midlevel-surface interaction that comprises TCG appears qualitatively similar to the canonical depiction of explosive midlatitude cyclogenesis and supercell tornadogenesis. The three highly-sheared storm systems all exhibit rapid surface cyclogenesis, midlevel intensification prior to that at the surface, intensifying near-surface convergence zones, a clear slot during the rapid surface intensification, and an occlusion. And all three take on the comma shape.

In the midlatitudes, a large-amplitude 500-hPa vorticity maximum typically exists for several days prior to surface cyclogenesis (Sanders 1986), and similarly in cases of supercell tornadogenesis the midlevel mesocyclone precedes that in the low

levels and develops due to tilting of environmental vorticity associated with environmental vertical shear. As discussed above, a similar tilting mechanism occurs leading to the intensification of the midlevel vortex in this case.

Another feature common to midlatitude cyclones and supercells is the clear slot, which is associated with rapid near-surface cyclogenesis (Browning 1997) in the midlatitudes and remains a research focus in understanding tornadogenesis. The dry slot in supercell storms acts to focus inflow into a primary updraft which can subsequently tilt and stretch ambient streamwise vorticity to extreme levels. In fact, in this case the minimum surface pressure drops most rapidly as a clear slot forms (Fig. 4.4h), and the location of the minimum pressure occurs at the southeastern tip of the reflectivity signature (Fig. 4.7d), often the location of tornado formation in supercells.

The midlatitude cyclones and tornadoes both occlude as the dry slot encircles and isolates the circulation center from the convection to its northeast and suffocates its supply of moisture. The occlusion typically signals the end of intensification, which stalls without sufficient input of moisture. A similar occlusion occurs in the present case, but aside from the obvious difference in scale, a critical distinction in the analogy of TCG to the other storms is that the *occlusion in the present case does not mark the end of the incipient TC, but rather isolates the circulation such that it can intensify via WISHE*.

This chapter represents a significant departure from the ongoing discourse regarding TCG. Rather than a stochastic process, the TCG process in the case of Chanchu proceeds in an well-organized manner beginning with favorable large scale

conditions. As an MCS intensifies in a sufficiently humid environment in which winds veer with height (Fig. 4.2), midlevel cyclonic vorticity enhancement is strongly favored (Fig. 4.5). The resulting midlevel circulation deforms the MCS into a spiral rainband, along which low-level cyclonic vorticity is preferentially generated from the tilting and subsequent stretching of streamwise vorticity and advected toward the circulation center (Fig. 4.8, 4.9). Through mergers, the surface circulation increases markedly (Fig. 4.10) before the rainband occludes and intensification ceases temporarily.

In this way, we hypothesize that the processes associated with the initial deepening phase (Fig. 4.2, 5/00-192 – 5/06-198), specifically the processes associated with the evolution of MCS4, may represent a *unique mesoscale phenomenon, something like a tropical megacell (TMC).* The life cycle of the TMC in the present case spans a 14-h period from initiation to occlusion (4/16-184 – 5/06-198) and is characterized by a spiraling radar reflectivity structure composed of many discrete updrafts which each acquire cyclonic vorticity from the veering environmental wind. The timescale is significantly shorter (longer) than its midlatitude (supercell) counterpart. Prerequisite to the development of such a TMC in the present case are: a veering wind profile up to 400 hPa, low- and midlevel moistening (Chapter 3), some sort of triggering mechanism (in this case a cold pool left by a previous MCS), and all of the typical TCG preconditions. Barotropic intensification follows after the occlusion phase of the TMC. The 14-hr TMC itself appears responsible for the production of near-surface vorticity, which has until now remained a mysterious process for TCG. Whether such a TMC mechanism occurs in reality and serves as

the trigger for actual TCG must be tested. The present dissertation is merely a single case study.

In summary, we have investigated the processes associated with the TCG of Typhoon Chanchu, as simulated with the WRF at finest resolution of 2 km. Apparently, TCG occurs in three phases. The first phase of initial deepening lasts just 6 h and occurs in a highly vertically sheared (900 – 500 hPa) environment, in which the tilted vortex transitions to vertically upright, facilitated by a spiral convective band. The second phase is one of intensity maintenance that begins as the spiral band occludes and the occluded circulation transitions to a warm core. The second phase of genesis begins with a 6-h period of near-constant intensity. During the maintenance phase, the near-core vertical wind shear diminishes significantly. This period is characterized by the development of a near-surface warm core inside a nascent eye, which is surrounded by low-$\theta_e$ air from the dry slot. After the low-$\theta_e$ air recovers through oceanic heat fluxes, the third phase of intensification occurs as convection intensifies around the warm core and Chanchu continues its intensification in the manner well-understood as a quasi-axisymmetric barotropic cyclone.

# Chapter 5: Summary

*5.1. Concluding remarks*

Several new insights into TCG have been brought to light in this dissertation. The first major result was that the synoptic scale precursor disturbance that eventually spawned Typhoon Chanchu formed on the equator and exhibited initially a dramatic westward vertical tilt and baroclinic vertical structure, which transitioned over a week-long period to a vertically upright structure at the onset of TCG. The tilt arose due to the westward-tilted structure of a westerly wind burst, which was associated with the active phase of the MJO and modulated the formation of the pre-Chanchu vortex. The implication of the vertical tilt was that ascent occurred to the downtilt-right of the vortex axis, where moist easterly flow turned cyclonically northward, and thus favored ascent and precipitation there. The downtilt-left half of the vortex remained precipitation-free, owing to cool outflow air that advected cyclonically from the downtilt-right precipitation. The role of precipitation was its vorticity generation, which served to attract the tilted vortex and align it in the vertical.

The downtilt-right precipitation was shown to take the form of squall lines and convective clusters, which persisted during the several days leading to TCG. Each of the strongest mesoscale convective systems (MCSs) left at the surface a cold pool, which served as the focus for subsequent MCS development. One MCS spawned a midlevel convective vortex (MCV), which merged with and intensified the preexisting tilted vortex. In whole, the series of MCSs preconditioned (i.e., humidified) the near-vortex environment such that the final MCS exhibited no cold pool and was dominated by slantwise updrafts. The final MCS became the first spiral

rainband of the incipient TC and persisted during the initial rapid surface pressure deepening period, which was characterized as a transition from a cold-core vortex to a warm-core vortex.

A second major result arose because the final MCS developed in a highly vertically sheared environment associated with the tilted vortex. The updrafts within the final MCS tilted environmental shear-generated horizontal vorticity, selectively enhancing vorticity on the flanks of the updrafts and ultimately leading to the deformation into a spiral shape. More specifically, because the environmental wind veered with height, it was concluded that net cyclonic vorticity generation was favored on the cyclonic flank of the updrafts. Updrafts that initiated within the MCS thus preferentially acquired cyclonic vorticity at the surface through tilting of horizontal vorticity, and were subsequently stretched in deep vortical updrafts. In short, the initiation of an MCS in an environment with veering winds dictates that each updraft will acquire net cyclonic vorticity at low altitudes, possibly facilitating the often-observed rapid TCG. Until now, the implications of a veering wind profile in the TCG environment has not been mentioned in the literature, likely due to the long-held view that vertical shear-related processes are unfavorable for TCG.

### *5.2. Future research agenda*

Research will continue on several fronts. First, the existence of vertically tilted precursors has not been clearly established in the literature, but the precipitation structure and evolution associated with the vertical alignment of the tilted precursor herein resembles the canonical depiction of TCG, e.g., the development of a spiral band during initial surface pressure deepening. Thus, future research will aim to

understand whether other precursor disturbances do in fact exhibit vertical tilt more often than previously thought, particularly away from dynamic MJO environments.

Moreover, the model exploited herein (the WRF) has demonstrated its ability to successfully reproduce TCG given the existence of a tilted precursor. This suggests that with sufficient representation of the sub-synoptic environment, particularly the vertical structure of the tilted vortex, skillful deterministic predictions of TCG may indeed be possible in these cases. A goal is to work with operationally-acquired datasets to understand whether present observation methodologies are sufficiently sampling the pre-TC environment. If precursors do tilt in the vertical, and the downtilt-right environment does exhibit a veering wind profile, successful numerical TCG forecasts may depend on adequate representation of the vertical structure of the horizontal wind far from the near-surface circulation center, which is often the focus of observational campaigns.

Next, at the convective scale, where convective "hot towers" have long been known to exist in the near-TC environment and play some role in TCs, the supercell structure presented herein has been neither observed nor considered in the deep tropical environment. Of future interest is the detailed structure of this convective cell and the prevalence of its peers in nature. If the typical spiral band in nature is indeed composed of supercellular convection, or at least some tropical variant of the supercell, the mechanisms for TCG could be quite different than that presently understood.

# Bibliography

Aiyyer, A. R., and J. Molinari, 2003: Evolution of mixed Rossby–gravity waves in idealized MJO environments. *J. Atmos. Sci.*, **60,** 2837–2855.

Barnes, S. L., 1970: Some aspects of a severe, right-moving thunderstorm deduced from mesonetwork rawinsonde observations. *J. Atmos. Sci.,* **27,** 634–648.

Barrett, B. S., and L. M. Leslie, 2009: Links between tropical cyclone activity and Madden–Julian oscillation phase in the North Atlantic and Northeast Pacific basins. *Mon. Wea. Rev*., **137**, 727 – 744.

Bartels, D. L., and R. A. Maddox, 1991: Midlevel cyclonic vortices generated by mesoscale convective systems. *Mon. Wea. Rev.,* **119**, 104–118.

Biggerstaff, M. I., and R. A. Houze, Jr., 1991: Kinematic and precipitation structure of the 10 – 11 June 1985 squall line. *Mon. Wea. Rev*., **119**, 3034 – 3065.

Bister, M., and K. A. Emanuel, 1997: The genesis of Hurricane Guillermo: TEXMEX analyses and a modeling study, *Mon. Wea. Rev*., **125**, 2662–2682.

Black, M. L., J. F. Gamache, F. D. Marks, C. E. Samsury, and H. E. Willoughby, 2002: Eastern Pacific Hurricanes Jimena of 1991 and Olivia of 1994: The effect of vertical shear on structure and intensity. *Mon. Wea. Rev.,* **130,** 2291–2312.

Bracken, W. E., and L. F. Bosart, 2000: The role of synoptic-scale flow during tropical cyclogenesis over the North Atlantic Ocean., *Mon. Wea. Rev*., **128,** 353–376.

Braun, S. A., M. T. Montgomery, K. J. Mallen, and P. D. Reasor, 2010: Simulation and interpretation of the genesis of Tropical Storm Gert (2005) as part of the

NASA Tropical Cloud Systems and Processes Experiment, *J. Atmos. Sci*., (pre-release).

Browning, K. A., 1964: Airflow and precipitation trajectories within severe local storms which travel to the right of the winds. *J. Atmos. Sci.,* **21,** 634–639.

Camargo, S. J., M.C. Wheeler, and A.H. Sobel, 2009. Diagnosis of the MJO modulation of tropical cyclogenesis using an empirical index, *J. Atmos. Sci.,* **66**, 3061-3074.

Chang, H.-R., and P. J. Webster, 1990: Energy accumulation and emanation at low latitudes. Part II: Nonlinear response to strong episodic equatorial forcing. *J. Atmos. Sci.,* **47,** 2624–2644.

Davies-Jones, R.P.,1984. Streamwise vorticity: the origin of updraft rotation in supercell storms. *J. Atmos. Sci*. **41**, 2991–3006.

Davis, C. A., and L. F. Bosart, 2001: Numerical simulations of the genesis of Hurricane Diana (1984). Part I: Control simulation. *Mon. Wea. Rev.,* **129**, 1859-1881.

——, and ——, 2003: Baroclinically induced tropical cyclogenesis. *Mon. Wea. Rev.*, **131,** 2730–2747.

——, and ——, 2004: The TT problem: Forecasting the tropical transition of cyclones. *Bull Amer. Meteor. Soc*., **85,** 1657–1662.

Dickinson, M., and J. Molinari, 2002: Mixed Rossby–gravity waves and western Pacific tropical cyclogenesis. Part I: Synoptic evolution. *J. Atmos. Sci.,* **59,** 2183–2196.

Emanuel, K. A., 1986: An air–sea interaction theory for tropical cyclones. Part I: Steady-state maintenance. *J. Atmos. Sci.*, **43,** 585–604.

Emanuel, K. A., 1987: An air–sea interaction model of intraseasonal oscillations in the tropics. *J. Atmos. Sci.*, **44**, 2324–2340.

Frank, W. M., and P. E. Roundy, 2006: The role of tropical waves in tropical cyclogenesis. *Mon. Wea. Rev.,* **134,** 2397–2417.

——, and E. A. Ritchie, 1999: Effects of environmental flow upon tropical cyclone structure. *Mon. Wea. Rev.*, **127**, 2044–2061.

Fritsch, J. M., J. D. Murphy, and J. S. Kain, 1994: Warm core vortex amplification over land. *J. Atmos. Sci.,* **51,** 1780–1807.

Gamache, J. F., and R. A. Houze Jr. (1982), Mesoscale air motions associated with a tropical squall line, *Mon. Wea. Rev*., **110**, 118–135.

Gray, W. M., 1998: The formation of tropical cyclones. *Meteor. Atmos. Phys.,* **67,** 37–69.

Hack, J.J., and W.H. Schubert, 1986: Nonlinear response of atmospheric vortices to heating by organized cumulus convection. *J. Atmos. Sci.*, **43**, 1559-1573.

Harr, P. A., and R. L. Elsberry, 1996: Structure of a mesoscale convective system embedded in Typhoon Robyn during TCM-93. *Mon. Wea. Rev.,* **124,** 634–652.

——, M. S. Kalafsky, and R. L. Elsberry, 1996: Environmental conditions prior to formation of a midget tropical cyclone during TCM-93. *Mon. Wea. Rev.*, **124,** 1693–1710.

Hendricks, E. A., M. T. Montgomery, and C. A. Davis, 2004: The role of ‘‘vortical’’ hot towers in the formation of Tropical Cyclone Diana (1984). *J. Atmos. Sci*., **61**, 1209–1232.

Holland, G. J., 1995: Scale interaction in the western Pacific monsoon. *Meteor. Atmos. Phys.*, **56,** 57–79.

Hong, S.-Y., Y. Noh, and J. Dudhia, 2006: A new vertical diffusion package with an explicit treatment of entrainment processes. *Mon. Wea. Rev.*, **134**, 2318-2341.

Houze, R. A., Jr., S. A. Rutledge, M. I. Biggerstaff, and B. F. Smull, 1989: Interpretation of Doppler weather-radar displays of midlatitude mesoscale convective systems. *Bull. Amer. Meteor. Soc.,* **70**, 608 – 619.

——, 2004: Mesoscale convective systems, *Rev. Geophys.*, **42**, RG4003, doi:10.1029/2004RG000150.

——, W.-C. Lee, and M. M. Bell, 2009: Convective contribution to the genesis of Hurricane Ophelia (2005). *Mon. Wea. Rev*., **137**, 2778 – 2800.

Hoxit, L.R., C.F. Chappell, and J.M. Fritsch, 1976: Formation of mesolows or pressure troughs in advance of cumulonimbus clouds. *Mon. Wea. Rev.*, **104**, 1419-1428.

Hulme, A. L., and J. E. Martin, 2009: Synoptic- and frontal-scale influences on tropical transition events in the Atlantic basin. Part I: A six-case survey. *Mon. Wea. Rev*., **137**, 3605 – 3625.

Jones, S. C., 1995: The evolution of vortices in vertical shear. I: Initially barotropic vortices. *Quart. J. Roy. Meteor. Soc.,* **121,** 821–851.

Kain, J. S., and J. M. Fritsch, 1993: Convective parameterization for mesoscale models: The Kain–Fritsch scheme. *The Representation of Cumulus Convection in Numerical Models, Meteor. Monogr.*, No. 46, Amer. Meteor. Soc., 165–170.

Kieu, C. Q., and D. L. Zhang, 2008: Genesis of Tropical Storm Eugene (2005) Associated with the ITCZ Breakdowns. Part I: Observational and Modeling Analyses. *J. Atmos. Sci.*, **65**, 3419-3433.

——, and ——, 2009: Genesis of Tropical Storm Eugene (2005) from merging vortices ssociated with the ITCZ Breakdowns. Part II: Roles of vortex merger and ambient potential vorticity. *J. Atmos. Sci.*, **66**, 1980-1966.

Kim, J.-H., C.-H. Ho, H.-S. Kim, C.-H. Sui, S. K. Park, 2008: Systematic variation of summertime tropical cyclone activity in the Western North Pacific in relation to the Madden-Julian oscillation. *J. Climate*, **21**, 1171 – 1191.

Klemp, J. B., and R. Rotunno, 1983: A study of the tornadic region within a supercell thunderstorm. *J. Atmos. Sci.*, **40,** 359–377.

Klemp, J. B., and R. B. Wilhelmson, 1978: The simulation of threedimensional convective storm dynamics. *J. Atmos. Sci.*, **35,** 1070–1096.

Lander, M. A., 1990: Evolution of the cloud pattern during the formation of tropical cyclone twins symmetrical with respect to the equator. *Mon. Wea. Rev.*, **118**, 1194–1202.

Lemon, L. R., and C. A. Doswell, 1979: Severe thunderstorm evolution and mesocyclone structure as related to tornadogenesis. *Mon. Wea. Rev.*, **107,** 1184–1197.

Liebmann, B., H. H. Hendon, and J. D. Glick, 1994: The relationship between tropical cyclones of the western Pacific and Indian Oceans and the Madden–Julian oscillation. *J. Meteor. Soc. Japan,* **72,** 401–411.

Lin, Y.-L., R. D. Farley, and H. D. Orville, 1983: Bulk parameterization of the snow field in a cloud model. *J. Appl. Meteor.,* **22,** 1065–1092.

Madden, R. A., and P. R. Julian, 1994: Observations of the 40–50 day tropical oscillation — A review. *Mon. Wea. Rev.,* **122,** 814–837.

Maddox, R. A., 1976: An evaluation of tornado proximity wind and stability data. *Mon. Wea. Rev.,* **104B,** 133 – 142.

Maloney, E. D., and D. L. Hartmann, 2001: The Madden–Julian oscillation, Barotropic dynamics, and North Pacific tropical cyclone formation. Part I: Observations. *J. Atmos. Sci.,* **58,** 2545–2558.

Mao, J., and G. Wu (2008), Influences of Typhoon Chanchu on the 2006 South China Sea summer monsoon onset, *Geophys. Res. Lett.*, **35**, L12809, doi:10.1029/2008GL033810.

Markowski, P.M., Straka, J.M., Rasmussen, E.N., 2002. Direct surface thermodynamic observations within the rear-flank downdrafts of nontornadic and tornadic supercells. *Mon. Wea. Rev.* **130**, 1692–1721.

Markowski, P.M., Straka, J.M., Rasmussen, E.N., 2003. Tornadogenesis resulting from the transport of circulation by a downdraft. *J. Atmos. Sci.* **60**, 795–823.

Markowski, P. M., and Y. P. Richardson, 2009: Tornadogenesis: Our current understanding, forecasting considerations, and questions to guide future research. *Atmospheric Research*, **93**, 3–10.

Marquis, J., Y. Richardson, J. Wurman, P. M. Markowski, 2008: Single- and dual-Doppler analysis of a tornadic vortex and surrounding storm-scale flow in the Crowell, Texas, supercell of 30 April 2000. *Mon. Wea. Rev*., **136**, 5017-5043.

Menard, R. D., and J. M. Fritsch, 1989: A mesoscale convective complex-generated inertially stable warm core vortex, *Mon.Wea. Rev*., **117**, 1237–1261.

Mlawer, E. J., S. J. Taubman, P. D. Brown, M. J. Iacono, and S. A. Clough, 1997: Radiative transfer for inhomogeneous atmospheres: RRTM, a validated correlated-*k* model for the longwave. *J. Geophys. Res.*, **102,** 16 663–16 682.

Molinari, J., K. Lombardo, and D. Vollaro, 2007: Tropical cyclogenesis within an equatorial Rossby wave packet. *J. Atmos. Sci.*, **64**, 1301 – 1317.

Montgomery, M. T., M. E. Nicholls, T. A. Cram, and A. B. Saunders, 2006: A vortical hot tower route to tropical cyclogenesis. *J. Atmos. Sci.*, **63**, 355–386.

Nolan, D. S., 2007: What is the trigger for tropical cyclogenesis? *Aust. Met. Mag*., **56**, 241 – 266.

Rasmussen, E. N., J. M. Straka, R. Davies-Jones, C. A. Doswell III, F. H. Carr, M. D. Eilts, and D. R. MacGorman, 1994: Verification of the Origins of Rotation in Tornadoes Experiment: VORTEX. *Bull. Amer. Meteor. Soc.*,**75,** 995–1006.

Ritchie, E. A., and G. J. Holland, 1997: Scale interactions during the formation of Typhoon Irving. *Mon. Wea. Rev.*, **125,** 1377–1396.

——, and ——, 1999: Large-scale patterns associated with tropical cyclogenesis in the Western Pacific. *Mon. Wea. Rev.*, **127**, 2027–2043.

Rotunno, R., 1981: On the evolution of thunderstorm rotation. *Mon. Wea. Rev.*, **109,** 577–586.

——, and J. B. Klemp, 1982: The influence of the shear-induced pressure gradient on thunderstorm motion. *Mon. Wea. Rev.,* **110,** 136–151

——, and ——, 1985: On the rotation and propagation of simulated supercell thunderstorms. *J. Atmos. Sci.,* **32,** 271 – 292.

Sanders, F., 1986: Explosive cyclogenesis in the west-central North Atlantic Ocean, 1981-84. Part I: Composite structure and mean behavior, *Mon. Wea. Rev*., **114**, 1781-1794.

Simpson, J., E. Ritchie, G. J. Holland, J. Halverson, and S. Stewart, 1997: Mesoscale interactions in tropical cyclone genesis. *Mon. Wea. Rev.,* **125,** 2643–2661.

Sobel, A. H., and E. D. Maloney, 2000: Effect of ENSO and the MJO on western North Pacific tropical cyclones. *Geophys. Res. Lett.,* **27,** 1739–1742.

Skamarock, W. C., J. B. Klemp, J. Dudhia, D. O. Gill, D. M. Barker, W. Wang, and J. G. Powers, 2005: A description of the Advanced Research WRF, version 2. NCAR Tech. Note NCAR/TN-468_STR, 88 pp.

Sperber, K. R., 2003: Propagation and the vertical structure of the Madden-Julian oscillation. *Mon. Wea. Rev.*, **131**, 3018 – 3037.

Stossmeister, G. J., and G.M. *Barnes*, 1992: The Development of a Second Circulation Center within Tropical Storm Isabel (1985). *Mon. Wea. Rev*., **120**, 685–697.

Tao, W.-K., J. Simpson, C.-H. Sui, B. Ferrier, S. Lang, J. Scala, M.-D. Chou, and K. Pickering, 1993: Heating, moisture, and water budgets of tropical and midlatitude squall lines: Comparisons and sensitivity to longwave radiation. *J. Atmos. Sci.*, **50**, 673-690.

Wang, Y., and G. J. Holland, 1996: The beta drift of baroclinic vortices, Part II: Diabatic vortices. *J. Atmos. Sci.,* **53,** 3737–3756.

Weisman, M. L., and J. B. Klemp, 1986: Characteristics of isolated convective storms. *Mesoscale Meteorology and Forecasting*, P. S. Ray, Ed., Amer. Meteor. Soc., 331–358.

——, and C. A. Davis, 1998: Mechanisms for the generation of mesoscale vortices within quasi-linear convective systems. *J. Atmos. Sci*, **55**, 2603–2622.

Willoughby, H. E., F. D. Marks, Jr., and R. J. Feinberg, 1984: Stationary and moving convective bands in hurricanes. *J. Atmos. Sci.*, **22**, 3189-3211.

Yuter, S. E., and R. A. Houze Jr., 1998: The natural variability of precipitating clouds over the western Pacific warm pool. *Quart. J. Roy. Meteor. Soc.*, **124**, 53–99.

Zhang, D.-L., and J. M. Fritsch, 1987: Numerical simulation of the meso-b scale structure and evolution of the 1977 Johnstown flood. Part II: Inertially stable warm-core vortex and the mesoscale convective complex. *J. Atmos. Sci.*, **44**, 2593–2612.

——, and ——,1988 Numerical simulation of the meso-beta scale structure and evolution of the 1977 Johnstown flood. Part III: Internal gravity waves and the squall line. *J. Atmos. Sci.,* **45,** 1252–1268.

——, , and K. Gao, 1989: Numerical simulation of an intense squall line during 10–11 June 1985 PRE-STORM. Part II: Rear inflow, surface pressure perturbations, and stratiform precipitation, *Mon. Wea. Rev*., **117**, 2067–2094.

——, 1992: The formation of a cooling-induced mesovortex in the trailing-stratiform region of a midlatitude squall line, *Mon. Wea. Rev*., **120**, 2763–2785.

——, and N. Bao, 1996a: Oceanic cyclogenesis as induced by a mesoscale convective system moving offshore. Part I: A 90-h real-data simulation. *Mon. Wea. Rev.,* **124,** 1449–1469.

——, and ——, 1996b: Oceanic cyclogenesis as induced by a mesoscale convective system moving offshore. Part II: Genesis and thermodynamic transformation. *Mon. Wea. Rev.,* **124,** 2206–2226.

——, Y. Liu and M.K. Yau, 2001: A multiscale numerical study of Hurricane Andrew (1992). Part IV: Unbalanced flows. *Mon. Wea. Rev.*, **129**, 92-107.

——, and C. Q. Kieu, 2006: Potential vorticity diagnosis of a simulated hurricane. Part II: Quasi-balanced contributions to forced secondary circulations. *J. Atmos. Sci.,* **63,** 2898–2914.

Zhu, C.-W., T. Nakazawa and J.-P. Li, 2003: Modulation of twin tropical cyclogenesis by the MJO westerly wind burst during the onset period of 1997/98 ENSO. *Advances in Atmos. Sci.*, **20**, 882-898.

Zipser, E. J., and C. Gautier, 1978: Mesoscale events within a GATE tropical depression. *Mon. Wea. Rev.*, **106**, 789-805.